Liudmila Fokina

Coherent Spin Dynamics of Carriers in GaAs and CdTe Semiconductor Quantum Wells

Coherent Spin Dynamics of Carriers in GaAs and CdTe Semiconductor Quantum Wells

Dissertation

presented to the Institute of Physics of the TU Dortmund University, Germany in partial fulfilment of the requirements for the degree of Doktor rer. nat.

presented by

Fokina Liudmila

Dortmund, March 2010

Accepted by the faculty of the Institute of Physics of the TU Dortmund University, Germany.

Day of the oral examination: 12th March 2010

Examination board:

Prof. Dr. Dmitri Yakovlev

Prof. Dr. Markus Betz

Prof. Dr. Götz S. Uhrig

Dr. Bärbel Siegmann

Contents

Motivation

Currently, manipulating electron charge is the sole characteristic the electronics industry utilizes in computers and other digital devices. But in order to create faster and more powerful devices, researchers have been exploring the possibility instead of using electron spin to carry, process and store information. Electron spins offer major advantages over electron charge degrees of freedom, potentially both for devices for conventional computation as well as for quantum computation. The spin is much less susceptible to external noise and at the same time, the magnetic noise levels are generally lower than the electrical ones. The spin can be easily manipulated by externally applied magnetic fields, this property already in use in magnetic storage technology. Another more subtle, but potentially significant property of spin is its long coherence, or relaxation, time-once created it tends to stay that way for a long time, unlike charge states, which are easily destroyed by scattering or collision with defects, impurities or other charges [1]. Another avenue for using the spins of elementary particles comes from the rapidly developing field of quantum computing. The states of spin of electrons can be used as an implementation of a qubit (quantum bit, the unit of quantum information). Information can be encoded using the polarization of the spin, manipulation (computation) can be done using external magnetic fields or laser pulses, and readout can be done by measuring spin-dependent transport. Quantum computers execute a series of simple unitary operations (gates) on one or two qubits at a time. The computation on a quantum computer is a sequence of unitary transformations of an initial state of a set of qubits. After the computation is performed, the qubits can be measured, and the outcome of the measurement is the result of the quantum computation.

Not only that the fields of quantum computing [2, 3] and quantum communication [3, 4] could revolutionize computing, but also the performance of quantum electronic devices in conventional computers can be enhanced by the electron spin, e.g. spin-transistors (based on spin-currents and spin injection), non-volatile memories, single spin as the ultimate limit of information storage etc [5].

By understanding the behavior of the electron spin in semiconductor materials one can learn something new about solid state physic and of course it helps to develop new generation of the electronic devices that could be much smaller, consume less energy and be more powerful then today's devices.

Outline

The outline of this work is as follows: The Chapter 1 gives a brief introduction into the basic theory required for the analysis of the data throughout this thesis. It is starting from introduction of the band structure of GaAs and CdTe semiconductors including explanation of optical selection rules and describes the evolution from bulk materials to low dimensional systems. Here we focus on two-dimensional structures-quantum wells and give some introduction to the physics of particles in a quantum well from quantum mechanical point of view. As next we define such important concepts like spin dephasing and spin coherence. The chapter ends with fundamentals of spin coherence and a compilation of spin relaxation mechanisms relevant for our experiments.

In the Chapter 2 we discuss the pump-probe technique based upon dynamic measurements of the Faraday and Kerr effects to reveal information about coherent spin evolution that occurs on time scales much longer than the radiative recombination times. The setup as well as the measurement procedure on ultrashort time scale will be described here. Here you can find as well a brief description of the samples.

Systematic investigation of the spin dephasing times in GaAs/(Al,Ga)As quantum wells and its depending on parameters like temperature, magnetic fields and doping will be shown in Chapter 3.

In Chapter 4 are presented results of investigation of the nuclear spin systems in quantum well heterostructures. The chapter 5 presents the results of studying the carrier spin dynamics in a n-doped (In,Ga)As/GaAs quantum wells by time-resolved Faraday rotation and ellipticity techniques in the temperature range down to 430 milliKelvin.

In Chapter 6 is devoted to experimental and theoretically studying of optical control of the spin coherence of quantum well electrons by short laser pulses with circular or linear polarization. For that purpose the coherent electron spin dynamics in a n-doped CdTe/(Cd,Mg)Te quantum well structure was measured by time-resolved pump-probe Kerr rotation, using resonant excitation of the negatively charged exciton (trion) state.

Chapter 1

Introduction

In this thesis GaAs/(Al,Ga)As and CdTe/(Cd,Mn)Te QW heterostructures are investigated. To facilitate the presentation and understanding of the results, discussed in the following chapters, it is necessary to give an overview about the structural, electronic and magnetic properties of these materials in the first sections of this chapter. Electronic band structures of the studied materials are described in the following sections, as well as a effects of the quantum confinement in the semiconductors heterostructures.

1.1 Semiconductors and semiconductor nanostructures

GaAs and CdTe have a zinc-blende crystal structure, which is based on a face-centered-cubic (f.c.c.) lattice and belong to the T_d point symmetry group. In such structures, each constituent atom has four valence electrons, given that eight electrons are covalently shared in each molecule comprising the crystal. The valence electrons of a four-valent atom come from s- and p-orbitals, and the nature of these orbital plays into the character of the semiconductor band structures, especially at the band edge, where the electron wave vector is null or $\mathbf{k} = 0$ [6]. When the structure has an even number of electrons per atom, as in our case, the highest occupied band is completely full of electrons and is called the valence band (VB) and the lowest unoccupied band is called the conduction band (CB). Somewhere between the VB and CB is the Fermi energy located. Excitation of an electron, and hence absorption of a photon, requires a minimal amount of energy corresponding to the energy difference between the VB and CB, which as referred to as the band gap, E_g. When a photon is absorbed by the semiconductor, and electron from the VB is promoted to the CB, leaving behind a hole in the VB. GaAs and CdTe have a direct band gap located at the center of the Brillion zone. This property make them favorably suited for optical studies. The GaAs energy band structure is displayed in the Fig. 1.1. The conduction band CB is s-like and degenerated in a two fold way considering the electron spin. Due to spin orbit interaction, the p-type valence band (VB) six-fold degeneracy is lifted. One band with $j = 1/2$ (sh holes) is energetically split off by Δ_{SO}. The two $j = 3/2$ bands exhibit two

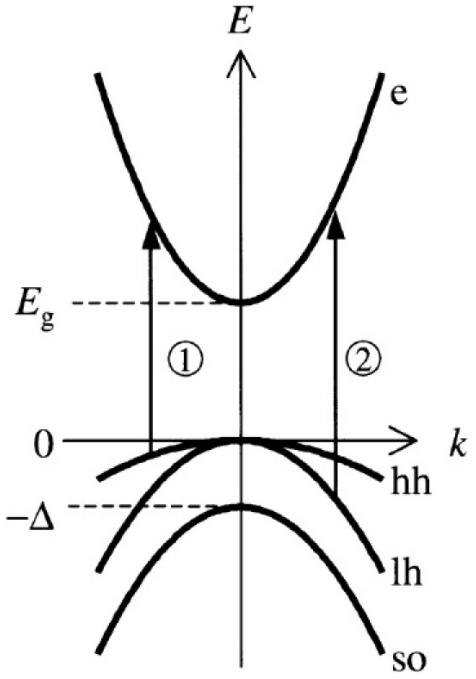

Figure 1.1: Band structure of a direct gap III-V semiconductor such as GaAs near **k** = 0. $E = 0$ corresponds to the top of the valence band, while $E = E_g$ corresponds to the bottom of the conduction band. Four bands are shown: the heavy hole (hh) band, the light hole (lh) band, the split-off hole (so) band, and the electron (e) band. Two optical transitions are indicated. Transition 1 is a heavy hole transition, while transition 2 is a light hole transition. Transitions can also take place between the split-off hole band and the conduction band, but these are not shown for the sake of clarity. This four-band model was originally developed for InSb in reference [8].

curvatures and are therefore divided into heavy hole (hh) and light hole (lh) band [6]. All four of these bands have parabolic dispersion curves near $\mathbf{k} = 0$. Positive curvature of a CB indicates an electron band, and negative curvature of a VB indicates a hole band. An electron in the CB behaves like a negatively-charged free particle of mass m_e^*, whereas a hole in the VB behaves like a positively-charged free particle of mass m_h^*. The dispersion for the four bands near $\mathbf{k} = 0$ are written as follows:

$$E_c(k) = E_g + \frac{\hbar^2 k^2}{2m_e^*} \tag{1.1}$$

$$E_{hh}(k) = -\frac{\hbar^2 k^2}{2m_{hh}^*} \tag{1.2}$$

$$E_{lh}(k) = -\frac{\hbar^2 k^2}{2m_{lh}^*} \tag{1.3}$$

$$E_{so}(k) = -\Delta_{so} - \frac{\hbar^2 k^2}{2m_{so}^*} \tag{1.4}$$

The p-like nature of the VBs and s-like nature of the CB makes transitions from all three bands to the CB dipole-allowed by electric dipole selection rules. However, the SO hole band is rarely involved in direct-band studies because its energy is so low. Important property of GaAs and CdTe relevant for this thesis are summarized in the Table 1.1.

Parameters	***GaAs***	***CdTe***
Band gap E_g (eV) at T= 1.6 K	1.6	1.5
Lattice constant, a (nm)	0.57	0.65
Exciton Bohr radius, a_x (nm)	13	6.7
Exciton Rydberg energy, E_x (meV)	4.2	12
Electron effective mass, m_e/m_0	0.066	0.1
Heavy hole effective mass, m_{HH}/m_0	0.47	0.4

Table 1.1: Parameters for GaAs and CdTe.

1.1.1 Optical selection rules

Photon absorption and emission (luminescence) are powerful tools in characterizing the band structure of semiconductors. The hole to electron transition obeys selection rules which preserve the angular momentum of the incoming or outgoing photon. If the photons are right or left circularly polarized they carry an angular momentum of +1 or -1 (denoted by σ^+ and σ^-), respectively. The optical selection rules for absorption or emission of circularly polarized photons near the hand edge between $j = 3/2$ hole states of the valence band and $j = 1/2$ electron states of the conduction band are illustrated in Fig. 1.2. Four different absorption and emission processes are allowed. Two of them involve heavy hole states, the others involve light hole states. It is important to note that an electron in the valence band with spin $J_z = -3/2$ leaves a hole of opposite spin after it is excited into the conduction band. The absorption process can thus be viewed in two equivalent ways: (1) a σ^+ photon transfers its angular momentum to an electron, promoting it from $j_z = -3/2$ to $j_z = -1/2$, or (II) a σ^+ photon creates an electron-hole pair with a total z angular momentum ($j_{z,hh} + j_{z,e} = 3/2 - 1/2 = +1$) equal to that of the photon (+1) [10]. As seen in Fig. 1.2 the absorption of σ^+ photons will inject spin -1/2 electrons for heavy hole transitions and at the same spin +1/2 electrons for light hole transitions. As the absorption probabilities for both transitions differ by a factor of 3, the absorption of σ^+ photons results in a large net electron spin polarisation of -50%, where the sign reflects the relation between photons and spin polarization. The inverse process, which is the recombination of electrons with holes, obeys the identical selection rules. A spin -1/2 electron can recombine with a -3/2 heavy hole state and emit a σ^+ photon. The luminescence emitted by spin polarized electrons recombining with unpolarized holes will thus be circularly polarized. These processes allow the conversion of spin polarization into an optical polarization. In particular the luminescence process can be used as a spin-detector for electrical spin

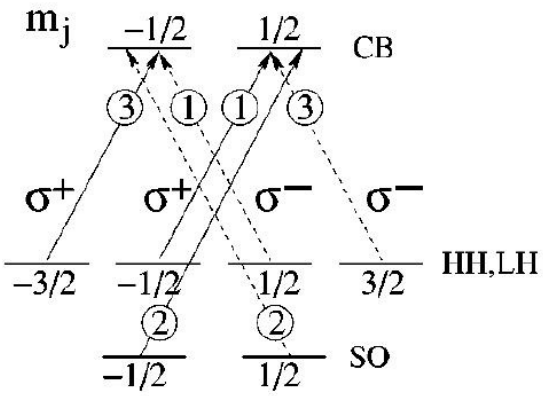

Figure 1.2: Optical selection rules between $j = 3/2$ holes (valence band) and $j = 1/2$ electrons (conduction band). The probability for heavy hole transitions ($j_z = 3/2$) is three times as large as for the light hole transitions (j_z) [10].

injection [63, 64]. The degree of optical polarization yields another -50 %, which leads to a total photoluminescence polarization of $P_{max,PL} = 25\%$ when using pure σ^+ or σ^- photon for excitation. The absorption process circularly polarized light is called optical pumping or optical spin orientation [50].

1.2 Exciton and trion

When an electron lifts from valence to conduction band, it leaves a positively charged hole in the valence band. The Coulomb interaction between electron and hole results in a bound state which is called exciton (X). It can be described in the effective mass approximation. With the exciton Bohr radius a_B^{ex} the exciton binding energy E_b^{ex} is given by

$$E_b^{ex} = E_{Ry}^h \frac{\mu}{m_0} \frac{1}{\varepsilon^2(0)}, \qquad a_B^{ex} = a_B^h \frac{m_0}{\mu}, \qquad \frac{1}{\mu} = \frac{1}{m_e} + \frac{1}{m_h} \ . \tag{1.5}$$

Here μ is the reduced mass, m_h the effective hole mass [65], E_{Ry}^h is the Rydberg energy and a_b^h the exciton Bohr radius of the hydrogen atom. The existence of exciton and trion states may be inferred from the absorption of light associated with their excitation. Typically, excitons are observed just below the band gap. In the presence of an excess of electrons in the conduction band, the neutral exciton might be able to bind a second electron forming a three-particle system, i.e. the negatively-charged exciton, T^- , also called the negatively-charged trion . The existence of T^- was predicted by Lampert [66] in 1958 for the first time by making an analogy with the negatively-charged hydrogen ion, H^- , resulting in an T^- binding energy of 0.055 Ry. This binding energy is the energy needed to remove the second electron, leaving X and an additional electron in the conduction band.

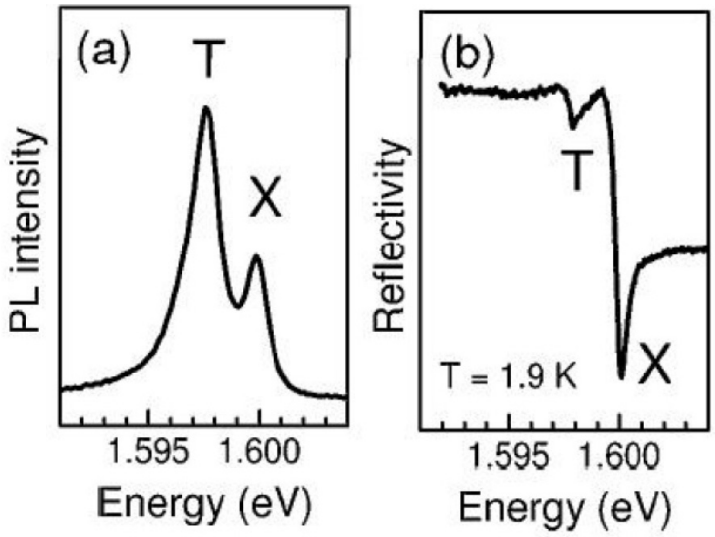

Figure 1.3: (**a**) Photoluminescence spectrum of a 20-nm-thick CdTe/$Cd_{0.78}Mg_{0.22}$Te quantum well measured under nonresonant continuous-wave excitation with a photon energy of 2.33 eV. The exciton (X) and trion (T) resonances are separated by the trion bindning energy of 2 meV. (**b**) Reflectivity spectrum of the same structure [34].

In a similar way to T^- , the positively-charged exciton, T^+ , can be formed when X binds a second valence-band hole originating from an excess of 2DHG carriers. In the quantum wells the trion binding energies are strongly enhanced due to confinement and can reach several meV. The existence of exciton and trion states may be inferred from the absorption of light associated with their excitation.

A photoluminescence (PL) spectrum of the n-type CdTe/$Cd_{0.78}Mg_{0.22}$Te quantum well measured at temperature $T = 1.9$ K is given in Fig. 1.3 (a)[16]. The spectrum shows two peak signature, with the higher energy being the neutral exciton, X, and the lower energy being the negatively charged trion, T^-. The energy separation between the two lines is the binding energy, $E_B = 2$ meV, of the second electron to the trion complex. The exciton binding energy is 12 meV. The full width at half maximum of the exciton line is about 0.5 meV and arises mainly from exciton localization in well width fluctuations. The relative strength of each of these PL lines is related to the background electron density, n_e: the lower the electron density is, the weaker is the exciton intensity and the stronger the trion line becomes. The background electron density affects not only the relative strength of the X and T^- peaks, but also their energy separation and lineshape. One can view the exciton as the ionized state of the trion, and hence their energy separation ΔE is the energy needed to excite an electron from the bound state in a trion to above the Fermi energy, E_F, with the final state being an exciton and a free electron. It is easy to see that this energy is $E_B + E_F$, and therefore, the energy separation between exciton and trion should evolve with density as $\Delta E = E_B + E_F$ [67].

1.3 Quantum well

Semiconductor quantum wells are examples of heterostructure crystals. Heterostructures are artificial crystals that contains layers of different materials grown on top of a thicker substrate crystal. The structures are made by the specialized epitaxial crystal growth techniques, ones is molecular-beam epitaxy (MBE). The layer thicknesses of the crystal grown by these techniques can be controlled with atomic precision. This makes it easy to achieve the thin layer thicknesses required to observe quantum confinement of the electrons in a semiconductor at room temperature [8].

The size dependence of the optical properties in very small crystals is a consequence of a quantum confinement effect [8]. The Heisenberg uncertainty principle tells, that if on confines a particle to a region of the x axis of length Δx, ten it will be introduced an uncertainty in its momentum given by [8]:

$$\Delta p_x \sim \frac{\hbar}{\Delta x}. \tag{1.6}$$

If the particle is otherwise free, and has a mass m, the confinement in the x direction gives it an additional kinetic energy of magnitude

$$E_{conf} = \frac{(\Delta p_x)^2}{2m} \sim \frac{\hbar^2}{2m(\Delta x)^2}. \tag{1.7}$$

Quantum confinement becomes important when the confinement energy, E_{conf}, is comparable or larger than the thermal kinetic energy of the particle due to its thermal motion in the x direction. This condition may be written, then

$$E_{conf} \sim \frac{\hbar^2}{2m(\Delta x)^2} > \frac{1}{2}k_B T. \tag{1.8}$$

It means that quantum size effects will be important if

$$\Delta x \sim \sqrt{\frac{\hbar^2}{mk_B T}}, \tag{1.9}$$

here k_B the Boltzmann constant and T temperature. This equation is equivalent to say that Δx must be of the same order of magnitude as the de Broglie wavelength $\lambda_d eB \equiv p_x/h$ for the thermal motion [8]. The criterion presented in Eq. (1.9) gives an idea of how small the structure must be if one is to observe quantum confinement effects. For an electron in a typical semiconductor with $m_e^* = 0.1m_0$ at room temperature, it must be $\Delta x \sim 5nm$.

The are three general classification of quantum confinement effects. If the motion is confined in one direction (e.g. z-direction), the structure is called a quantum well. The electrons are free to move in other two directions (i.e. x- and y-directions) and so we have free motion in two dimensions and quantized motion in the third. If the motion is confined in two directions the structure is called a quantum wire. Finally, if the motion is confined in all three directions a structure is called quantum dot.

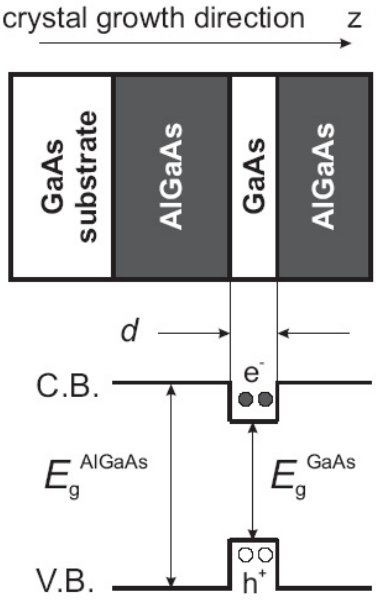

Figure 1.4: Schematic diagram of a single GaAs/(Al,Ga)As quantum well. The quantum well is formed in the thin GaAs layer sandwiched between (AlGa)As layers which have a larger band gap. The lower half of the figure shows the spatial variation of the conduction band (CB) and the valence band (VB).

Here we consider the properties of quantum well. This is effectively a two-dimensional system with quantized motion in z-direction and free motion in other two directions. In the simplest model, a quantum well can be considered as a one-dimensional potential well. From quantum-mechanics texts is known, that the energy of a particle of mass m confined in a deep potential well of width L is given by:

$$E = \frac{\hbar^2}{2m}\left(\frac{n\pi}{L}\right)^2 \tag{1.10}$$

where n is an integer. The energy for quantized motion in the z-direction of a semiconductor quantum well of thickness d will therefore be given approximately by:

$$E = \frac{\hbar^2}{2m_e^*}\left(\frac{n\pi}{d}\right)^2 \tag{1.11}$$

, where m_e^* is the effective mass. In this model the lowest energy state for the electrons in the conduction band is equal to $(E_g + \frac{\hbar^2\pi^2}{2m_e^* d^2})$. This shows that the effective band gap shifts to higher energy as the well width decreases [68]. Quantum wells are formed by growing a layer of a semiconductor of thickness d between layers of another semiconductor with a larger band gap, as illustrated schematically in Fig. 1.4. In this particular case, it is shown a GaAs/(Al,Ga)As structure, grown on a GaAs substrate. The structure consists of a GaAs layer of thickness d sandwiched between much thicker layers of the alloy semiconductor AlGaAs. d is chosen so that the motion of the electrons in the GaAs layer is quantized according to the criterion given in equation . We

set up axes so that the z axis corresponds to the crystal growth direction, while the x and y axes lie in the plane of the layers. We thus have quantized motion if the z direction, and free motion in the x-y plane. The bottom half of Fig. 1.4 shows the spatial variation of the conduction and valence bands that corresponds to the change of the composition along the z direction. The band gap of AlGaAs is larger than that of GaAs, and the bands line up so that the lowest conduction and valence band states of the GaAs lie within the gap of the AlGaAs. This means that electrons in the GaAs layer are trapped by potential barriers at each side due to the discontinuity in the conduction band. Similarly, holes are trapped by the discontinuity in the valence band. These barriers quantize the states in the z direction, but the motion in the x-y plane is still free. We thus effectively have a two-dimensional system in which the electrons and holes are quantized in one direction and free in the other two. Epitaxial techniques are very versatile, and they allow the growth of a great variety of quantum well structures [8].

1.4 Larmor precession and g-factor

In order to study magnetic field dependence of the spin dephasing time, one apply the magnetic field perpendicular (Voigt geometry) to the initial spin direction. As result elecron spins start to precess with the Larmor frequency (ω_L) due to creation of a coherent superposition of the eigenstates for spin-up and spin-down by the applied external magnetic field. The energy eigenvalues for the spin up and spin down states are then (the frequency of the phase oscillation in this superposition)

$$\hbar\omega_L = \Delta E \equiv E_{\Uparrow} - E_{\Downarrow} = \frac{e\hbar B}{m_e} \tag{1.12}$$

here $e = 1.602\times\ 10^{-19}$C the elementary charge, $\hbar$ the reduced Planck constant. The B-field is taken along the z-axis, which also defines the quantization axis.

The Larmor frequency can be written as

$$\omega_L = g_0\mu_B B/\hbar \tag{1.13}$$

using the material dependent parameter Lande g-factor of the free electron $g_0 = 2.002$ and the Bohr magneton $\mu_B = (e\hbar)(g_0 m_e) = 9.274 \times 10^{-24}$ J/T.

The Eq. (1.13) is usually valid for free electrons. In our case, where spins in GaAs and CdTe optically oriented, we have to replace the Lande g-factor by an effective g-factor, the same like for the free electron mass that is replaced by the effective mass $m_e \rightarrow m_e^*$. For conduction band electrons in semiconductors heterostructures it may deviate strongly from the free electron g-factor in vacuum $g_0 = 2.002$ due to the spin-orbit interaction, for example it is g_e= -0.44 in GaAs and g_e= -1.64 in CdTe. In GaAs QWs, the quantum confinement renders the g-factor of 2D electrons anisotropic and modifies the values of the components of the g-factor along ($g_\parallel$) and perpendicular ($g_\perp$) to the growth axis of the heterostructure.

In this thesis are presented experimental results for the time-resolved pump-probe Kerr rotation, which allow us to determine the transverse component $g_\perp$ of the electron g-factor with high accuracy from the frequency of the spin precession in an external magnetic field.

1.5 Spin relaxation

1.5.1 Spin relaxation and spin dephasing

Spin relaxation and spin dephasing are processes that lead to spin equilibration and are thus of great importance for spintronics. The fact that nonequilibrium electronic spin in metals and semiconductors lives relatively long (typically a nanosecond), allowing for spin-encoded information to travel macroscopic distances, is what makes spintronics a viable option for technology. After introducing the concepts of spin relaxation and spin dephasing times T_1 and T_2, respectively, which we discuss four major physical mechanisms responsible for spin equilibration in nonmagnetic electronic systems: Elliott-Yafet, Dyakonov-Perel, Bir-Aronov-Pikus, and hyperfine-interaction processes.

1.5.2 Electron spin coherence

In order to study spin coherence in a semiconductors, an ensemle of electrons spins is excited by an optical pulse from an ultrafast laser. In the initial state, all optically excited spins add constructively to yield a net magnetization. In the so-called "Voigt geometry" an external magnetic field is applied perpendicular to the propagation direction of the circularly polarized light pulse (along the z-axis). The electron spin ensemble thus enters in coherent superposition of the eigenstates for spin-up and spin-down defined by the external magnetic field. The corresponding energy eigenvalues are

$$E_{\uparrow,\downarrow} = \pm\frac{e\hbar B}{2m_e}. \tag{1.14}$$

The resulting spin splitting can be related to the Larmor frequency ω_L by Eq. (1.12). As the spin states along the z-axis (quantization axis) are energy eigenstates, the application of the time-evolution operator

$$U(t,0) = exp(-iHt/\hbar) = exp(-i\omega_L S_x t/\hbar) \tag{1.15}$$

on the eigenstates $|s_z;\uparrow\rangle$ and $|s_z;\downarrow\rangle$ yields the states themselves independent of time. Along the field axis (longitudinal direction) these quantum-mechanical spin states are thus stationary. Any loss of coherence is induced by coupling of those states with the environment. Applying the time-evolution operator on the spin states perpendicular

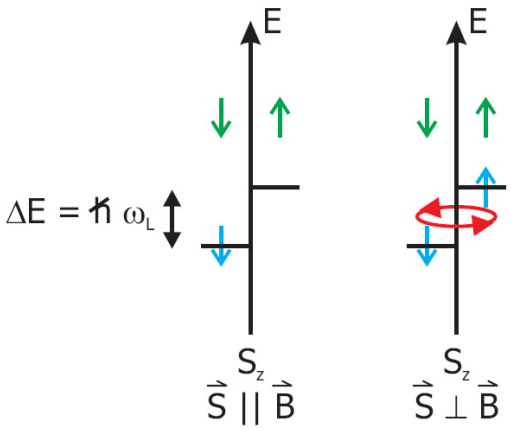

Figure 1.5: Quantum mechanical picture of Larmor precession. Left: The spin is initially aligned along the B-field axis, where the z-component of the spin is an energy eigenstate, which is therefore stationary upon time evolution. Right: Taken the B-field perpendicular to the initial spin alignment leads to a superposition of the spin eigenstates [7].

to the magnetic field direction

$$\begin{aligned} |s_x;\uparrow\rangle &= \frac{1}{\sqrt{2}}[|s_z;\uparrow\rangle + |s_z;\downarrow\rangle] \\ |s_x;\downarrow\rangle &= \frac{1}{\sqrt{2}}[|s_z;\uparrow\rangle - |s_z;\downarrow\rangle] \\ |s_y;\uparrow\rangle &= \frac{1}{\sqrt{2}}[|s_z;\uparrow\rangle + i|s_z;\downarrow\rangle] \\ |s_y;\downarrow\rangle &= \frac{1}{\sqrt{2}}[|s_z;\uparrow\rangle - i|s_z;\downarrow\rangle] \end{aligned} \tag{1.16}$$

yields the following expectation values [9]

$$< S_x >= \frac{1}{2}\hbar\cos(\omega_L t), \quad < S_y >= \frac{1}{2}\hbar\sin(\omega_L t), \quad < S_z >= 0 \tag{1.17}$$

The time-evolution of the spin vector may be viewed semi-classically as the Larmor precession of the classical spin vector in a plane perpendicular to the applied field. This results in an oscillatory cosine projection (Eq. (1.17)) of the electron spin polarization along its excitation direction. Incoherent evolution of the spin wave function results in a decay of the amplitude of the oscillations. Such a decoherence can arise from various scattering events with the enviroment, such as spin-orbit scattering due to impurities or phonons, spin-spin interaction with holes or local magnetic impurities, or finite lifetime effects due to electron-hole recombination .

Quantum-mechanically (see Fig. 1.5), such spin precession can be viewed as arising from the excitation of coherent superposition of the spin states energy split by the magnetic field along the z-direction, which results in quantum beatings between the spin-up and the spin-down eigenstates [10].

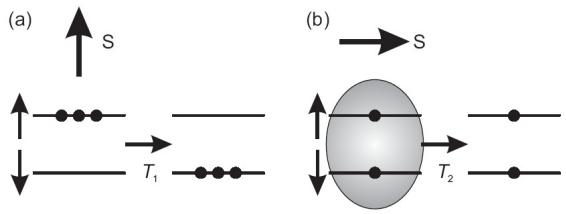

Figure 1.6: (**a**) Schematic illustration of the decay of a non-equlibrium occupation in a two level system characterized by the longitudinal spin relaxation time T_1. Spin-up and spin-down eigenstates are split by a magnetic field. (**b**) Phase coherence between two spin eigenstates. Its decay characterized by the transverse spin coherence time T_2 does not involve a change in the occupation number (after [10]).

1.5.3 Longitudinal and transverse spin coherence.

The non-equilibrium perturbation to the two-level system by ultrafast optical excitation has two important effects: it changes the relative occupation of the two states, and it results in an oscillatory change in the coherence (phase) relation between the two states. The time evolution of these two components of the perturbation is described by the times T_1 and T_2 , the longitudinal and the transverse spin coherence times, respectively. The time T_1 is the time it takes for the longitudinal spin magnetization (along z direction parallel to the magnetic field) to reach equilibrium. The relaxation process requires energy transfer between the spin system and, for example, the lattice by phonons (See Fig. 1.6). In contrast, time T_2 is the transverse decoherence time of the precessing electron spin. This decoherence is a result of a loss of the phase relation between the two eigenstates, which does require neither any energy transfer nor a change in occupation, in contrast to T_1 processes. Note that the T_2 timescale is of direct relevance to coherent spin devices. In the following, it therefore will be focused on experimental techniques to probe the transverse spin coherence time in semiconductors [10].

1.5.4 Spin coherence and spin dephasing

The above definition of spin coherence refers to a single electron spin. Experimentally, such a single electron spin is usually not accessible. Instead, in optical experiments a whole ensemble of electron spins $\sim 10^{15}$ electron per cm^3 is coherently excited [10]. Only if all conduction electrons were identical and non-interacting, then the transverse decay of net spin magnetization would reflect the intrinsic spin decoherence time of individual electrons. However, in addition to such homogeneous decoherence, there might be inhomogeneous effects such as local magnetic fields or local variations in the electron g-factor. In such local inhomogeneous magnetic fields different electron spins precess at different rates, which lead to an extra decay or dephasing of the net spin polarization. This results in a spreading of the relative spin orientations within the electron distribution, even when all spins are evolving coherently. In principle,

this dephasing effect can be distinguished from decoherence as in case of dephasing it remains possible to recover the initial macroscopic spin magnetization (an example being spin echo experiments in nuclear magnetic resonance). As spin echo techniques in time-resolved optical measurements are rarely utilized, the measured transverse spin decay is usually called a transverse spin dephasing time T_2^* , which is a lower bound to the actual transverse spin coherence time T_2 unless inhomogeneous effects can be eliminated. In general, inhomogeneous and homogeneous processes contribute to T_2^* according to

$$\frac{1}{T_2^*} = \frac{1}{T_2} + \frac{1}{T_2^{inh}} \tag{1.18}$$

where $1/T_2$ and $1/T_2^{inh}$ are the homogeneous and the inhomogeneous spin relaxation rates, respectively. As an example, inhomogeneous dephasing caused by a spread Δg in the electron g-factors is given by

$$\frac{1}{T_2^{inh}} = \frac{1}{T_{\Delta g}} = \frac{\Delta g \mu_B B}{\sqrt{2}\hbar} \tag{1.19}$$

However, such a simple relationship is usually not observed experimentally [11].

1.5.5 Homogeneous spin dephasing

Homogeneous spin dephasing occurs in scattering events, where the macro spin vector changes its direction and/or its magnitude by transferring its angular momentum to other scattering partners. The probability for such an event to happen is the same for all spins with identical properties within a "homogeneous" spin ensemble. The net change of spins loosing their coherence dN/dt to the total number of spins $N(t)$ at time t is then

$$\frac{dN}{dt} = -\frac{1}{T_2} N(t)$$

$$N(t) = N_0 \exp\left(-\frac{t}{T_2}\right) \tag{1.20}$$

where $N_0 = N(0)$ is the number of spins at time $t = 0$. Thus, homogeneous dephasing is in general characterized by a simple exponential decay. However, as soon as this sample rate ansatz is no longer valid, other time dependencies may appear. One of these exceptions is spin dephasing via nuclear hyperfine interaction [10].

1.5.6 Hole spin coherence

The experimental observation of the spin coherence of holes is difficult. But as well as in case of the spin coherence of electrons, it can be observed in a pump-probe Kerr rotation. The main idea of these method will be given in Chapter 2. The problem of the hole spin coherence observation has few reasons. First, due to zero in-plane spin component of the heavy holes, they can not perform precession about(around) in-plane magnetic field. Applying tilted magnetic field allows one to observe the hole

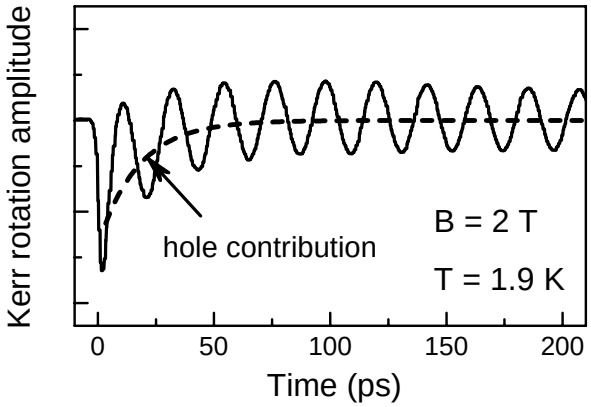

Figure 1.7: Time-resolved Kerr rotation signal measured on a n-type CdTe/$Cd_{0.78}Mg_{0.22}$Te quantum well. The laser is resonant with the trion energy. The experimental data are shown by the solid line. The dashed line gives the exponentially decaying part of the centre-of-gravity of the electron spin beats which is assigned to the hole spins in the trions [12]

spin beats, which however have a long period. Only a few oscillations periods can be usually observed during the hole dephasing time [13, 14]. Second reason relates to considerably stronger the spin-orbit interaction in the valence band than in the conduction band and as result efficiency of the spin relaxation is higher for free holes. The spin relaxation time of holes strongly depends on the doping density and excitation energy. Localization of holes suppresses the most spin relaxation mechanism inherent for free carriers. Even interaction between holes and the nuclear spins is damped [15]. That is why, a long spin coherence time for holes is expected. The lifetime of the photogenerated holes in n-type quantum wells is limited by recombination. It can exceed even a few hundred picoseconds for non-resonant excitation of quantum wells (see [13]). For non-resonant excitation of quantum wells it can last up to a few hundreds of picoseconds [13], but for resonant trion excitation it does not exceed a few tens of picoseconds. In the latter case, which is typical for pump-probe Kerr rotation experiments, the spin dynamics of holes bound to trions can be seen as an asymmetric shift of the centre-of-gravity of the electron oscillations. In Fig. 1.7 is shown an example of such behavior, observed in an n-type CdTe/$Cd_{0.78}Mg_{0.22}$Te quantum well (for details see Ref. [14]). The decay of this shift on a time scale of about 20 ps (dashed line) is contributed by hole spin dephasing and by trion recombination. The separation of these both contributions as wells as extraction of the spin dephasing time are quite difficult. The lifetime of the resident holes in p-type quantum wells is infinitely long, what makes these structures attractive for studies of the hole spin coherence. Here are briefly described, the main theoretical and experimental results for a 15-nm-thick GaAs/$Al_{0.34}Ga_{0.66}$As quantum well ($n_h = 1.51 \times 10^{11}$ cm^{-2}), observed in the Ref. [14]. The Kerr rotation signal for resonant excitation of the positively charged trion is shown by the upper curve in Fig. 1.8(a). It consists of two coherent signals. After decomposition by a fit, the two contributions are shown in panel (a). The one with a faster precession frequency corresponds to $\mid g_e \mid = 0.285$, which is typical

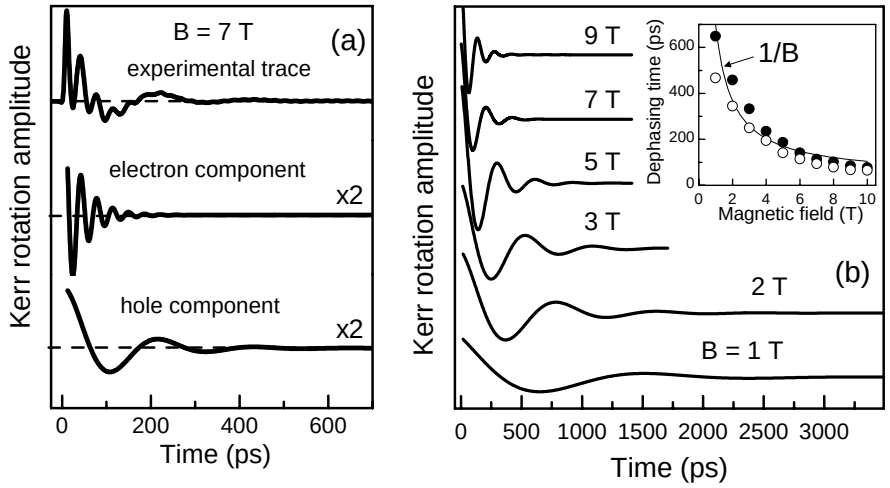

Figure 1.8: Kerr rotation traces for a p-type 15-nm-thick GaAs/(AlGa)As quantum well. The magnetic field was tilted by $\vartheta = 4°$ out of the quantum well plane. The laser energy of 1.5365 eV is resonant with T^+. The powers were set to 5 and 1 W/cm^2 for pump and probe, respectively. (**a**) Top trace is the measured signal. Bottom traces are obtained by separating electron and hole contributions. (**b**) Hole component extracted from a fit to the Kerr rotation signals at different magnetic fields. The inset shows the magnetic field dependence of the hole spin dephasing time T_2^*. The solid line is a $1/B$ fit to the data. The closed and open circles are data measured for pump to probe powers of 1 to 5 W/cm^2 and 5 to 1 W/cm^2, respectively. $T = 1.6$ K [14]

for electrons in GaAs-based quantum wells. It is observed only during ~ 200 ps after pump arrival and decays with a time of 50 ps, which coincides with the lifetime of the resonantly excited T^+. The other contribution with a small precession frequency is assigned to the hole spin beats. In a magnetic field of 7 T they decay with a time of about 100 ps. The hole beats can be followed up to 500 ps delay. At these long times the Kerr rotation signal is solely due to the coherent hole precession [16].

Experimentally it is difficult to observe the hole spin quantum beats due to the very small in-plane hole g-factor. To enhance the visibility, the magnetic field was tilted slightly out of plane by an angle $\vartheta = 4°$ to increase the hole g-factor by mixing the in-plane component ($g_{h,\perp}$) with the one parallel to the quantum well growth axis ($g_{h,\parallel}$), which typically is much larger: $g_h(\vartheta) = (g_{h,\parallel}^2 \sin^2\vartheta + g_{h,\perp}^2 \cos^2\vartheta)^{1/2}$. For the studied structure $\mid g_{h,\perp} \mid = 0.012 \pm 0.005$ and $\mid g_{h,\parallel} \mid = 0.60 \pm 0.01$ [14]. Figure 1.8(b) shows the hole contribution to the Kerr rotation signal for different magnetic fields. The hole spin dephasing time T_2^* is plotted versus B in the inset. A long-living hole spin coherence with $T_2^* = 650$ ps is found at $B = 1$ T. With increasing B up to 10 T it shortens to 70 ps. The field dependence is well described by a $1/B$-form, from which we conclude that the dephasing shortening arises from the inhomogeneity of the hole g-factor $\Delta g_h = 0.007$. The hole spin dephasing time decreases drastically by elevating the lattice temperature to 5-10 K [14]. The main reason for that is hole delocalization, which activates spin relaxation caused by the spin-orbit interaction.

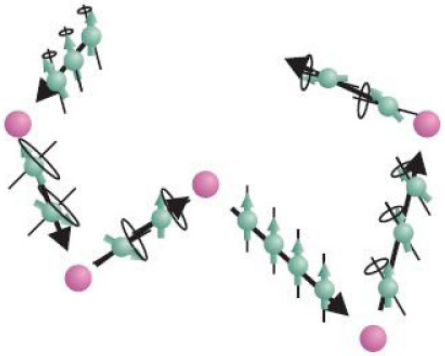

Figure 1.9: Sketch of the Dyakonov-Perel spin dephasing mechanism. Through the lifting of the spin degeneracy in non-centrosymmetric crystals an effective magnetic field $\vec{B}(\vec{k})$ acts on the electron spins, causing them to precess. After each momentum scattering event, precession frequency and axis change, which leads to spin dephasing (after [10]).

1.6 Mechanisms of spin relaxation

Four mechanisms for spin relaxation of conduction electrons have been found relevant for metals and semiconductors: the Elliott-Yafet, Dyakonov-Perel, Bir-Aronov-Pikus, and hyperfine-interaction mechanisms.

Elliot-Yafet mechanism

Elliot (1954) first suggested that electron spin relaxation occurs via momentum scattering. In the ElliottYafet mechanism, spin flip of an electrons results from the spin-orbit interaction in the process of scattering.

Dyakonov-Perel mechanism

The Dyakonov-Perel (or precession) mechanism is the main mechanism of electron spin relaxation in bulk semiconductors and semiconductor quantum wells (QWs). It is connected with the spin-orbit splitting of the conduction band states which acts as an effective magnetic field with the Larmor precession frequency $\mathbf{\Omega_k}$ dependent on the value and direction of the electron wave vector ($\mathbf{k}$) (see Fig. 1.9) [17]. Such an effective field arises only in noncentrosymmetric systems, the most widespread examples of them being bulk III-V semiconductors and QWs on their base.

The spin relaxation rate can be estimated as

$$\tau_s^{-1} \propto \langle \mathbf{\Omega_k^2} \tau \rangle \tag{1.21}$$

where angular brackets denote the averaging over the electron ensemble and τ is the microscopic scattering time. Hence, the spin relaxation is slowed down by the scattering. It is evident that any momentum scattering process such as interaction of an electron with static impurities, interface imperfections or phonons stabilizes the spin [17]. Glazov and Ivchenko [17] were the first to note that the inverse relaxation time τ^{-1} is the sum of contributions due not only to various momentum-scattering mechanisms

(which control the carrier mobility), but also to electronelectron collisions (which do not change the mean electron quasimomentum). Indeed, it does not matter whether a change in k (and the corresponding change in the axis of Larmor precession) is due to the scattering by a static defect or a phonon, or due to cyclotron motion of free carriers in magnetic field, or it is caused by a collision with another electron [18]. In particular, this implies that there exists a natural upper limit of spin relaxation rate in high-quality structures: In particular, this implies that there exists a natural upper limit of spin relaxation rate in high-quality structures [17]:

$$\tau_s^{-1} \leq \langle \mathbf{\Omega_k^2} \rangle \tau_{\mathbf{ee}}^{(\mathbf{s})}, \tag{1.22}$$

where the time scale $\tau_{ee}^{(s)}$ characterizing the electronelectron collision frequency.

An interesting anisotropy appears, if $\mathbf{k}$ is restricted to the plane of a quantum well ($\mathbf{k} \rightarrow \mathbf{k}^{\|}$). The spin relaxation time τ_s^{DP} of two-dimensional confined electron spins in a zinc-blende semiconductor is given by [19]

$$\tau_s^{DP} \propto T^{-1} E_g d^{-2} E_1^{-2} \tau_p^{-1} \tag{1.23}$$

where T is the temperature, E_1 the quantized kinetic energy of electrons in the first subband, and E_g and d are the band gap and the width of the quantum well (QW), respectively. It is assumed that the spin splitting $\mathbf{\Omega_k}$ is determined by the Dresselhaus term. Since $\mathbf{\Omega_k}$ depends on the electron momentum direction, the DP mechanism can be influenced by the QW's confinement direction. In (001)-oriented QWs, $\mathbf{\Omega_k}$ lies in the plane of the QW and changes its direction with $\mathbf{k}^{\|}$. For (001)-oriented QWs, the relaxation time of spins pointing in an in-plane direction ($\tau_s^{\|}$) and in the out-of-plane direction ($\tau_s^{\perp}$) is given by $\tau_{s(001)}^{\|} = \tau_s^{DP}$ and $\tau_{s(001)}^{\perp} = \tau_s^{DP}/2$, respectively. If the QW is grown in the [110] lattice direction, the times change to $\tau_{s(110)}^{\|} = 4\tau_s^{DP}$ and $\tau_{s(110)}^{\perp} = \infty$. For the latter orientation, $\mathbf{\Omega_k}$ ($\mathbf{k}^{\|}$) points in the growth direction for all $\mathbf{k}^{\|}$. Spins oriented normal to the QW plane are thus not affected by $\mathbf{\Omega_k}$ and the DP spin relaxation becomes totally suppressed, when higher order terms in $\mathbf{k}$ are neglected [20]. The suppression of the DP relaxation for out-of-plane spins explains the large spin dephasing anisotropies found in (110)-oriented QWs [21, 22]. In the presence of the Rashba term the spin relaxation in the plane of [001]-grown quantum wells is anisotropic [23, 24].

Bir-Aronov-Pikus mechanism

The spin of hole can be exchange with conduction electrons. These exchanges proceed through scattering and lead to spin relaxation of conduction electron in p-doped semiconductors [25]. Holes have shorter spin coherence time and spin exchange between electrons and holes is very effective. Ultimately, it will leads to spin decoherence. This mechanism is of importance at low temperatures [26].

Hyperfine-interaction mechanism

Hyperfine-interaction comes from the magnetic interaction between the magnetic momentum of nuclei and electrons. In semiconductor heterostructures, this mechanism

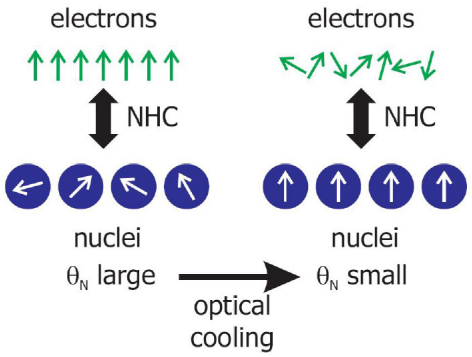

Figure 1.10: Sketch of spin dephasing through nuclear hyperfine coupling. Left: An initially spinpolarized electron system couples to nuclear spin system. Right: After dynamic nuclear polarization through the electrons the nuclear spin system has cooled down, while the electron spin polarization has decreased [7].

is responsible for spin dephasing of localized or confined electron spins [10]. Electrons in the conduction band have s-type wave function, and the hyperfine interaction can be written as

$$H_{HF} = AV\mathbf{I} \cdot \mathbf{S}\delta(\mathbf{r}) \tag{1.24}$$

where A is the couplin constatnt and V the unit cell volume. Fishmann and Lampel [**?**] calculated the spin relaxation rate due to hyperfine coupling (NHC) (see Fig. 1.10) as

$$\frac{1}{\tau_S^{NHC}} = \frac{2}{3} N_N (AV)^2 \left(|\Psi(0)|^2 V\right)^2 I(I+1) \frac{\sqrt{2(m^*_{CB})^3 E_{kin}}}{2\pi\hbar^4} \tag{1.25}$$

Therein, N_N is the density of nuclei, while Ψ and m^*_{CB} are the electronṡ wave function and effective mass, respectively. The nuclear polarization $\mathbf{I}$ induces an additional local magnetic field for the electrons. Since Kerr/Faraday rotation directly measures the Larmor frequency of the electron spins, it can be used an indirect probe of the nuclear spin polarization. In experiments on dynamical nuclear polarization (DNP) the non-equilibrium electron spin population can thermally equilibrate, in part by flipping nuclear spins, thereby transferring angular momentum to the nuclear system (Fig. 1.10). DNP has been observed in bulk semiconductors as well as in semiconductor heterostructures [27]. In this thesis the DNP effects are described in Chapter 4.

1.7 Optical generation of spin coherent carriers

In this work we use a time-resolved pump and probe technique. This technique uses ultra-short laser pulses as short as $\sim$ 100 fs and provide us the ability to study carrier spin coherence. In the figure 1.11 are displayed three different situations taking place in experiments on the coherent spin dynamics in quantum wells under resonant optical excitation. The difference between these cases lies in the density of resident 2D electrons, n_e. In undoped samples (panel (a), $n_e = 0$) spin oriented excitons are photogenerated. In this case the coherent spin dynamics of either an exciton or an electron

in the exciton can be measured depending on the experimental details. However, this dynamics can be monitored only during the exciton lifetime, which is typically in the range from 30 ps to 1 ns [16].

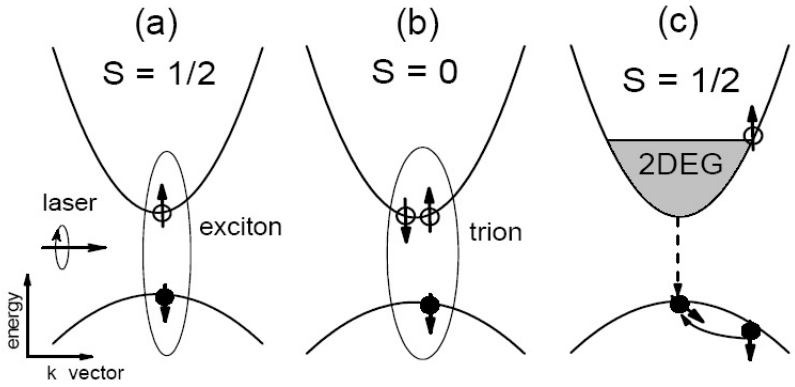

Figure 1.11: Schematic presentation of generation of carrier spin coherence by circular polarized laser pulses. The three cases differ with respect to the density of the 2DEG in the quantum well: (**a**) empty well, only photogenerated carriers are present, which become bound to form excitons; (**b**) low density 2DEG, trions with a singlet ground state are formed by a photogenerated exciton and a background electron. The interaction of the trion with the 2DEG is negligible; (**c**) dense 2DEG with a Fermi energy exceeding the exciton binding energy. Bound complexes such as excitons and trions are suppressed [28].

For high density 2DEGs (panel (c), $n_e a_B^2 > 1$, where a_B is the exciton Bohr radius), exciton formation is suppressed because of state-filling and screening effects. After photogeneration the hole looses its spin and energy and recombines with an electron from the Fermi see. However, the spin oriented electron photogenerated at the Fermi level has infinite lifetime, which allows one to study its long-lived spin coherence. As a result, a circularly polarized photon can change the spin polarization of the 2DEG by $S = \pm 1/2$ [28].

In case of diluted 2DEGs (panel (b), $n_e a_B^2 \ll 1$) the mechanism for generation of electron spin coherence is not so obvious. The lowest in energy optical transition corresponds to a negatively charged exciton (trion), which consists of two electrons and one hole [29]. The ground state is a singlet trion with antiparallel orientation of the electron spins. When excited resonantly, this state does not contribute directly to the spin polarization because the hole undergoes fast decoherence and the total spin of the two electrons is $S = 0$. However, generation of electron spin coherence has been observed experimentally under resonant excitation of trions, both for quantum wells [28, 30] and quantum dots [31]. There are two equivalent approaches to explain this generation, which are detailed described in the work Ref. [28]. The first one suggests that a coherent superposition of electron and trion states is excited by a circular polarized light pulse when the system is subject to an external magnetic field [31, 30, 32]. The second one is based on considering the 2D electrons which are involved in the trion formation: under circular polarized excitation electrons with a specific spin

orientation will be taken from the 2DEG and, consequently, spin polarization with opposite sign is induced [28]. More detailed explanations you can find in the Ref. [28].

Chapter 2

Experimental setup and samples

The goal of the experimental results presented in this work is to study the influence of the electronic states of spin-polarized electrons in quantum well heterostructures on the spin coherence and dephasing in the time domain. Time-resolved spectroscopy is therefore the method of choice.

In the recent years the field of ultrafast spectroscopy of semiconductors based on the femtosecond laser pulses technique became a very active field of research. It brings fundamental information about nonequilibrium, nonlinear and transport properties of semiconductors and semiconductor nanostructures. More concrete, this kind of spectroscopy provides the best means of determining the distribution functions of excitations, and hence determining the dynamics of the relaxation of these excitations. Besides, this technique provides the ability to investigate the nonlinear properties, including coherent effects and thus provides insights into yet different aspects of semiconductors, such as many-body effects, coherent effects and dephasing phenomena.

We discuss here only in this work used technique pump-probe spectroscopy. This is the most common form of ultrafast spectroscopy.

2.1 Time-resolved magneto-optics: experimental methods

2.1.1 The magneto-optical Kerr effect

In order to probe the net magnetization of optically oriented electron spins, magneto-optical techniques are used which either measure the Kerr or Faraday rotation. The measurements of the rotation of the polarization of the probe pulse transmitted (Faraday rotation) through or reflected (Kerr rotation) from the semiconductor nanostructure are used to monitor the time evolution of the electron magnetization induced by the pump pulse [10].

In both cases the resulting polarization is no longer strictly linear but rather slightly elliptic. Both effects can theoretically be described by Maxwells equations through off-

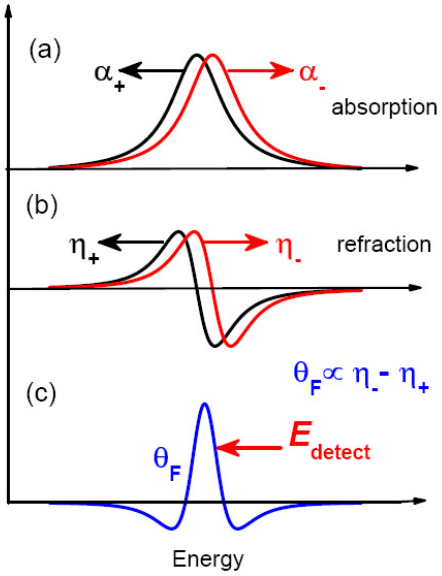

Figure 2.1: (**a**) Idealized Zeeman-split absorption resonance (α_+,α_-) corresponding to right (σ^+) and left (σ^-) circularly polarized light. (**b**) Associated indices of refraction (η_+, η_-). (**c**)Resonant Faraday rotation [10]

diagonal elements of the dielectric tensor. The strength of the polarization rotation is strongly enhanced in the spectral vicinity of optically-allowed band-to-band transitions [10]. The origin of the large resonant Faraday rotation in semiconductors is the Zeeman effect. In (100) GaAs this corresponds to to the well-known (spin-up and spin-down) splitting of the s-state conduction band electrons, and the fourfold splitting of the p-type valence band into spin-up and spin-down light- and heavy-holes. Thus the optical transition associated with left and right circularly polarized light are split in energy [10]. Consider two such Zeemans-split states whose absorption resonances appear as shown in Fig. 2.1(a) assuming a Lorentzian lineshape for simplicity. Their associated indices of refraction which are also split in energy (Fig. 2.1(b)) give rise to a large resonant Faraday rotation shown in Fig. 2.1(c) through the relation

$$\Theta_F(\omega) \propto \eta_-(\omega) - \eta_+(\omega). \tag{2.1}$$

In practice, the spectral shape of the Faraday resonance strongly depends on the exact lineshape of the absorption edges and is rarely so symmetric [10].

2.1.2 Time resolved Kerr/Faraday rotation

In order to describe the KR in the pump-probe experiment under normal-incidence resonant excitation, one has firstly to consider the amplitude reflection coefficient of an axially-symmetric single QW, which in the vicinity of the exciton or trion resonance is given by [33]

$$r_{QW}(\omega) = \frac{\mathrm{i}\Gamma_0}{\omega_0 - \omega - \mathrm{i}(\Gamma_0 + \Gamma)}\,, \tag{2.2}$$

where ω is the incident light frequency and ω_0, Γ_0 and Γ are the exciton (trion) resonance frequency, the radiative and the nonradiative damping rates, respectively. Taking into account also the cap layer as constituent of the heterostructure, the total amplitude reflection of the light incident on the structure from vacuum reads [34]

$$r = \frac{r_{01} + r_{QW}\mathrm{e}^{2\mathrm{i}\phi}}{1 - r_{10}r_{QW}\mathrm{e}^{2\mathrm{i}\phi}} , \tag{2.3}$$

Here $r_{01} = -r_{10} = (1 - n_b)/(1 + n_b)$ is the reflection coefficient at the boundary between the cap layer and vacuum, n_b is the refractive index of the cap layer which for simplicity is assumed to coincide with the background refractive index of the well material, $\phi = k_b b$, b is the cap-layer thickness and k_b is the light wave vector in the cap-layer. The above equation is valid for a spin-unpolarized system in which case the coefficient r is insensitive to the light polarization. For the spin-polarized resident electrons the reflection coefficient for right (+) and left (−) circularly polarized light has the form of Eq. (2.2) but r_{QW} is replaced by [34]

$$r_{QW,\pm}(\omega) = \frac{\mathrm{i}\Gamma_{0,\pm}}{\omega_{0,\pm} - \omega - \mathrm{i}(\Gamma_{0,\pm} + \Gamma_{\pm})} \tag{2.4}$$

with the parameters ω_0, Γ_0 and Γ dependent on the light helicity. These parameters are, in general, determined by the concentration and spin polarization of the carriers and their complexes as well as by the delay between the pump and probe pulses. When describing the Faraday rotation effect we have to analyze the amplitude transmission coefficient $t_{QW,\pm}(\omega) = 1 + r_{QW,\pm}(\omega)$. Both the two signals measured in reflection (Kerr rotation) or transmission (Faraday rotation) geometry are proportional to the difference [34]

$$\Sigma_+ - \Sigma_- = \Sigma_0 \mathrm{Im}\{r_+^* r_-\} , \tag{2.5}$$

where Σ_0 where Σ_0 and $\Sigma_\pm$ are the time-integrated intensities of the incident and reflected/transmitted probe pulses in time-resolved experiments (or the stationary intensities under steady-state photoexcitation) [34]. A typical beam arrangement for time-resolved Faraday (TRFR) and Kerr (TRKR) rotations is presented in Fig. 2.2. The pump and the probe beam are at almost normal incidence to the sample, and the polarization rotation of the transmitted and the reflected probe beam is simultaneously monitored as the pump-probe delay Δt is varied. Thus the polar component of the magnetization (which is normal to the sample) is measured [10]. Fig. 2.3 schematically shows the oscillatory Faraday or Kerr response at a non-zero transverse magnetic field. The oscillations appear at the Larmor frequency ω_L directly proportional to the energy splitting $\Delta E = \hbar\omega_L$ between the two eigenstates parallel and antiparallel to the field. This frequency is a direct measure of the electron g-factor, $g = \hbar\omega_L/\mu_B B$. Homogeneous spin dephasing leads to an exponentional decay of the optically induced magnetization. Combining both spin dephasing and spin precession thus leads to an exponentially decaying cosine function of the Faraday/Kerr rotation angle [10]

$$\Theta_{K,F} = \Theta_0 \cdot e^{\frac{-\Delta t}{T_2^*}} \cos(\omega_L \Delta t) \tag{2.6}$$

with

$$\omega_L = g\mu_B/\hbar. \tag{2.7}$$

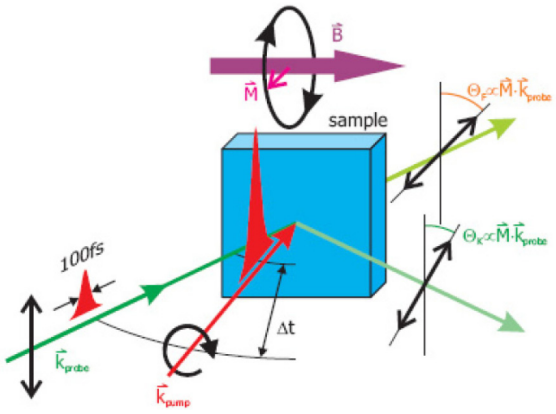

Figure 2.2: Time-resolved pump-probe setup. The coherent spin ensemble is generated by a circularly polarized pump pulse. Spin precession is obtained by a transverse external magnetic field (Voigt geometry). The projection of magnetization along the probe direction is measured through the Faraday (Θ_F) and the Kerr effect (Θ_K) at various pump-probe delays Δt [10]

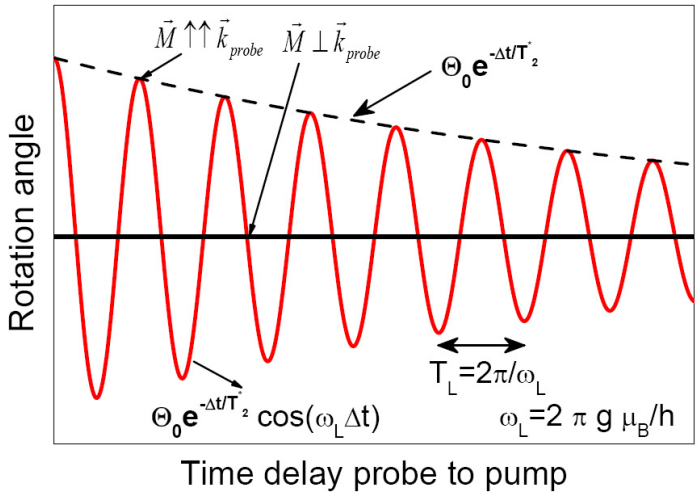

Figure 2.3: Schematic curve of the time-resolved Faraday/Kerr rotation. The envelope is caused by the spin relaxation, whereas the periodic cosine stems from the precessional rotation.

2.2 Resonant spin amplification

The above delay-line technique only offers to determine spin dephasing times of up to about three times the scan length. Another problem arises if the spin lifetime is significantly longer than the laser repetition interval, which is on the order of $T_R = 12.5$ ns. In this case a new pump pulse coherently excites an additional spin ensemble before the previous ensemble has completely dephased [10]. Such a situation is depicted in Fig. 2.4: Depending on the Larmor frequency and the laser repetition rate, the subsequently injected spin can interfere constructively with the existing spins, if the spin ensemble has precessed an integer number of times. Since this happens not only for

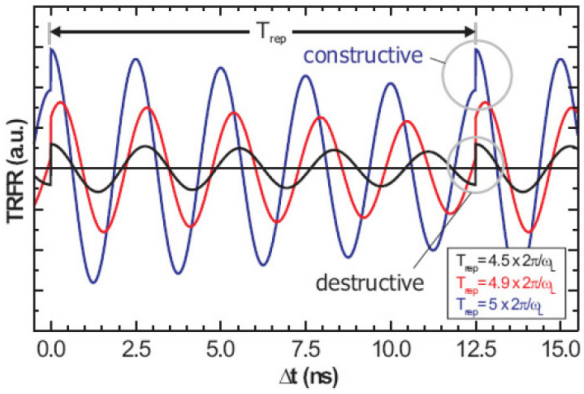

Figure 2.4: The formation of the RSA peaks stems from constructive interference of the precessing spins with freshly injected spins at $\Delta t = 0$. The image shows a simulation with g = -0.42 and T_2 = 30 ns while the Laser repetition interval is T_R = 12.5 ns. Delay-line scans for different magnetic fields are displayed, so that the repetition interval equals 4.5, 4.9 and 5 Larmor precessions, respectively [10]

the latest spin ensemble, but also for its predecessors, all these spins are in resonance. However, if the spin precession does not exactly fit into the repetition interval, this resonance is greatly suppressed [10]. This can be understood in the following way: Even if the most recently created spin ensemble is only slightly off the resonance condition, its predecessor is already twice off, and so on. So the net magnetization is noticeably reduced [10]. In the extreme case when the spin ensemble has precessed a half-integral number of times, they will be aligned in the opposite direction to the newly injected spins, which leads to a destructive interference of the net spin population [10]. From mathematical point of view, one simply adds up all previous laser excitations with their respective exponentially damped Larmor precessions. The magnetization then becomes

$$M_s(\Delta t, \omega_L) = \sum_{n=1}^{\infty} M_0 \exp\left[-\frac{(\Delta t + nT_R)}{T_2^*}\right] \cos\left[\omega_L(\Delta t + nT_R)\right] \tag{2.8}$$

The convergence of this sum is guaranteed as long as the spin lifetime is finite. This formula can be written in a closed form as [7]

$$M_s(\Delta t, \omega_L) = \frac{M_0}{2} \exp\left[-\frac{(\Delta t + T_R)}{T_2^*}\right] \cdot \frac{\cos(\omega_L \Delta t) - \exp\left[T_R/T_2^*\right] \cos\left[\omega_L(\Delta t + T_R)\right]}{\cos(\omega_L T_R) - \cosh(T_R/T_2^*)} \tag{2.9}$$

with $\Delta t \in [-T_R; 0)$ and $\omega_L = g\mu_B B/\hbar$. In experiments, T_R is usually fixed while the Larmor frequency can be varied by the external magnetic field. Therefore in a resonant spin amplification RSA measurement the delay line is hold constant while the B field is being swept [35]. Whenever the resonance condition is met a sharp resonance peak appears as it is shown in Fig. 2.5.

If the spin dephasing time is only about half of the repetition interval, the resonance peaks degrade to a sinusoidal modulation of the magnetization. However, RSA can

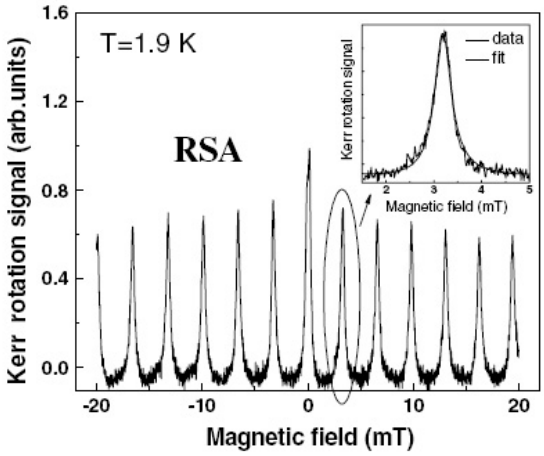

Figure 2.5: (**a**) Typical RSA scan for a 20-nm-thick CdTe/$Cd_{0.78}Mg_{0.22}Te$ quantum well at $T = 6$ K as taken by time-resolved Kerr rotation while sweeping the external magnetic field. The pump-probe delay is fixed at $\Delta t = -100$ ps. The broadening of the RSA peaks with increasing field reflects a decrease in the spin dephasing time. The peak distance corresponds to one Larmor precession during the laser repetition interval. (**b**) Part of the fit to RSA data. The spin dephasing time exceeds $T_2^* = 30$ ns at $T = 1.9$ K [29]

already be used for spin dephasing times exceeding 8 ns. The longest detectable lifetimes using this method in our experiments were observed for CdTe quantum well and exceed $T_2^* = 30$ ns at $T = 1.9$ K (see Fig. 2.5) and $T_2^* = 55$ ns for (In,Ga)As quantum well of the sample #11708 at $T = 2$ K.

Until now, we described the RSA measurement to detect spin lifetime of the electrons. In work of Ref. [36], was shown, that the RSA signal carries not only information on the electron spin relaxation but also on its generation, from which one can obtain information on the hole spin relaxation. This allows us to measure hole spin relaxation times exceeding by orders of magnitude their lifetimes. Panels (a) and (b) in the Fig. 2.6 give RSA signals recorded at the exciton and trion energies for $T = 2$ K. The probe pulse hit the sample at a delay of $(T_R - \delta)$ with $\delta = 10$ ps shortly before the pump pulse[35]. The shape of the exciton RSA curve in panel (a) agrees with RSA curves reported in literature [37, 16]. The peak positions correspond to electron spin precession frequencies which are multiples of the laser repetition frequency. The decrease of the peak amplitude with increasing magnetic field is due to the ensemble spread of electron g-factor. The RSA spectrum obtained for resonant trion excitation strongly differs from the exciton signal, see panel (b). First (and most important), the amplitude of the peaks increases with increasing magnetic field in contrast to a conventional RSA signal. Second, the peaks are inverted due to spectral dependence of the signal phase, as discussed in [40]. Third, the signal between peaks at $T = 2$ K is asymmetric.

Spin coherence of quantum well electrons was generated by optical excitation of the trion transition. The time evolution of the Faraday rotation signal, resulting from this type of excitation, is controlled by the interdependence of electron and hole spin

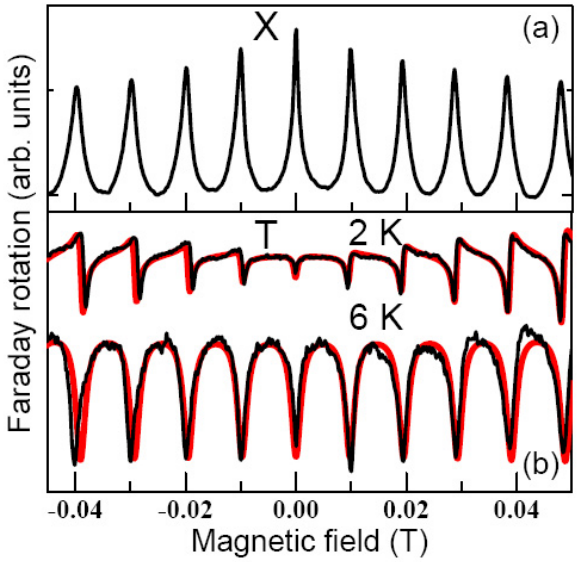

Figure 2.6: (**a**) RSA signal for exciton resonance of 8-nm-thick $In_{0.09}Ga_{0.91}As$ quantum well (sample #11307). (**b**) RSA signal for trion resonance. Black (red) curves give experiment (theory). Calculation parameters are $|g_e| = 0.555$ and $\Delta g_e = 0.002$. For upper curve: $T_s^e = 55$ ns, $T_s^h = 2$ ns, and $\tau_r = 120$ ps. For lower curve: $T_s^e = 20$ ns, $T_s^h = 0.2$ ns, and $\tau_r = 100$ ps. In all panels $T = 2$ K, except of lower trace in (d) with $T = 6$ K [36]

dynamics. As a result traces of the hole spin can be found in the electron RSA long after the radiative trion decay.

For a quantitative analysis, the spin states of the resident electron and singlet trion (hole) has been described by polarization vectors $\boldsymbol{s}$ and $\boldsymbol{j}$, respectively. The coupled dynamics of these polarizations in magnetic field can be seen from their equations of motion [41, 42, 43]:

$$\frac{d\boldsymbol{j}}{dt} = -\frac{\boldsymbol{j}}{T_s^h} - \frac{\boldsymbol{j}}{\tau_r} \equiv -\frac{\boldsymbol{j}}{\tau_T}, \tag{2.10}$$

$$\frac{d\boldsymbol{s}}{dt} = \frac{g_e \mu_B}{\hbar}(\boldsymbol{B} \times \boldsymbol{s}) - \frac{\boldsymbol{s}}{T_s^e} + \frac{(\boldsymbol{j}\boldsymbol{z})\,\boldsymbol{z}}{\tau_r} \tag{2.11}$$

Here $\boldsymbol{z}$ is the unit vector along z-axis, μ_B is the Bohr magneton, and g_e is the electron g-factor. We neglect the Larmor precession of the hole spin because the in-plane hole g-factor is close to zero [44, 45]. In both equations phenomenological terms describing relaxation processes are included. In Eq. (2.10) the loss of trion polarization due to hole spin relaxation (T_s^h) and trion recombination (τ_r) are taken into account, resulting in a trion spin lifetime $\tau_T = T_s^h \tau_r / (T_s^h + \tau_r)$. Equation Eq. (2.11) describes the electron spin precession in magnetic field (first term), the decrease of spin polarization due to spin relaxation (T_s^e, second term) and the change of electron spin polarization by trion recombination (third term). Note that the lifetime of the trion spin polarization is limited by the recombination time τ_r (fractions of a nanosecond), whereas the lifetime of the resident electron polarization is limited only by its spin relaxation time, T_s^e.

The reason for that is that the resident electrons contributing to the FR signal are not bound to trions. The trion spin relaxation and recombination control only the generation efficiency of electron spin coherence, but do not influence its decay. Solution of Eq. (2.10) gives $j_z(t) = j_{z0} \exp(-t/\tau_T)$ with the initial value j_{z0}. The reference time zero coincides with the end of the pump pulse.

Besides depending on pump power, j_{z0} depends also on the resident electron spin state, which has to be antiparallel to the photocreated electron. Denoting the z-component of the resident electron spin polarization right before pump pulse arrival at time $t \to T_R$ (i.e. $\delta \to 0$), by $\widetilde{s_z}$, j_{z0} is given by $(2\widetilde{s_z}+1)\sin^2(\Theta/2)/4$ for σ^+ polarized excitation [41, 43]. Here the pump power is expressed in terms of the pulse area $\Theta = \int 2|\langle d\rangle E(t)|dt/\hbar$, where $\langle d\rangle$ is the dipole transition matrix element, and $E(t)$ is the electric field of the laser pulse. In our experiment the pump efficiency was small, so that j_{z0} is approximately proportional to the pump power.

For solving Eq. (2.11) we introduce $s^+ = s_z + is_y$, for which we obtain with $s_0^+ = s_{z0} + is_{y0}$ at time zero:

$$s^+(t) = \left(s_0^+ - \frac{j_{z0}}{\tau_r \Omega}\right) \exp\left[-\left(i\omega_e + \frac{1}{T_s^e}\right)t\right] + \frac{j_{z0} e^{-t/\tau_T}}{\tau_r \Omega}, \tag{2.12}$$

where $\Omega = 1/T_s^e - 1/\tau_T + i\omega_e$, and the electron spin precession frequency $\omega_e = g_e \mu_B B/\hbar$. s_0^+ is determined by the pump intensity and the resident electron spin polarization $\widetilde{s_z}$ and $\widetilde{s_y}$ shortly before the pump [41, 43]:

$$\begin{aligned} s_{z0} &= \widetilde{s_z}(1 - \sin^2(\Theta/2)/2) - \sin^2(\Theta/2)/4, \\ s_{y0} &= \widetilde{s_y}\cos(\Theta/2). \end{aligned} \tag{2.13}$$

In strong magnetic fields ($\omega_e >> 1/\tau_r$) the trion contribution to $s^+(t)$ [terms proportional to j_{z0} in Eq. (2.12)] is negligible due to fast dephasing in the electron spin ensemble, which removes completely the electron signal at $T_R - \delta$ delays [46]. However, in weak magnetic fields this contribution becomes important. From Eq. (2.12) strong oscillations appear in the FR signal after pump pulse action due to electron spin precession about the magnetic field. These oscillations decay with the electron spin relaxation time T_s^e.

An infinite sequence of pump pulses with repetition period T_R creates an electron spin polarization periodic in time [42, 46]. When the first pulse arrives at time zero, $\widetilde{s}_{y(z)} = s_{y(z)}(nT_R - \delta)$, $\delta \to 0$, before action of the $(n+1)$-th pulse. After an extended pulse sequence ($n \to \infty$), $s_z((n+1)T_R - \delta)$ should be equal to $s_z(nT_R - \delta)$, so that one obtains for $\widetilde{s}_{y(z)}$:

$$\widetilde{s_z} = \frac{v}{2}\left[\frac{u(1+\alpha)e^{-T_R/T_s^e} - (1+\alpha)\cos(\omega_e T_R) - \beta\sin(\omega_e T_R)}{\Delta}\right] e^{-T_R/T_s^e} \tag{2.14}$$

$$\widetilde{s_y} = \frac{v}{2}\left[\frac{\beta e^{-T_R/T_s^e} - \beta\cos(\omega_e T_R) + (1+\alpha)\sin(\omega_e T_R)}{\Delta}\right] e^{-T_R/T_s^e}, \tag{2.15}$$

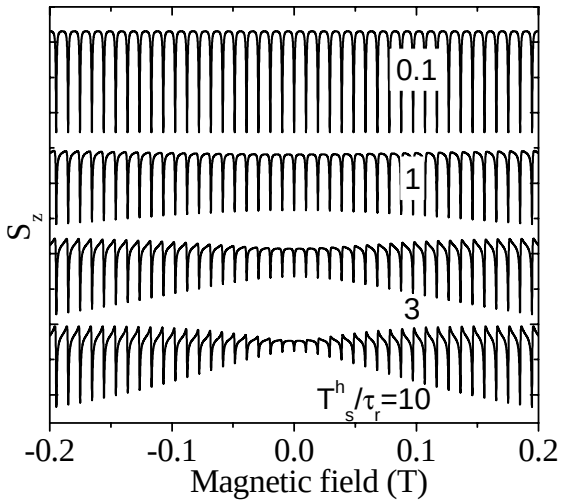

Figure 2.7: Calculated RSA spectra of 8-nm-thick $In_{0.09}Ga_{0.91}As$ quantum well (sample #11307) for a homogeneous spin ensemble excited at trion resonance, based on Eqs. (3-6). $\delta = 10$ ps, $|g_e| = 0.555$ (determined from RSA peak distance), $\Delta g_e = 0$, $T_s^e = 55$ ns, and $\tau_r = 120$ ps for different ratios T_s^h to τ_r, given at each curve.

where

$$\begin{aligned}\Delta &= 1 + u(1 - v(1+\alpha))e^{-2T_R/T_s^e} - (1 + u - v(1+\alpha))\cos(\omega_e T_R)e^{-T_R/T_s^e} + \\ &+ \beta v \sin(\omega_e T_R)e^{-T_R/T_s^e} \end{aligned} \tag{2.16}$$

here $v \equiv \sin^2(\Theta/2)/2$, $u \equiv \cos(\Theta/2)$, $\alpha \equiv Re(1/(\tau_r\Omega))$, and $\beta \equiv Im(1/(\tau_r\Omega))$.

The RSA signal is proportional to the spin polarization summed over the electron ensemble, $S_z = \sum s_z$. Figure 6.2 shows S_z shortly before pulse arrival calculated with Eqs. (2.12) - (2.15) for $T_s^e = 55$ ns and different hole spin relaxation times. With increasing T_s^h the RSA shape changes strongly, both with respect to the peak amplitude and the signal shape between the peaks. The upper curve (with a short $T_s^h = 12$ ps) looks like an ordinary RSA signal [35], in contrast to our experiment. If T_s^h approaches τ_r, the peak amplitudes decrease toward zero field. Only if $T_s^h \gg \tau_r$ the RSA signal reproduces the experimental data [upper curve in Fig. 2.6 (b)]. Therefore the imprint of the hole spin is essential for understanding the RSA spectra, even though the FR signal is solely contributed by the resident electron magnetization. This memory about the hole spin dynamics arises from the hole involvement in the generation of resident electron spin polarization. For the calculations a small pulse area $\Theta = 0.056\pi$ was used. Calculations show, however, that an increase of Θ up to 0.22 π does not change the RSA signal shape.

2.2.1 Optical setup

The complete optical setup is shown in Fig. 2.8. All experiments were done using 1.5 ps laser pulses. The source of these pulses is a commercial laser system consisting of a

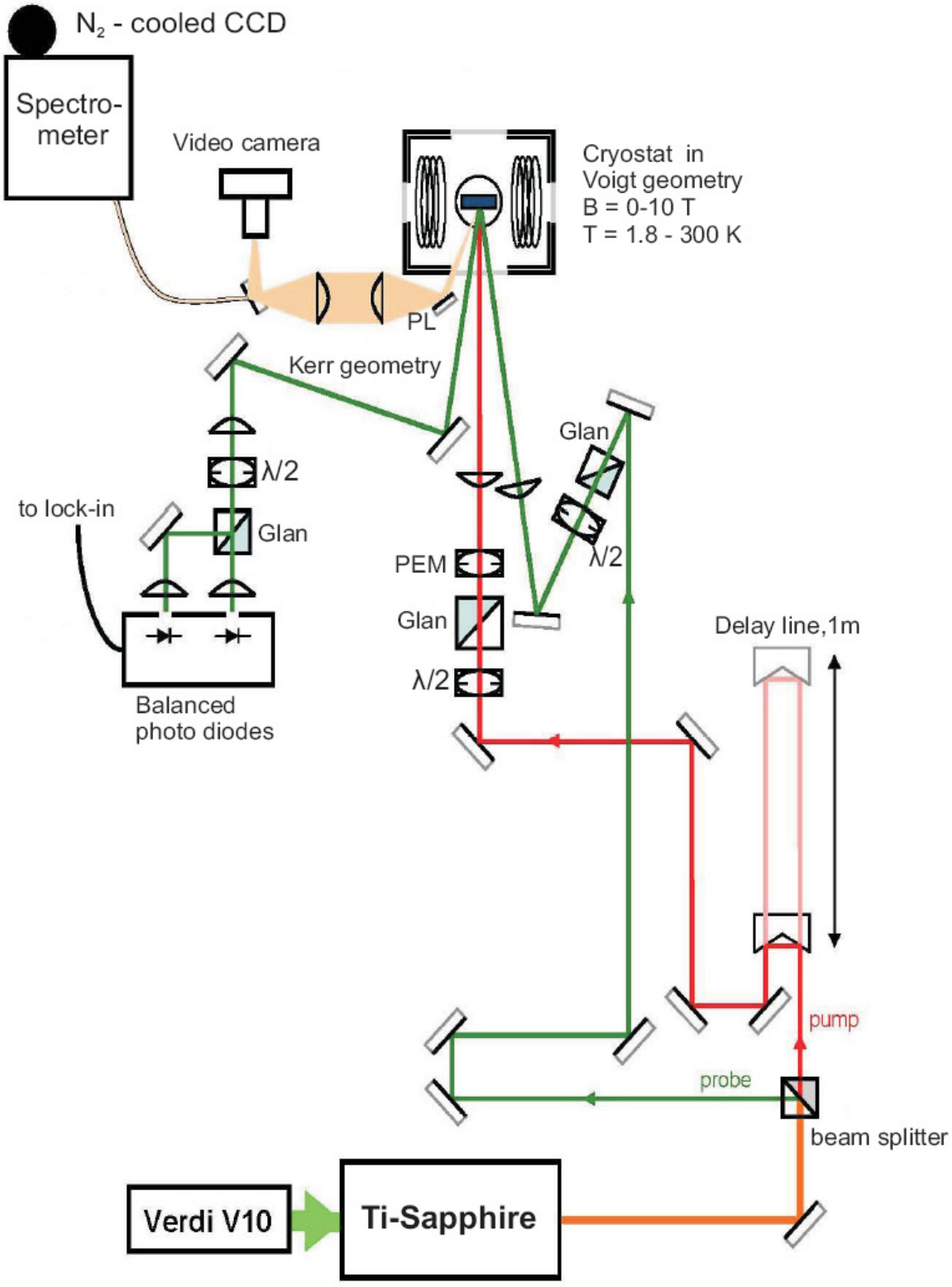

Figure 2.8: Optical setup of the TRKR experiment.

10 W Nd:YVO_4 pump laser (Coherent, Verdi V10, 532 nm) and a tunable Ti:Sapphire laser (Coherent, Mira 900-D). The advantage of the Mira is the large wavelength tuning range from 700 to 980 nm for the broadband set of intracavity mirrors. For a pumping power of 10 W the output power of the Mira is about 1.3 W at 800 nm and 1 W at 900 nm. The full width at half maximum (FWHM) of the pulses is about 2 meV with a typical pulse length of about 1.5 ps and repetition frequency of 75.6 MHz.

The laser beam is divided into the pump and probe beam by a glass plate at power ratio of about 9:1. The probe beam is then routed via a fixed compensation line to allow a time overlap of pump and probe pulse at $\Delta t = 0$ of the delay line. The probe beam is then going through a high quality calcite polarizer (Glan-Thompson prism) which prepares the linear polarization of the probe beam with an extinction ratio of 10^5. The following achromatic (600 - 1200 nm) $\lambda/2$-retarder plate (B. Halle Nachfl., RAC 5.2.10) allows to control the plane of linear polarization relative to the sample. The power of the probe pulse is controlled by a gradient gray filter (not shown in the Fig. 2.8, Edmund Optics, Filter ND Circ 0-3.0).

The pump beam is routed to a retro reflector (PLX, OW-25-2), that can be moved on a motorized translation stage (OWIS, LIMES 170, 1000 mm). This mechanical delay line controls the time delay between pump and probe pulses, simply by changing the path length the pump pulse has to travel. A full possible displacement of the delay line by L=1 m corresponds to a time delay of $2L/c = 6.6$ ns (c is the speed of light), and, with a positional accuracy of about 1 μm, a time resolution of 7 fs is easily achieved. This is much shorter than the pulse duration, so the total time resolution is limited by the ps-pulse length only. Because the laser already provides a 100:1 linear polarization, a motorized $\lambda/2$-retarder in conjunction with a high quality calcite polarizer is used after the delay line both to allow continuous intensity attenuation and to prepare the linear polarization state of the pump beam with a 10^5 extinction ratio. Then, for most experiments, a photoelastic modulator (PEM) placed at 45° to the vertical axis changes the polarization at a frequency of 50 kHz (Hinds, PEM90 with I/FS-50). For a retardation of $\lambda/4$ of the modulator, the polarization state is periodically modulated from left circular to right circular light. In between, the polarization changes from elliptical to linear. To select the proper phase position of the modulated signal, the lock-in technique is applied, which also greatly enhances the signal-to-noise ratio.

After this point, both the pump and the probe beams are focused on the sample with $f = 30$ cm quartz lenses onto the same spot on the sample, which is typically 140 μm in diameter for pump and 100 μm for probe. The spatial overlap is very crucial in order to obtain Faraday rotation of the optically aligned spins. For this purpose the pump spot is slightly defocused, so that if the pump spot position slightly changes (for example due to delay line movements) the spots are still overlapping. With the help of a video camera, which shows the position of the spots on the sample, preliminary alignment of the spot overlap can be done. Typical power densities, that were used in experiments are: for QWs $P_{pump} = 1$ W/cm^2; $P_{probe} = 0.5$ W/cm^2 (it strongly depends on the doping densities of the samples, temperature, etc.)

The sample is mounted in an optical cryostat (Oxford Instruments, SpectroMag), that allows bipolar application of a magnetic field up to 7 T using a superconductive

magnet. The variable temperature insert (VTI) of the cryostat features sample temperatures from around 2 K (with pumping on VTI) up to room temperature (300 K). The sample holder allows to rotate the sample in axial or transversal directions. The position of magnet relative to the sample can be changed by the rotation of the cryostat, so that both configurations (Faraday ($\mathbf{k} \parallel \mathbf{B}$) and Voigt ($\mathbf{k} \perp \mathbf{B}$)) are available. After passing through the sample the probe beam is traveling through an achromatic focusing lens and a $\lambda/2$-retarder followed by a polarizing beam splitter (Glan-laser prism). The beam splitter divides the incoming light into two beams with perpendicular polarizations. Each of them is then directed onto separate Si photodiodes of the auto-balanced photo detector (Laser 2000, NFI-2007). The retarder can be rotated about its optical axis, so that it allows to turn the incident polarization. This allows to balance both photodiodes, when no sample-induced polarization change is expected. Some changes of the setup are necessary in other cases. In the case of creation of linear dichroism an additional $\lambda/4$-retarder plate is placed after the PEM under an angle of 45°, which converts the modulated circular light into linear light. Another modification is used for excitation with light of only one circular polarization. Here an additional $\lambda/4$ plate is added, the PEM is switched off and the modulation of the pump beam is then provided by a mechanical chopper with a frequency range from 1 to 4 kHz. A third option is the measurement of differential transmission. Again, additional to previous case, only the registration of the probe is changed. Probe beam going through the sample hits one of the photodiodes and the other diode is hit by additional probe beam, which is routed around the cryostat. Figure 2.8 is also shows, that it was possible to measure the photoluminescence (PL) of the sample. For this purpose we have used an additional low-power (about 2 W/cm^2) He-Ne laser to excite the sample and an optical fiber to lead the PL light into the spectrometer associated with a liquid nitrogen cooled CCD detector. One has to mention, that for measurements of the Kerr rotation the only change of the setup is the routing of the reflected probe beam to the registration scheme.

2.3 ^{3}He setup

2.3.1 General remarks on differences between Oxford ^{3}He and ^{4}He variable temperature insets

The Oxford 7 tesla cryostat has a special ^{3}He inset , which is called Heliox TL, replacing the VTI (variable temperature inset) in the other Oxford magnets (7 T and 10 T). Concerning cooling down the magnet there is no difference between ^{3}He and ^{4}He versions.

There are two additional radiation shields in the ^{3}He magnet (Fig.2.9):

- Quartz windows on the nitrogen shield (77 K)
- Quartz windows on the magnet (4.2 K)

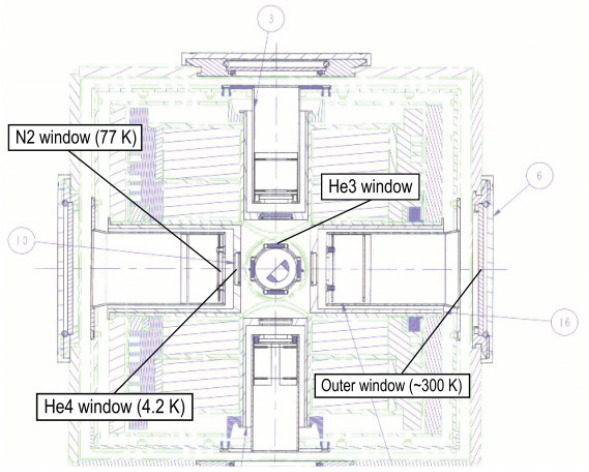

Figure 2.9: Windows ^{3}He cryostat [47]

The nitrogen windows can be heated if they get cloudy by any deposit, e.g. from the vacuum pump. The ^{3}He cryostat additionally has an controllable ^{4}He needle valve for cooling the so called "1K pot". The original VTI needle valve, which has a heater attached, is used to control the helium flow through the sorb [47].

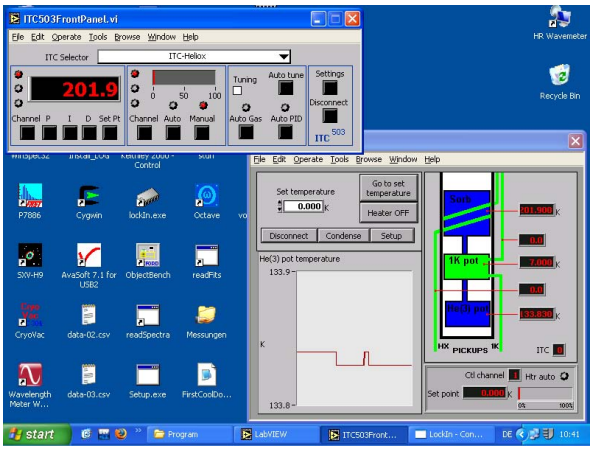

Figure 2.10: LabView control panels [47]

2.3.2 Mode of operation

The ^{3}He inset has three important parts: the ^{3}He pot, the 1K pot, and the sorb (Fig. 2.10). The last two can be cooled with ^{4}He from the magnet dewar. The ^{3}He pot contains the sample surrounded by ^{3}He. The 1K pot is used to precool and liquefy most of the ^{3}He into the ^{3}He pot while the sorb is kept at about 40 K, and thus not pumping.

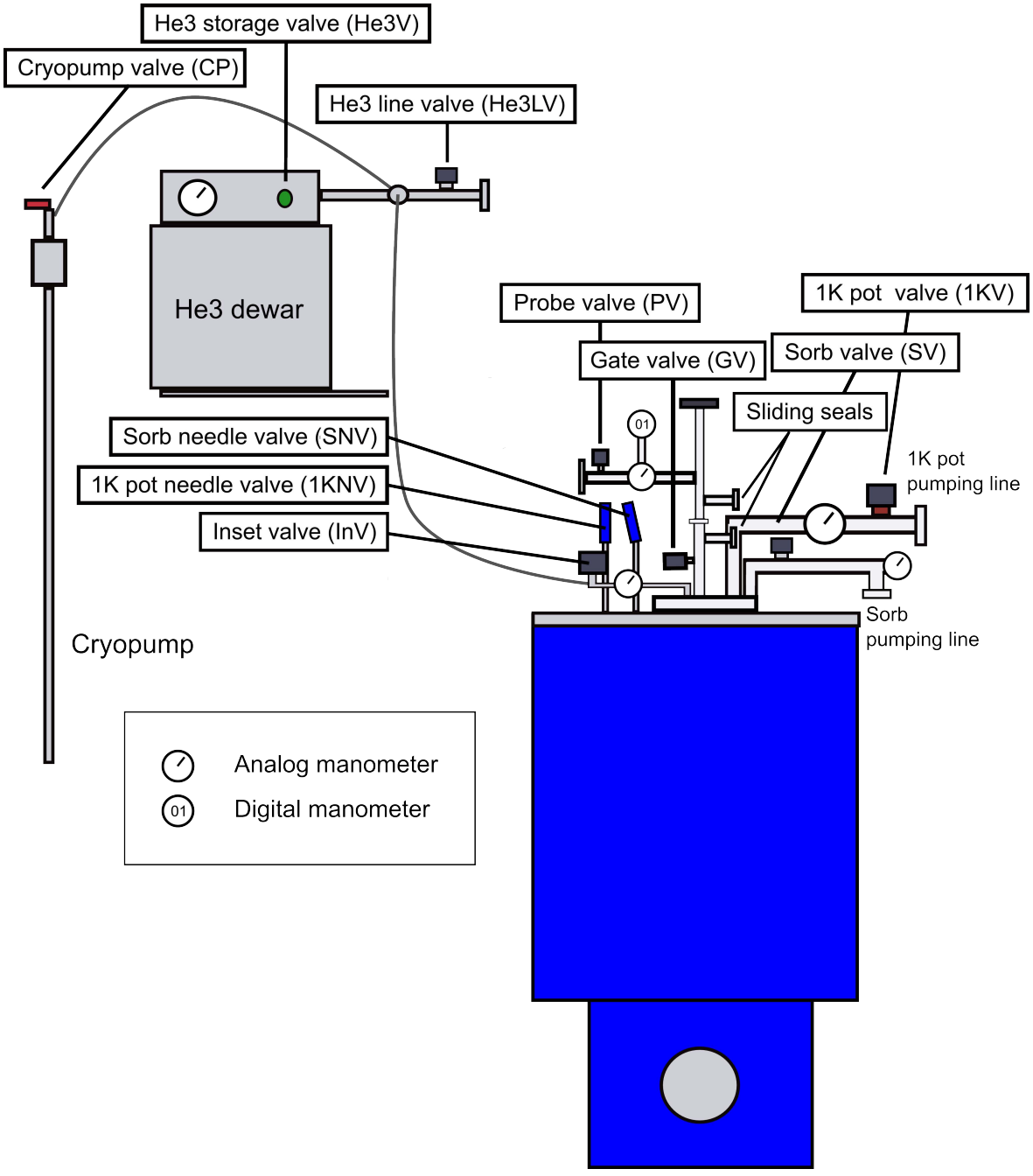

Figure 2.11: Schematics of valves of Heliox system [47]

Depending on the temperature reached in the 1K pot, a few percent of ^{3}He are not liquefied (e.g. $T_{1K} = 1.3$ K, $p_V = 30$ mbar, ≈ 96 % liquid ^{3}He). Cooling the sorb below 40 K, it starts pumping on the liquefied ^{3}He. Cooling the sorb to about 3 K the vapor pressure drops to 10^{-2} - 10^{-3} mbar, which corresponds to temperatures below 0.4 K.

2.3.3 Setup in detail

Fig. 2.11 shows the schematics of the Heliox system. The 30l ^{3}He storage is filled to a pressure of about 800 mbar ($\sim$24 l ^{3}He gas $\hat{=}$36cm^3 ^{3}He liquid, Ref. [47]). The cryopump is only used if the system is disassembled for transportation or warm up to safely store the ^{3}He in the storage vessel. There are two manometers to measure the ^{3}He pressure in the inset: An analog manometer for coarse measurement of the ^{3}He pressure and a digital manometer to measure the ^{3}He pressure down to 10^{-2} mbar with the sorb pump in operation [47].

The sliding seal pump has to be connected to evacuate a sliding seal whenever the respecting tube is moved, e.g. for adjustments of the sample.

The insulation vacuum pump is used to achieve an insulation vacuum when the ^{4}He dewar is empty. We use a turbo pump that is able to establish a pressure of about 10^{-5} mbar when the cryostat is at nitrogen temperature. With the ^{4}He dewar being filled, the pump is disconnected by closing valve IV2, and reopened whenever there is a danger of the dewar becoming empty, e.g. over the weekend.

The sorb, which consists of charcoal in the inset, is cooled by ^{4}He drawn through a needle valve (SNV, with needle valve heater) and has a heater attached. Both are regulated electronically by the Heliox-ITC on the magnet cabinet. The sorb is pumped by a mechanical pump (Edwards, 16 m^3/h). The 1K pot, which is attached to the inset, is also cooled by helium through a needle valve (1KNV, without heater) controlled by the ITC VTI. The pump connected to the 1K pot should have a pumping speed of at least 50 m^3/h in order to achieve a pressure below 30 mbar [47].

2.4 Samples characterization

Two GaAs/$Al_{0.34}Ga_{0.66}As$ structures were grown by molecular-beam epitaxy on (001) GaAs substrates for the present study. Each sample contains four QWs with nominal thicknesses of 5, 10, 14, and 17 nm sandwiched between 50 nm $Al_{0.34}Ga_{0.66}As$ barrier layers. The real QWs widths could deviate from these values within ± 10 % due to gradient of the epitaxial layer thicknesses. The structure #p340 was grown on a semi-insulating GaAs substrate. The structure #p343 was grown on a n-doped substrate. The top surface of this structure was coated by a semitransparent gold electrode. By applying an electric bias U to the electrode we tune the electron density in the 17-nm QW in the range from about 10^{10} cm^{-2} at a positive bias above 1 V to a negligibly small concentration at $U < -2$ V, for which no effects from resident electrons were observed. The growth parameters of the structures and their optical properties are collected in Appendix A.

Name	***Material***	***d[nm]***	***Substrate***	***Doping***
#p340	GaAs/$Al_{0.34}$,$Ga_{0.66}$As	17.2	001	undoped
#p343	GaAs/$Al_{0.34}$,$Ga_{0.66}$As	17.2	001	undoped
#11309	GaAs/(Al,Ga)As	10	100	n-doped
#11320	GaAs/(Al,Ga)As	10	100	n-doped
#Ash-undoped	GaAs/$Al_{0.3}$,$Ga_{0.77}$As	20	100	undoped
#Ash-doped	GaAs/$Al_{0.3}$,$Ga_{0.77}$As	25	100	n-doped
32A21M7	$Al_{0.1}Ga_{0.9}$As/AlAs	20	100	undoped
PDI-M4-2264	$In_{0.06}Ga_{0.94}$As/$Al_{0.15}Ga_{0.85}$As	20	110	undoped
	$In_{0.04}Ga_{0.96}$As/$Al_{0.15}Ga_{0.85}$As	20	110	undoped
	$In_{0.03}Ga_{0.97}$As/$Al_{0.15}Ga_{0.85}$As	20	110	undoped
	GaAs/$Al_{0.15}Ga_{0.85}$As	20	110	undoped
#11708	$In_{0.09}Ga_{0.91}$As/GaAs	8	100	n-doped

Table 2.1: List of samples

In order to study dependence of the spin dephasing time on the electron density and its optimization in the QWs, we observed additionally two n-doped GaAs/$Al_{0.3}$ $Ga_{0.77}$As quantum well heterostructures, namely middle n-doped sample #11319 and highly doped #11320. These structures were grown in Bochum University and have almost the same growth structures, that detailed description is given in Appendix A. To the same purpose we study a series of samples from Israel, namely GaAs/$Al_{0.3}Ga_{0.77}$As quantum wells. One samples is undoped GaAs/$Al_{0.3}Ga_{0.77}$As QW, which consist on 10 periods of 20 nm GaAs QW and 80 nm $Al_{0.3}$/$Ga_{0.7}$As barrier. The second sample was n-doped GaAs/$Al_{0.3}$,$Ga_{0.77}$As ($n = 2 \cdot 10^{11}$) QW of 25 nm width, which was asymmetrically doped (barrier 80 nm).

The next sample called 32A21M7 was made in France in group of J.Bloch [48]. This sample attracted our attention due the possibility of optically control of carriers, continuously go from excitons, trions toward a degenerate electron gas. The sample is a $\lambda/2$ AlAs cavity with a top (bottom) Bragg mirror of 15 (25) $Al_{0.1}Ga_{0.9}$As/AlAs pairs on a GaAs substrate (see Appendix for details). A mixed-type QW structure is placed at the antinode of the cavity mode: it contains a 20 nm wide GaAs quantum well, surrounded by two narrow GaAs quantum wells (2.6 nm). The narrow quantum wells are separated from the wide QW by AlAs barriers (10 nm). When the narrow quantum wells are photoexcited by a high-energy laser beam, the generated electrons quickly transfer toward the lower energy levels of the large QW through the X valley of the AlAs barrier (with transfer time in the ps range). On the other hand, holes can transfer to the wide QW only by tunneling through the barrier with a transfer time many orders of magnitude longer (in the ms range). An electron gas is thus formed in the large QW, the density of which is optically controlled [48].

The first part of this thesis is concentrated on the spin dynamics study in GaAs/Al_xGa_{1-x}As quantum well structures. Additionally we observed less studied type of heterostructures such as $In_{0.09}Ga_{0.91}$As quantum wells. This structure (with

the number #11708) was grown on (100)-oriented undoped GaAs substrate by the MBE method. As it is shown in Appendix, the sample is a $In_{0.09}Ga_{0.91}As$/GaAs heterostructure with the two coupled 8 nm $In_{0.09}Ga_{0.91}As$ QWs separated by a thin (1.7 nm) GaAs barrier. It contains a 100 nm n-doped GaAs:Si buffer layer separated by a 100 nm GaAs spacer from the QWs. The doped layer serves as a source of electrons for the QWs. The two-dimensional electron gas density in the QWs does not exceed $10^{10}\,cm^{-2}$.
The next sample was chosen from point of interest of studying GaAs/(Al,Ga)As quantum wells grown on (110) GaAs substrate. This sample was given us by K. Biermann from Paul-Drude-Institut fr Festkörperelektronik . It is called PDI-M4-2264 and consist of four 20-nm-thick undoped (Ga,In)As QWs with AlGaAs barriers grown by molecular-beam epitaxy on a (110) GaAs substrate. The growth parameters are given in Appendix.

In this work we concentrate on the spin dynamics studying not only on the III-V heterostructures but as well on the II-VI heterostructures. The CdTe/$Cd_{0.78}Mg_{0.22}Te$ QW heterostructure (sample 031901D) was grown by molecular-beam epitaxy on a (100)-oriented GaAs substrate followed by a 2 μm CdTe buffer layer. It has 5 periods, each of them consisting of a 110-nm-thick $Cd_{0.78}Mg_{0.22}Te$ barrier and a 20-nm-thick CdTe QW. An additional 110-nm-thick barrier was grown on top of this layer sequence to reduce the influence of surface charges on the electronic states in the QWs. The barriers contain 15 nm layers doped by Iodine donors. Undoped 20 nm spacers separate the modulation-doped layers from the QWs. Electrons from the barrier donors, being collected into QWs, provide there a 2DEG with a low density of about $n_e = 2 \times 10^{10}$ cm^{-2} Ref. [34].

Chapter 3

Spin coherence in GaAs/(Al,Ga)As quantum wells

In the following Chapter the discussion of the experimental results and a possible interpretation of the findings will be presented. We have studied experimentally high quality structures with GaAs/(Al,Ga)As QWs containing excess electrons. The effect of various experimental parameters such as applied external electric bias, magnetic field strength, and temperature on the rate of spin dephasing and electron concentration has been carefully analyzed.

3.1 Conditions for observation of spin coherence in a transverse magnetic field

The spin dynamics of carriers and the processes of optical spin orientation in semiconductors were treated in a great number of experimental and theoretical studies [50]. Here, we will consider, in brief, the main conclusions of these studies, which will be used in the analysis of our experimental data.

The angle of rotation of the polarization plane of the probe beam (signal of rotation), measured in Kerr rotation experiment is proportional to the degree of circular birefringence arisen due to orientation of the spins of carriers by the pump light. The Kerr signal is contributed by orientation both of electron and hole spins. In a transverse magnetic field, the optically oriented spins precess around the magnetic field direction. As a result, their projection on the direction of observation (in our case it coincides with the structure growth axis) and hence the signal amplitude oscillate in time with a frequency proportional to the field strength. From the quantum-mechanical point of view, these oscillations represent quantum beats (QBs) of Zeeman sublevels split by the magnetic field. I would not go into details of the pump-probe technique here, because the basics of this technique are described in the Chapter 2.

Electron-hole exchange coupling makes the exciton spin insensitive to weak magnetic fields for which the Zeeman splitting is smaller than the energy of the exchange

interaction. However, in sufficiently strong magnetic fields such that the exchange coupling is broken, the spin precession of electron and hole in the exciton can be considered independently. A specific feature of the spin states of carriers in low-dimensional structures is a pronounced anisotropy of the heavy-hole g-factor [49]. Namely, in most structures with QWs, the transverse component of the hole g-factor is negligibly small (see, e.g., [51]). As a result, the hole spin precession period in a transverse magnetic field appears to be much longer than the longitudinal relaxation time $T_{1,h}$, and, as a rule, the precession cannot be realized.

The dynamics of the Kerr signal related to the spin oriented electrons reflects the spin precession in transverse magnetic field and the spin dephasing. The precession is revealed in the form of harmonic oscillation of the signal at the frequency corresponding to splitting of spin sublevels (Zeeman splitting). The decay of the oscillations (with time T_e) is controlled by several factors. A more detailed description of these factors and discussion of spin decoherene are given in Section 1.5. When no excess electrons are present in the QW, the decay results not only from the electron-spin dephasing time characterized by $T^*_{2,e}$, but also from the exciton recombination characterized by τ_X: $1/T_e = 1/T_{2,e} + 1/\tau_X$.

In the presence of excess electrons, absorption of a photon may give rise to formation of a trion [52] - a triple-charged particle comprised of a hole and two electrons (photogenerated and excess). At zero magnetic field, orientation of the hole spin is controlled by polarization of the photon, while the spins of the photogenerated and excess electrons (according to the Pauli principle) should be antiparallel to each other. Note, that here are considered only the singlet trions because the triplet trions are unstable under usual conditions. This means that the trion formation extracts electron spins parallel to the hole spins from the excess electron ensemble. As a consequence, an excess spin antiparallel to that of the hole is generated in the electron ensemble. The amplitude of the Kerr signal associated with this spin depends on the ratio of the relaxation rate of the hole spin,$1/T_{1,h}$, to the rate of trion recombination, $1/\tau_T$. In the case of fast relaxation of the hole spin ($1/T_{1,h} \gg 1/\tau_T$), the hole may recombine with equal probability with each of the two electrons in the trion. This recombination does not change the average electron spin in the ensemble, and therefore cannot affect the Kerr amplitude. If the hole spin relaxes slowly ($1/T_{1,h} \ll 1/\tau_T$), then, in conformity with the selection rules on angular momentum, the electron spin taken from ensemble is returned with the same orientation, which decreases or even fully compensates the light-induced spin orientation.

In the presence of the transverse magnetic field, precession of the excess electron spin changes its orientation with respect to the hole spin and total compensation does not occur even if the hole spin does not relax [53]. In this case, the condition of conservation of the optical orientation after the trion recombination can be represented in the form: $\omega_e \gg 1/\tau_T$, where $\omega_e = g_e\mu_B B/\hbar$ is the electron Larmor frequency (μ_B is the Bohr magneton, B is the field strength, $\hbar$ is the Planck constant).

Thus the dynamics of the detected signal should contain, three components, namely, a nonoscillating signal related to the hole spin orientation and oscillations related to precession of the electron spin in the exciton and of the spin induced in the excess

electron ensemble. Generally, the decay of the oscillations should therefore be non-exponential and comprise two components associated with the exciton recombination and the dephasing of the excess electron spins. The signal resulting from resonant excitation of the trions should contain only the last component[54].

3.2 The time-resolved Kerr rotation signal with and without magnetic fields

The studies of the spin dynamics are performed here with experimental results on the undoped sample #p340 with a low concentration of excess electrons caused by nonintentional (residual) doping of the structure. Figure 3.1(a) shows the photoluminescence (PL) spectrum of this sample in the vicinity of the excitonic peaks of two widest QWs. Thickness of the QWs in the studied samples were slightly different from their nominal values due to lateral gradient of the growth rate. It is seen that each peak in the PL spectrum has a pronounced doublet structure with the short-wavelength exciton (X) and long-wavelength trion (T) components. Lower curve in Fig. 3.1(b) shows the excitonic PL kinetics for the 17-nm QW under near resonant excitation. Upper curves

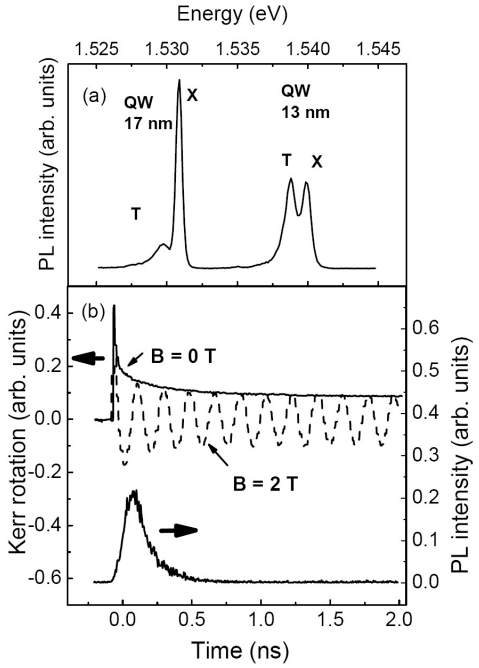

Figure 3.1: (**a**) A fragment of the PL spectrum for 13- and 17-nm-thick QWs of the sample #p340 GaAs/$Al_{0.34}Ga_{0.66}As$ in the region of both excitonic peaks. (**b**) Upper plot: dashed line - dynamics of the QB signal for the 17-nm-thick QW in the transverse magnetic field $B = 2$ T. Solid line - the same with no field. Lower plot - kinetics of the excitonic PL.

in Fig. 3.1(b) show the kinetics of the Kerr rotation signal detected at the exciton peak of a 17-nm QW with no magnetic field and in the transverse magnetic field $B = 2$ T.

The signals are seen to have a non-elementary shape. Each of them contains a rapidly decaying initial part transforming into slowly decaying tail in the absence of the field and into weakly damping oscillations in the transverse magnetic field. In accordance with the conclusions of the previous section, the rapidly decaying signal should be ascribed to the hole spin orientation. The decay time of this signal equals approximately 10 ps, which agrees with the published data about the hole spin relaxation time in similar systems [55, 56].

Rapid relaxation of the hole spin breaks the exchange coupling between the electron and the hole in the exciton, which makes possible free precession of the electron spin. The result of this precession is the oscillating signal shown in Fig. 3.1(b). The frequency of the observed oscillations well agrees with the value obtained from Zeeman splitting of spin sublevels of the electron, $\omega_e = g_{xy}\mu_B B/\hbar$, calculated for this QW with the use of the transverse component of the electron g-factor g_{xy} known from the literature [57]. The oscillating part of the curves can be sufficiently well fitted by the damped harmonic function of the form

$$y(t) = (a_1 \exp[-t/\tau_1] + a_2 \exp[-t/\tau_2]) \cos \omega_e t, \tag{3.1}$$

where τ_1 is the decay time of the fast component, and a_1 and a_2 are the amplitudes of the fast and long-lived components. The decay time of the fast component, $\tau_1 \sim$ 100 - 150 ps, is close to that of the exciton PL shown in Fig. 3.1. This fact allows us to conclude that the fast components of the oscillating signal is associated with the electron constituent of the exciton spin, vanishing after the exciton recombination.

The source of the oscillating signal at long time, τ_2, substantially exceeding the exciton lifetime may be related only with the excess electrons oriented by light, whose presence in the intentionally undoped structure #p340 is likely to be caused by non-intentional background doping. The presence of excess electrons is indicated by the doublet structure of luminescence spectrum shown in Fig. 3.1(a). The splitting of trion and exciton PL lines equals 1.2 meV, which substantially exceeds the energy difference for monolayer fluctuations in wells of this width and coincides with the binding energy of a singlet trion [58]. The relative intensity of the trion and exciton peaks in the PL spectrum corresponds corresponds to a density of two-dimensional electrons of about 10^{10} cm^{-2} [59]. The conclusion that the long component of the signal is associated with trion excitations agrees well with the results of studies of the spectral dependences of the amplitudes of the fast and slow components in the QBs signal. In experiment, the amplitude and the shape of the signal were measured as a function of the photon energy. The energy was varied by tuning the Ti:sapphire laser, i.e., the photon energies of the pump and probe beams were scanned synchronously (spectrally degenerate pump-probe regime). The spectral dependencies of the amplitudes obtained from the experimental data are shown by the symbols in Fig. 3.2. The spectrum of the fast component coincides fairly well with the exciton peak of the PL spectrum. The slowcomponent spectrum is shifted towards lower energies, i.e., towards the trion peak position as compared to fast component. The shift is significantly smaller than the exciton-trion splitting, which can be explained by the relatively small contribution of the trion absorption to the excitation of the trionic states. This conclusion

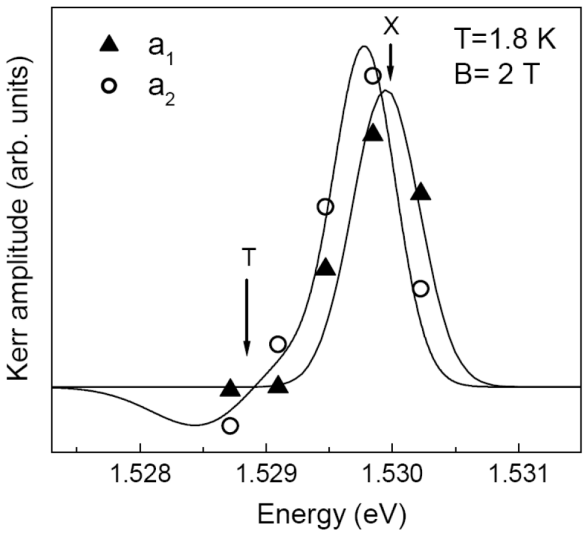

Figure 3.2: Spectral dependence of amplitudes of fast (triangles) and slow (circles) components in Kerr signal of a 17.2 nm GaAs/$Al_{0.34}Ga_{0.66}As$ QW of the sample #p340. Arrows marked by "X" and "T" show energy positions of the exciton and trion lines, respectively [54]

is supported by several experimental data related to the trion photoluminescence in semiconductor quantum wells (see, for example Ref. [60]). In accordance with these data, the ratio of the trion-to-exciton peak intensities in photoluminescence spectra substantially exceeds a similar ratio in absorption spectra. This means that the trion is predominantly formed after exciton absorption. At the same time, the Kerr rotation effect should have a maximum at the trion resonance. In our case of degenerate pump probe, the maximum of the signal should occur somewhere between the maxima of absorption and of Kerr rotation. This maximum occurs between the exciton and trion peaks. The experimental data presented here allow us to conclude that the long-lived oscillating signal is due to coherent precession of the excess electron spins. The spin coherence is generated through trions, which are predominantly formed via trapping of excess electrons by the photogenerated excitons.

In Section 3.3, we will consider the results of the experiments aimed at studying the factors affecting the decay of spin oscillations and, thus, restricting, the lifetime of spin coherence for free electrons. The measurements were performed on the sample #p340 grown on an undoped substrate.

Electron spin beats in the TRKR have been measured in magnetic fields up to 4 Tesla applied perpendicular to the structure growth axis (the Voigt geometry) (see Figure 3.3). These measurements have been done at temperature $T = 10$ K. In Figure 3.3 one can clearly see, that the decay of spin beats is enhanced for increasing fields. The amplitudes of the beats are distinguishable from each other with increase of the magnetic field. The frequencies increase with magnetic field. Here one can observe the signal at negative part, which is getting weak with increasing magnetic field. There are two primary effects of increasing the magnetic field: the spin precession frequency

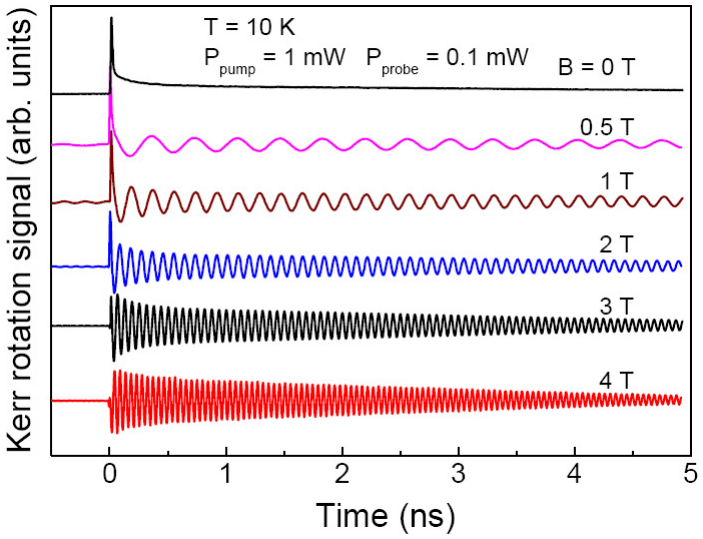

Figure 3.3: Time-resolved Kerr rotation signal measured for a 17.2 nm GaAs/$Al_{0.34}Ga_{0.66}As$ QW of the sample #p340 in magnetic field up to 4 T at temperature $T = 10$ K, $E_{exc} = 1.525$ eV and $P_{pump} = 1$ mW, $P_{probe} = 0.1$ mW.

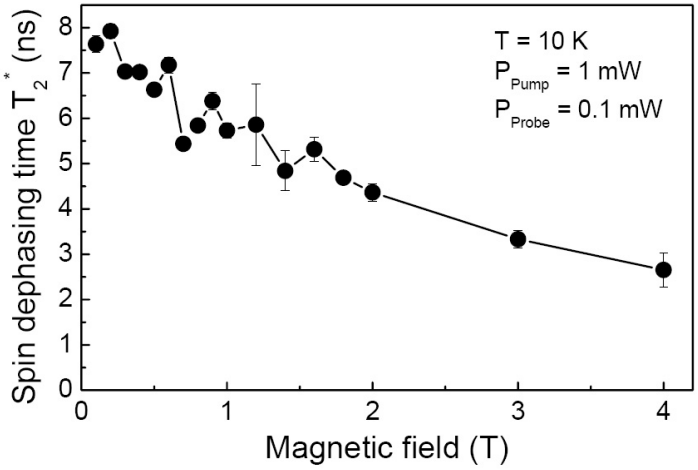

Figure 3.4: Spin dephasing time T_2^* of electrons as a function of magnetic field for 17.2 nm GaAs/$Al_{0.34}Ga_{0.66}As$ QW of the sample #p340 at temperature $T = 10$ K.

increase, and the spin coherence decays more rapidly. The former can be understood from the linear dependence of the Larmor frequency on the applied magnetic field, while the latter indicates a change in the spin dephasing time. The oscillation frequency increases with magnetic field as expected from the spin-splitting of electron states according to Eq. (1.13). The resulting B-field dependence of the electron precession frequency is shown in the Fig. 3.5 (a). The values of the g factors found from the field dependence of the frequency obtains $|g_e| = 0.383 \pm 0.001$. Figure 3.4 shows spin dephasing time T_2^* of electron as a function of magnetic field. As one can see, the spin dephasing time reduces with increasing magnetic field. We observe the longest time at temperature $T = 10$ K in the zero field limit width of about 8 ns. The decrease of T_2^*

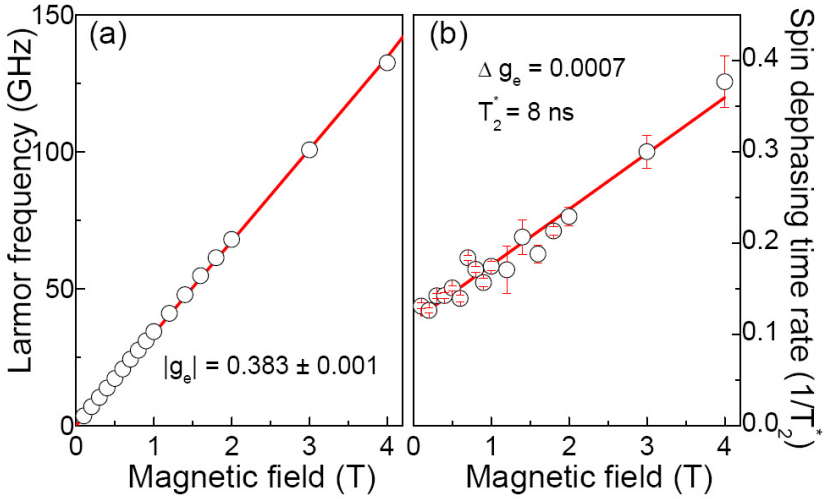

Figure 3.5: (**a**) Field dependence of the QB frequency (circles) at temperature $T = 10$ K. Solid line is a fit by a linear dependence $\omega_e = |g_e|\mu_B B/\hbar$ with $|g_e|$=0.383±0.001. (**b**) Dependence of the spin dephasing rate on the magnetic field for a 17.2-nm-thick GaAs/$Al_{0.34}Ga_{0.66}$As QW of the sample #p340 at temperature $T = 10$ K. Solid line is an interpolation, which allows us to evaluate Δg_e.

with the growing magnetic field can not be described by the dependence $T_2 \sim 1/B$, what allows us to suggest, that in this sample the spread Δg_e of the electron g factors is not the main mechanism controlling the inhomogeneous dephasing. The dependence of the spin dephasing rate on the magnetic field is shown in Figure 3.5 (b). The fitting of this curve gave the result spread of the g-factor $\Delta g_e = 0.0007$, which is only 0.18% of the value of g_e factor.

3.3 Temperature dependence of TRKR signal

In Section 3.2 was schown the magnetic field dependence of the Kerr rotation signal, where the signal has a considerable amplitude even at negative delays. This means that the spin dephasing time becomes equal or longer than the laser pulse repetition interval ($T_R \approx 13$ ns). In this case one has to use the other technique, called resonant spin amplification (RSA) technique. The main idea of this method is described in Chapter 2. The result of the measurement on the #p340 sample with a help of the RSA technique is presented in Fig. 3.6 (a). The magnetic field was scanned from -30 mT to +30 mT at negative time delay of the probe pulse ($\Delta t = -80$ ps). Here are observed a series of sharp peaks as a fuction of the magnetic field. These peaks correspond to the commensurable of the spin precession period. The spin dephasing time T_2^* can be directly evaluated from the fit of the RSA peaks to equation (2.9). The fit is presented in the Figure 3.6 (b). The long spin dephasing time $T_2^* = 25$ ns has been evaluated. It is important to note that this time is longer than the electron spin coherence time of 10 ns reported so far for GaAs QWs [61]. The figure 3.7 shows a part of the RSA signal scanned in the range from -50 mT to 50 mT at temperatures

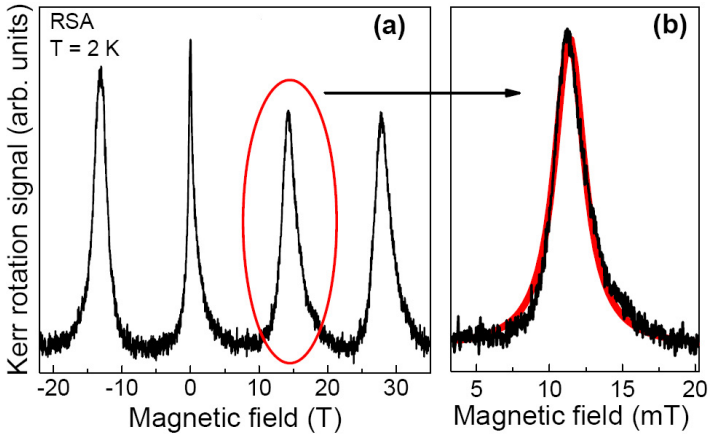

Figure 3.6: (**a**) Resonant spin amplification signal for a 17.2 nm GaAs/$Al_{0.34}Ga_{0.66}As$ QW of the sample #p340 measured from -0.075 T to +0.04 T at temperature $T = 2$ K. (**b**) Part of the fit to the RSA data (red line). The spin dephasing time $T_2^* = 25$ ns at $T = 2$ K.

from 2 K to 10 K. A temperature increase causes broadening of the peaks, which reflects shortening of the spin dephasing time. Obviously, this effect is related to the heating of the 2DEG and delocalization of electrons bound to quantum well width fluctuations. Free electrons have more channels for spin relaxation and their spin

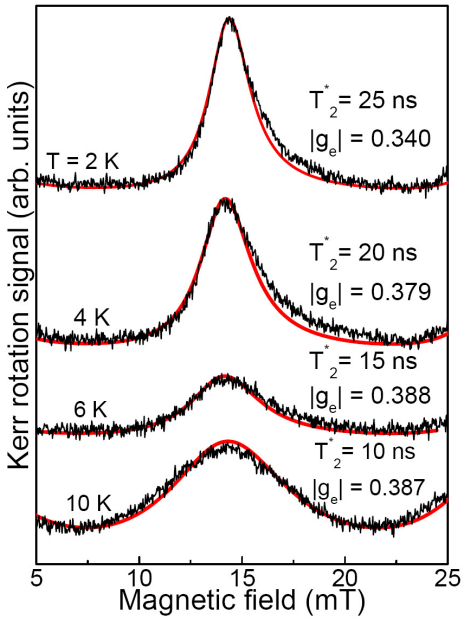

Figure 3.7: Temperature dependence of the RSA signal for a 17.2 nm GaAs/$Al_{0.34}Ga_{0.66}As$ QW of the sample #p340, scanned from 5 mT to 25 mT (black). Black curves are experimental data and thick red curves are fits by Eq. (2.9). Calculated parameters are given in the figure.

coherence decays faster. If one knows parameter T_R - the laser repetition rate, then

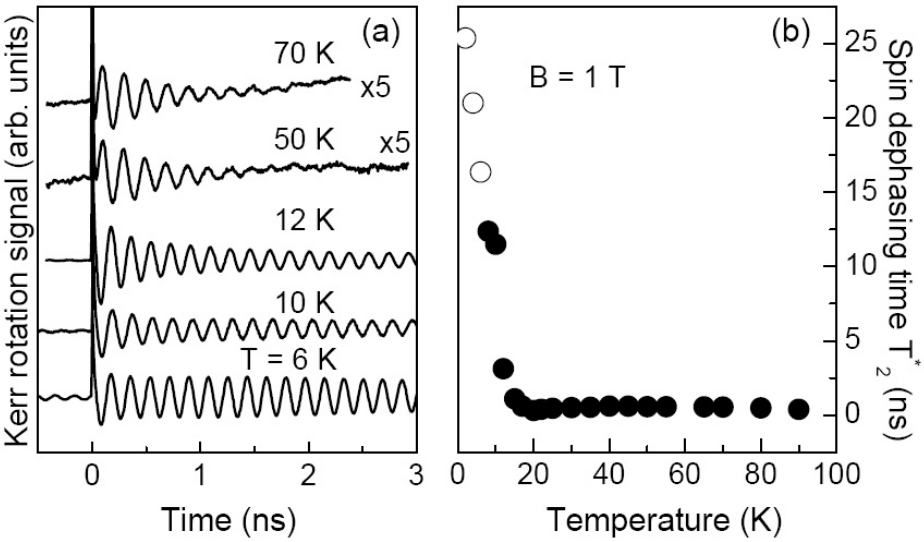

Figure 3.8: (**a**) Dependence of the time-resolved Kerr rotation signal on the temperature for 17.2 nm GaAs/$Al_{0.34}Ga_{0.66}As$ QW of the sample #p340 at magnetic field $B = 1$ T. The range of the temperatures varies from 2 K to 90 K. (**b**)The spin dephasing time T_2^* as the function of the temperature. The data (black circles) evaluated from the fit of Kerr rotation signal presented in (a). The data marked by open circles are extracted from RSA signal.

the spacing between the resonant peaks allows to extract the electronic g-factor, while the widths of the peaks are related to T_2^*. The g_e-factors values are presented in the same figure. Figure 3.8(a) shows measurements of TRKR for GaAs QW at $B = 1\,\mathrm{T}$ in the range of temperatures from $T = 2$ to $90\,\mathrm{K}$. Significant changes of the signal is observed, as first the decay of the signal is getting weaker with the high temperature and the frequencies are getting smaller. Here we see the amplitude modification. The temperature increase has a strong influence on the spin dephasing time T_2^*.

In order to make a deeper insight into main dephasing mechanisms in this structure, a temperature dependence of T_2^* was measured in the 1 Tesla magnetic field. The figures 3.8(b) shows the spin dephasing time T_2^* electrons as a function of the temperature for 17.2 nm GaAs QW. The results were taken for the interval of temperatures $2 < T < 90K$. The times longer than 6 ns are received from the first peak of the RSA signals. The longest electron coherence time $T_2^* = 25$ ns was observed at a temperature of 2 K. Figure 3.8 (b) shows obvious decrease of the spin dephasing time with rising temperature. It is known, that the spin relaxation time of localized and free electrons may be different [62]. With increasing temperature localized electrons become delocalized, and as a consequence their spin dephasing time dicreases. Such behaviour is observed in our case.

As next we describe the results of the Kerr rotation measurements with a help of ^{3}He system for the sample #p340 at millikelvin temperatures. The detailes of the ^{3}He setup are given in Chapter 2. In figure 3.9 is displayed the RSA spectrum, that was scanned from -0.3 to +0.3 T at temperature 1.2 K. This RSA signal was obtained

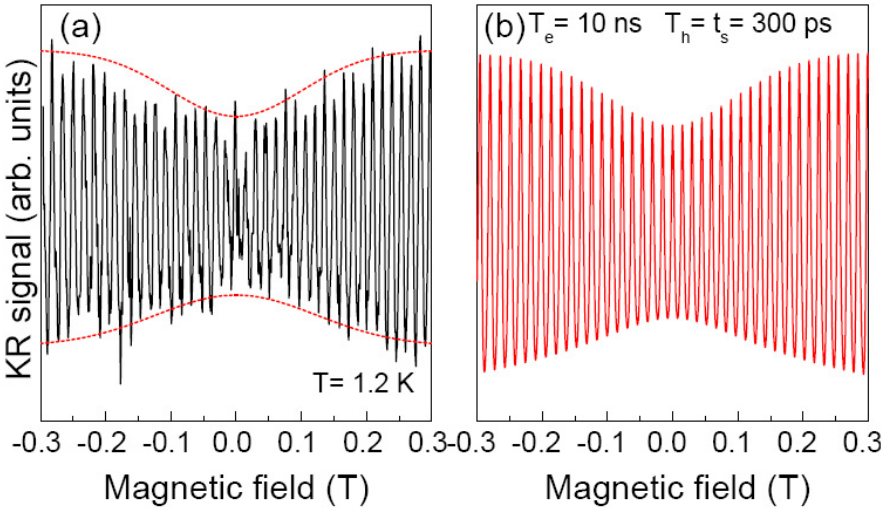

Figure 3.9: (**a**) Resonant spin amplification signal measured for 17.2 nm GaAs/$Al_{0.34}Ga_{0.66}$As QW of the sample #p340 at temperature $T = 1.2$ K. (**b**) The red curves is the fit of experimental RSA signal shown in panel (a) by Eq. (2.14).

for resonant trion excitation. The signal is quite different compare to the previous shown RSA signals, where we excited resonantly to exciton. It has bat shape and the amplitude of the peaks increases with icreasing magnetic field. This increase of the RSA peak amplitudes in weak fields is overpowered at stronger fields by the inhomogeneity of precession frequencies.

At zero magnetic field, the spin polarization of the resident electrons is preserved after trion recombination only in case of fast hole spin relaxation in the trion [41, 54]: If the hole spin relaxation time, T_s^h, is long compared to the trion recombination time, τ_r, the resident electron reappears after trion recombination with the same spin orientation as before trion formation. Therefore the induced spin polarization of the resident electrons disappears. Vice versa, if the hole spin relaxation is fast such that $T_s^h << \tau_r$, the hole in the trion on average can recombine with electrons of both orientations. Consequently, electrons polarized by light can accumulate. In a transverse magnetic field the spins of the resident electrons which are not bound to trions precess about the field, resulting in a rotation of the electron polarization during the trion lifetime. Therefore the induced polarization is not fully annihilated after trion recombination, even when the hole spin has not relaxed. Faster electron spin precession in stronger magnetic fields leads to an increase of the spin polarization. This is reflected in Fig. 3.9 by the increasing RSA amplitudes with increasing magnetic field at $T = 1.2$ K. This RSA signal was fitted by Eq. (2.14). The resulting spin lifetime of the electron equal to 10 ns. In Figure 3.10 (a) RSA scans measured at different low tempertures in the range from 0.89 K to 1.3 K are presented. The RSA signal posses here bat form. The fit of the data is shown as red curve. After fit these RSA signals by Eq. (2.14), we extract the corresponding values of the spin dephasing times T_2^*. Figure 3.10 (b) shows a low temperature dependence of the spin dephasing time. We do not observe here any changes in T_2^* with increase of the temperature.

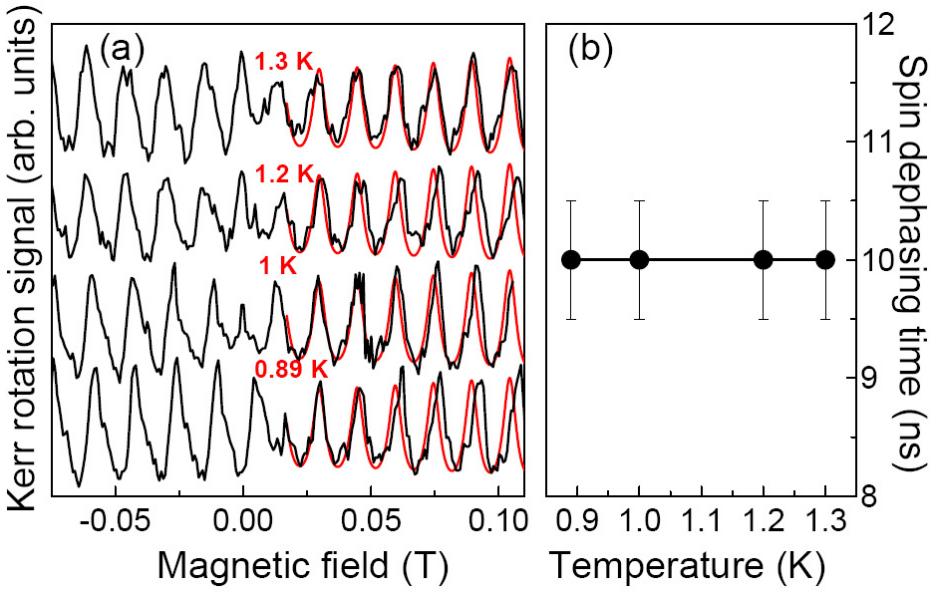

Figure 3.10: (**a**) RSA signal measured for a 17.2 nm GaAs/$Al_{0.34}Ga_{0.66}As$ QW of the sample #p340 at the trion resonance for various temperatures. Black curves are experimental data and thick red curves are fits by Eq. (2.14). (**b**) The spin dephasing times evaluated from the fit as a fuction of the temperature

3.4 Effect of beas on dephasing of electron spin beats

In this Section, we turn our attention to sample #p343, for which the density of resident electrons can be tuned by bias voltage. The detailed parameters of the structure are given in the Chapter 2. The dependence of the QB signal for the 17-nm QW on the magnetic field strength is shown in Fig. 3.11(a). The signal has been detected at the trion optical transition and therefore consists of the long-lived component only. Increase of the magnetic field strength is accompanied by a linear increase of the oscillation frequency [see Fig. 3.11(b)]. The value of the g-factor found from this dependence, g_e=0.34±0.01, agrees well with the published data [57] for the transverse component of the electron g-factor in GaAs QWs of this width. The decay time of the QBs determined from the fit of the oscillations by a harmonic function with a Gaussian envelope, $y \sim \exp(-(t/\tau)^2)\cos\omega_e t$, practically does not depend on the magnetic field strength up to $B = 4$ T [see Fig. 3.11(c)]. The electron concentration in the 17-nm QW of sample #p343 was varied by applying an electric bias to the top electrode of the sample. The QBs detected in a transverse magnetic field of 1 T at different biases are shown in Fig. 3.12. The appearance of the QB decay is seen to strongly depend on the bias. This dependence may be divided into three regions (see inset in Fig. 3.12). At negative bias below −2 V, the decay time is about 1.5 ns. As the negative bias increases to −1.5 V, the decay time increases to 4.5 ns and remains practically constant in the range from -1.5 to +0.5 V. For positive biases greater than 1 V the decay time increases to 10 ns. In the interpretation of the data, one has to keep in mind that the

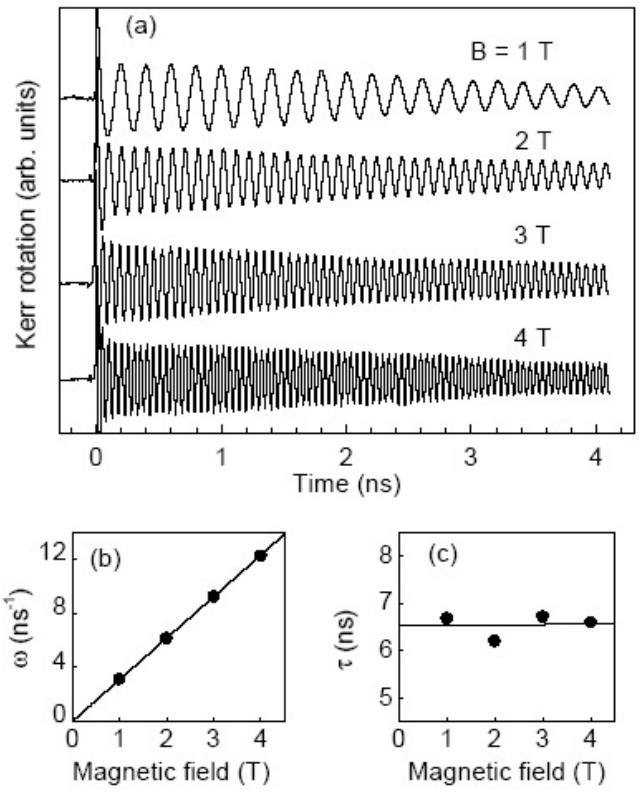

Figure 3.11: (**a**) Kerr rotation signals measured for the 17.2 nm GaAs/$Al_{0.34}Ga_{0.66}As$ QW of sample the #p343 at $U = 0.7$ V for different magnetic fields. (**b**) Field dependence of the QB frequency (circles). Solid line is a fit by a linear dependence $\omega_e = |g_e|\mu_B B/\hbar$ with $|g_e| = 0.34$. (**c**) Field dependence of the QB decay time (circles)[54]

golden electrode on the sample surface forms a Schottky barrier of 0.7 V height. As a result, the energy structure of the conduction band is substantially tilted, as shown schematically in Fig. 3.13(b). Due to that, the bottom of the conduction band in the QW is located above the Fermi energy of the doped substrate without external bias, and the electrons are not able to penetrate the substrate and reach the QW. Under this condition, the main source of the excess electrons in the QW is most likely provided by residual background doping. It is exactly these electrons that are responsible for the oscillating signal in the bias range from -1.5 to +0.5 V. For large values of negative bias, the tilt of the bottom of the conduction band becomes so steep that tunnelling of electrons from the QW to the substrate becomes possible [see Fig. 3.13(a)]. This process strongly reduces the electron concentration in the QW. As seen from Fig. 3.12, this decrease of carrier concentration results in the strong shortening of the spin oscillation decay time at $U = -2.5$ V.

A positive bias voltage compensates for the Schottky barrier effect and reduces the tilting of the conduction band. For voltages exceeding +1 V, the Schottky barrier is completely compensated [see Fig. 3.13], and an electronic current from the doped

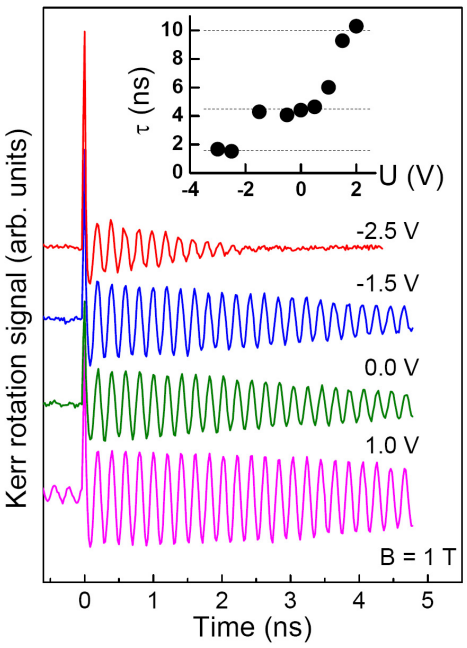

Figure 3.12: Dependence of the QB signals in the 17.2 nm GaAs/$Al_{0.34}Ga_{0.66}As$ QW of sample #p343 on bias. $T = 1.8$ K. Inset: Bias dependence of the QB decay time.

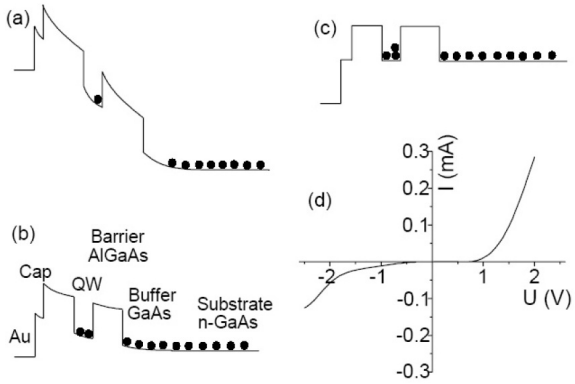

Figure 3.13: Schematic diagram of the conduction band in sample #p343 for the following electric biases applied to the top electrode: (**a**) $U = -2$ V, (**b**) $U = 0$ V, and (**c**) $U = +1$ V. (**d**) I-V characteristics of sample #p343 [54]

substrate to the QW appears as seen from the I-V curve shown in Fig. 3.13(d). As a result, the electron concentration in the QW increases. This increase is accompanied by a noticeable increase in the oscillation decay time in Fig. 3.12, i.e., by a slowdown of the electron spin dephasing rate. Based on the experimental data from Fig. 3.12and Fig. 3.13, we conclude that the coherence lifetime of the electron spin in the 17.2 nm thick GaAs/$Al_{0.34}Ga_{0.66}As$ QW of sample the #p343 increases monotonically with electron concentration.

3.5 Spin relaxation times in doped QWs

In order to study in more details the spin dynamics in the quantum wells heterostructures, it have been done measurements not only for undoped GaAs/(Al,Ga)As QW structures, but for quantum wells with different electron concentration. In this chap-

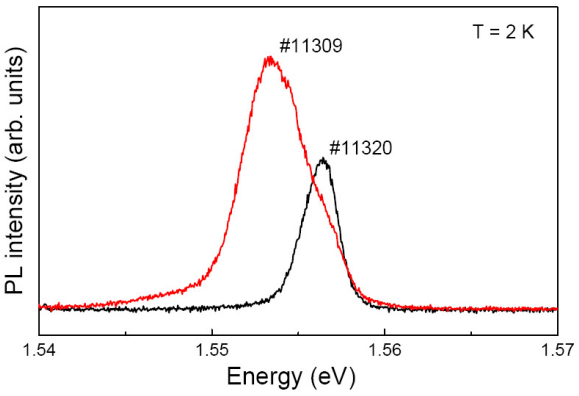

Figure 3.14: Photoluminescence of a low n-doped #11309 and highly doped #11320 GaAs/$Al_xGa_{1-x}As$ quantum wells heterostructures.

ter the results are presented for the two n-doped GaAs/(Al,Ga)As quantum well heterostructures structures, namely low n-doped sample #11309 and highly doped #11320. These structures were grown in Bochum University. Additionaly here are given results for two samples from Israel, namely GaAs/(Al,Ga)As quantum wells. The samples are called #Ash-undoped and #Ash-doped. The detailed growth of the strcutures and all characteristics are described in the Chapter 2. We start here with

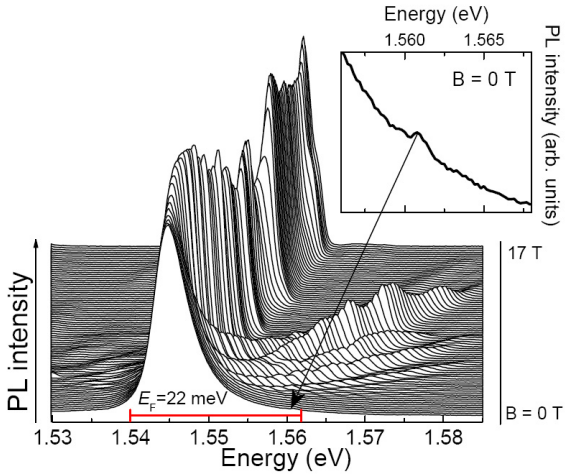

Figure 3.15: Photoluminescence of n-doped GaAs/$Al_xGa_{1-x}As$ QW (#11309)in the magnetic field region between 0 and 17 T in σ^+-polarization. The Fermi energy has been estimated to be 22 meV. $T = 2.2$ K, $E_{exc} = 1.96$ mV, $P_{exc} = 3.5$ mW/cm^2.

some experimental results measured for n-doped samples #11309 and #11320. In

Fig. 3.14 you can see the photoluminescence of these samples. In both PL spectra the only one peak is observed, it corresponds a signal from quantum well.

Our setup allows us to measure the photoluminescence in different magnetic fields. A series of PL spectra have been taken for magnetic fields between 0 T and 17 T for both circular polarizations. Results for the sample #11309 in case of the σ^+ polarization are plotted in Fig. 3.15. The samples consists of a single, wide AlGaAs QW embedded into a AlAs barrier. It is n-type doped by Silicon. To calculate the carrier density the following equation was used:

$$n_e = \frac{E_F[meV] \cdot m_e^*}{2.3 \cdot 10^{-12}} \tag{3.2}$$

The Fermi energy can be estimated from the highest recombination peak found at an energy of 1.5446 eV at as shown in Fig. 3.15. A small step in the PL signal can be observed slightly above 1.56 eV. States at higher energies are empty and do not contribute to the photoluminescence. The width of the lowest recombination peak from the onset at 1.54 eV to the small step is in good approximation 22 meV [71]. This value can be used as Fermi energy. With the well known effective mass of GaAs ($m^* = 0.067m_0$) an electron density of about $n_e = 6.4 \cdot 10^{11}$ cm^2 can be derived. This series of PL spectra has been taken at $T = 2.2$ K. Up to five Landau levels can be identified from this graph. A strong variation of the line intensity can be observed for both the main peak and its Landau level multiples. Also a nonmonotonic shift of the peaks with increasing magnetic field can be seen. Both effects are related to changes of the filling factor.

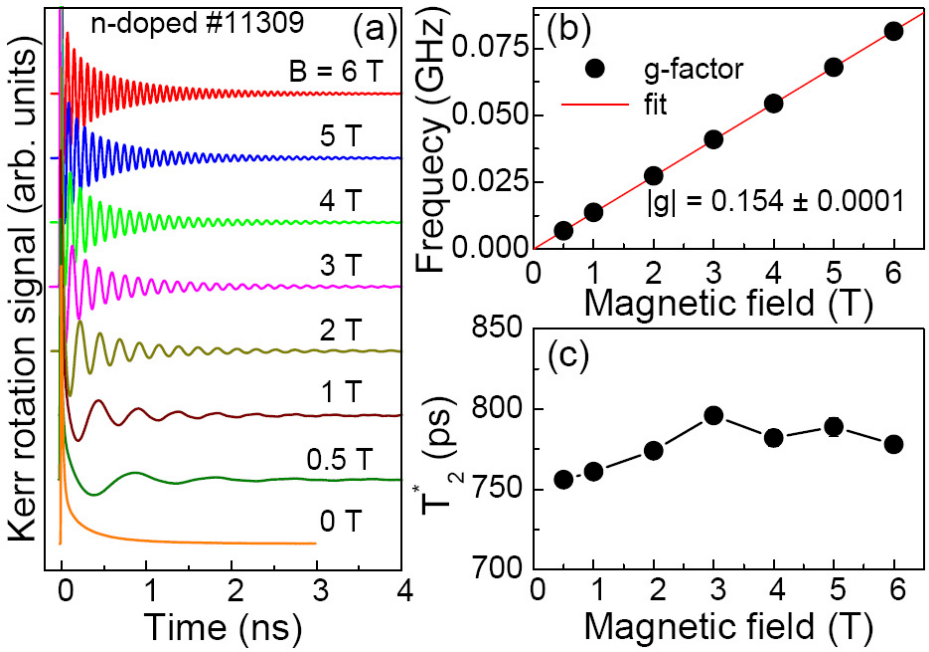

Figure 3.16: (**a**) Time resolved Kerr rotation signal for GaAs/(Al,Ga)As QW of the n-doped sample #11309 at $T = 2$ K and E = 1.562 eV. (**b**) Magnetic field dependence of the frequency at $T = 2$ K. (**c**) Spin dephasing time T_2^* as a function of the magnetic fields.

In Figure 3.16(a) is shown the dependence of the TRKR signal on the magnetic field for the sample #11309. We do not observe here long electron spin beats. The fit of these signals gives frequencies, which are displayed in the figure 3.16 (b). The frequencies increase with rise of magnetic field. The extracted value of g-factor is about $|g_e| = 0.15$. The dependence of the spin dephasing time on the magnetic field is represented in Fig. 3.16 (c). As one can see from this dependence, there is no influence of the magnetic field on the spin dephasing time. We suppose that the reason of such behavior correspond to the the Dyakonov-Perel mechanism, which is controlled by the imurity scattering.

Figure 3.17 (a) shows the dependence of the TRKR signal on the magnetic field for the second n-doped sample #11320. We do not observe here long-lived electron

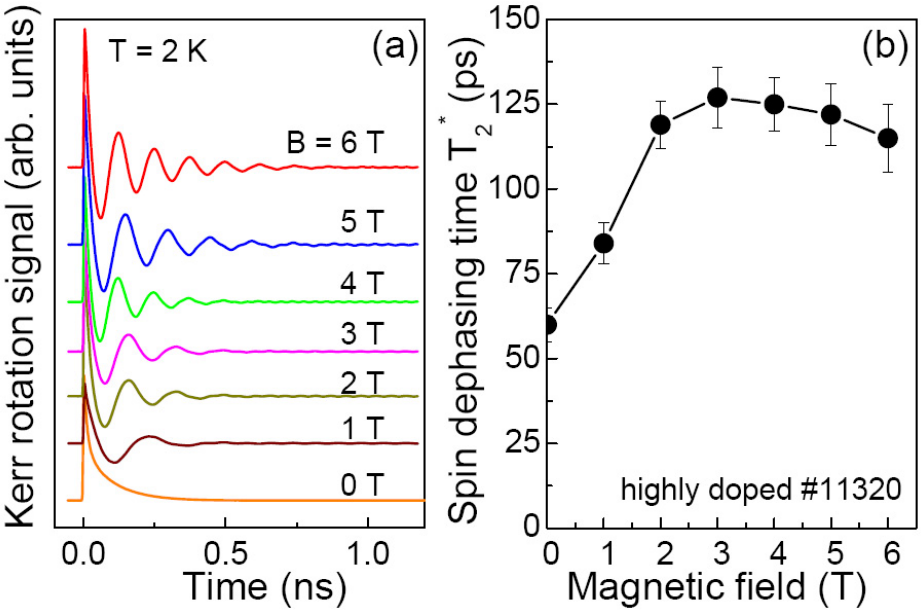

Figure 3.17: (**a**) Time resolved Kerr rotation signal for highly n-doped sample #11320 at $T = 2$ K and $E_{exc} = 1.562$ eV. (**b**) Spin dephasing time T_2^* as a function of the magnetic fields.

spin beatings. The decay time of the oscillation practically does not depend on the magnetic field strength like in the case for the previous sample #11309. The dependence of the spin dephasing time on the magnetic field is represented in Figure 3.17 (b). Magnetic field does not effect spin relaxation time, because $\Omega_k \tau_p \ll 1$, where τ_p is momentum scattering time. Brief details are given in Section 1.6. In Figure 3.18 PL spectra for the samples #Ash-undoped and #Ash-doped are given. A sample #Ash-undoped consist of 20 nm GaAs/$Al_{0.3}Ga_{0.77}$As QW. The sample #Ash-doped, n-doped GaAs/$Al_{0.3}Ga_{0.77}$As QW with a concentartion of about $n = 2 \cdot 10^{11}$ and well width of 25 nm. In Fig. 3.19 (a) is presented Kerr rotations signal measured for the structure #Ash-undoped at $T = 2$ K. A common feature of the signal is a appearance of long-lived beatings. The spin dephasing times evaluated from the fit of these experimental data are shown in the figure 3.19(b) as a function of magnetic field.

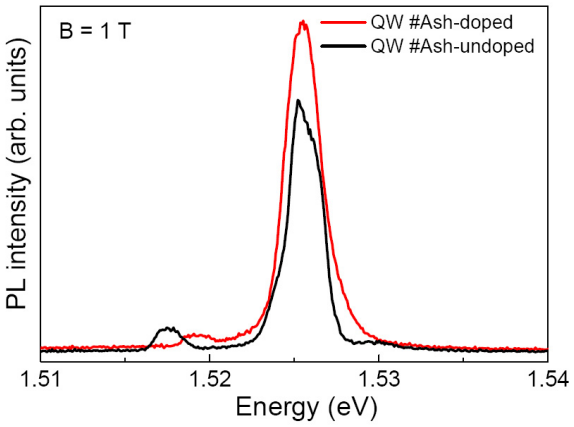

Figure 3.18: PL spectra measured for two samples #Ash-undoped, #Ash-doped at $B = 1$ T

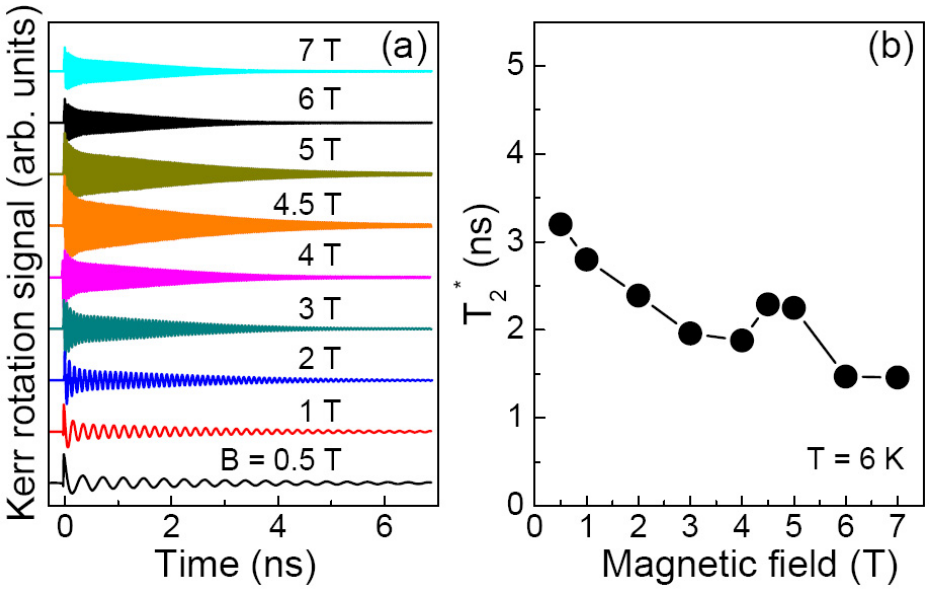

Figure 3.19: (**a**)Kerr rotation signal measured for 20 nm-thick GaAs/$Al_{0.3}Ga_{0.77}As$ QW of the undoped sample #Ash-undoped at different magnetic fields. $T = 6$ K, P_{Pump}= 1 mW, $P_{Probe} = 0.1$ mW. (**b**) Spin dephasing time T_2^* as a function of the magnetic fields.

In order to prove the effect of the variation of the spin dephasing time with doping, we compare the Kerr rotation signal measured at $B = 1$ T for nominanntly undoped GaAs (sample #Ash-undoped) and n-doped GaAs (sample #Ash-doped) quantum wells (see Fig. 3.20). These Kerr roation signals reveal, that the spin lifetime in undoped GaAs quantum well is quit long compare to the n-doped struucture. In case of undoped GaAs QW, the beatings can be seen even at negative time delays. To accurately measure these long spin lifetimes,we measured RSA signal, which is given in the figure 3.20(b). The spin dephasing time extracted from this RSA scan with a fit by Eg. (2.9) is about 11 ns. For n-doped GaAs QW structure is observed very fast decay. The

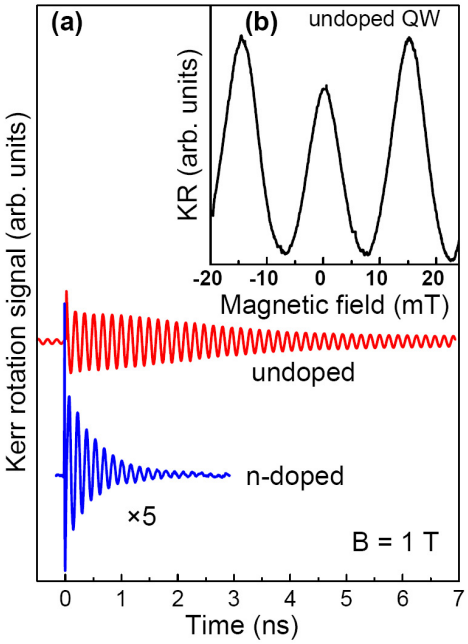

Figure 3.20: (a) Time resolved Kerr rotation signal, measured at $B = 1$ T for two different samples: n-doped 20-nm-thick GaAs/$Al_{0.3}Ga_{0.77}$As QW of the sample #Ash-doped (blue curve) and undoped 20-nm-thick GaAs/$Al_{0.3}Ga_{0.77}$As QW of the sample #Ash-undoped (red curve). (b) RSA signal for undoped sample #Ash-undoped. $B = 1$ T, $T = 6$ K, P_{Pump}= 1 mW.

presence of long-livetimes in undoped GaAs heterostructures and their lack in n-doped qualitative similar to the to that has been observed in other GaAs structures desribed above.

From our experimental results of this section we can conclude, that spin lifetime in doped QW does not depend on the magnetic field.

3.6 The influence of the electron-electron interaction on the temperature dependence of the spin dephasing time.

The next sample 32A21M7 consist of two $Al_{0.1}Ga_{0.9}As$/AlAs Bragg mirrors surrounding a L/2 cavity. A mixed-type QW structure is placed at the antinode of the cavity mode: it contains a 20 nm wide GaAs quantum well, surrounded by two narrow GaAs quantum wells (2.6 nm). The parameters of this sample are given in the chapter 2. Sample is nominally undoped. This structure has attracted our interest, because we can tune electron density and continuously go from studying the spin dynamics of excitons and trions towards a degenerate electron gas. Figure 3.21 shows the PL spectra measured at $B = 0$ T. The sample was excited by He-Ne-Laser with $E_{exc} = 1.61$ eV. Two peaks can be seen here, which we relate to exciton and negatively charged

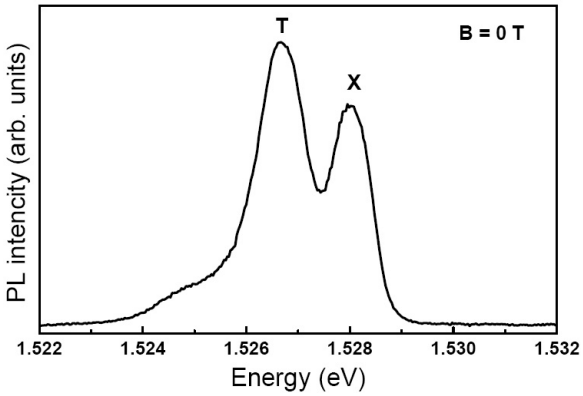

Figure 3.21: The PL spectra of the sample 32A21M7, measured at $B = 0$ T.

trion. With increasing He:Ne power, the exciton line loses intensity, while the trion line becomes stronger (not shown here). In the measurements of spin dynamics by time-

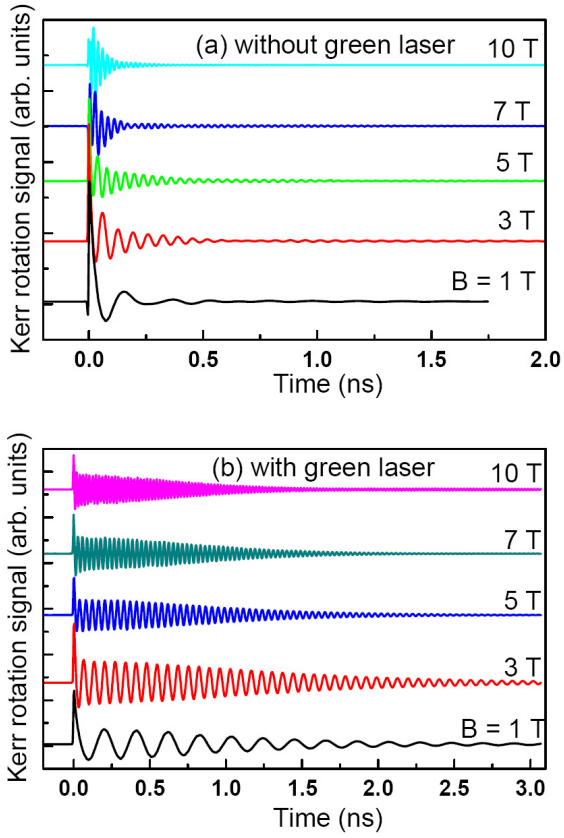

Figure 3.22: Magnetic field dependence of the Kerr rotation signal for 20 nm GaAs/(Al,Ga)As QW of the sample 32A21M7 (**a**) without and (**b**) with additional green laser illumination. $T = 1.7$ K, $E_{exc} = 2.33$ eV

resolved Kerr rotation two different cases have been considered. The Kerr rotation signal was measured with and without an additional illumination of the sample by a

second laser with $E_{exc} = 2.33$ eV. Applying an additional illumination allows to tune electron density in the sample. Figure 3.22 shows the Kerr rotation signal measured at $T = 2$ K with and without additional green laser illumination. It is easy to see that

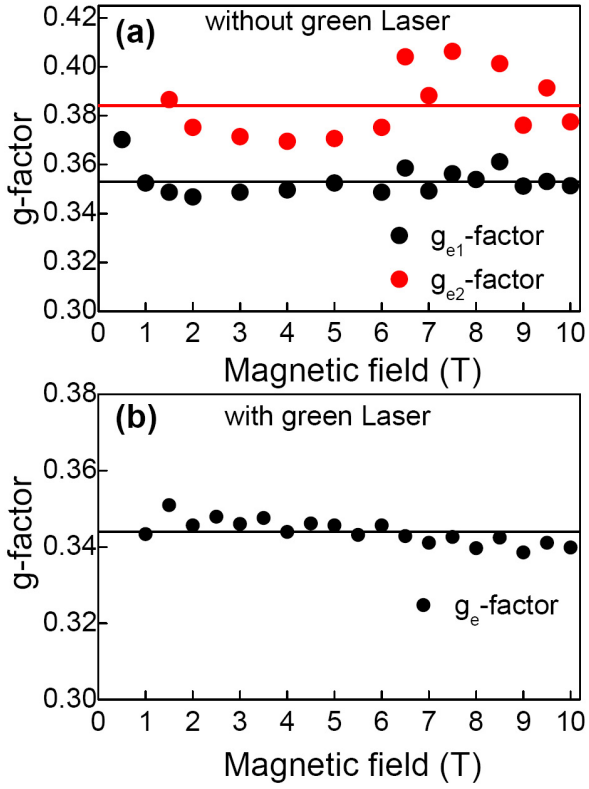

Figure 3.23: Dependence of the $|g_e|$ factor value for 20 nm GaAs/(Al,Ga)As quantum well of the sample 32A21M7 with (**a**) and without (**b**) green laser illumination.

the signal without illumination contains two different frequencies and quickly decay with time. The additional illumination applying leads to result there the Kerr signal describes only with one frequency and decay of the oscillations became considerably slower. As it was explained in section 1.5, the value of g-factor can be evaluated from the frequency Kerr rotation signal. The dependence of g-factors on external magnetic field allows to obtain the mean value of it, see Figure 3.23. So, the signal measured without additional illumination contains two different g-factors. These g-factors we relate with localized $|g_e|= 0.38$ and free electrons $|g_e|=0.35$. Figure 3.23(a) red and black lines respectively. In the case where the additional illumination was applied, we obtain only one g-factor $|g_e|= 0.35$, Figure 3.23 (b). The value of it coincides very well with g-factor of free electrons derived from the experiment without additional illumination. The same set of measurements have been done at temperature $T = 6$ K. In spite of measurements done at $T = 2$ K here we were unable to find two different g-factors. Only signal from free electrons were observed. The purpose of this work is to study the spin dephasing time in different quantum wells heterostructures and its changing depending on the different parameters. For above described sample, the spin dephasing time, retrieved from the fit of the Kerr rotation signal with additional

illumination, is displayed in the Figure 3.24. If the sample is illuminated by the green

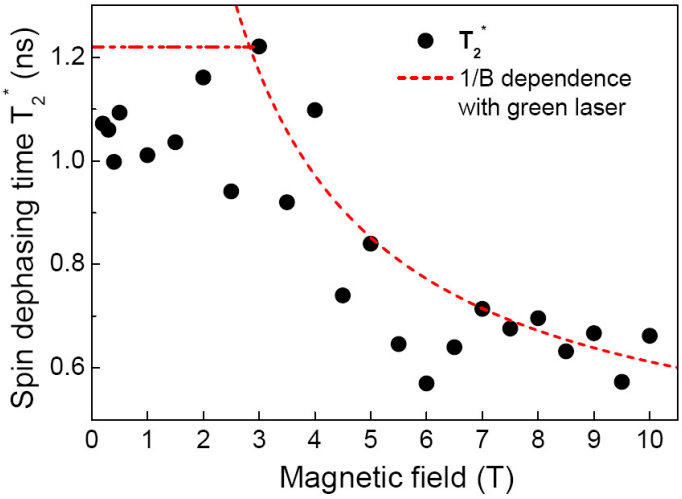

Figure 3.24: Dependence of the spin dephasing time on the magnetic field for 20 nm GaAs/(Al,Ga)As quantum well of the sample 32A21M7.

laser the situation shifts to the free electron case. Here we observe relatively short times about 1.3 ns. Commonly in undoped QWs of similar width, as it shown in Section 3.3 we can measure the spin dephasing time up to 20-30 ns. We identify $1/B$ dependence characteristic to dephasing process caused by inhomogeneity of g-factor.

In Kerr rotation signal measured without additional illumination, we can assign three components, namely the nonoscillating signal related to the hole spin orientation and the oscillations related to precession of the electron spin in the exciton and of the spin induced in the excess electron ensemble. The second long-lived component of the oscillating signal may be related only to precession of the excess spin of resident electrons, formed upon excitation of the trion. The resident electrons oriented by light and their presence is indicated by the doublet structure of excitonic peaks in the luminescence spectrum, see Fig. 3.21. As a consequence, an absorption of a photon may give rise to formation of a trion comprised of a hole and two electrons, namely photogenerated and resident. Due the creation of trions a certain number of the resident electron spins are compensated parallel to the hole spins. As result, an excess spin parallel to those of the photocreated electrons arises in the ensemble of resident electrons.

In case of the measurements with additional illumination [see Fig. 3.22 (b)], the concentration of the carriers is changing, one can see here long-lived oscillations, which can be explained due the contribution of both localzed and delocalied electrons. In Figure 3.25 is plotted temperature dependence of the spin dephasing time T_2^*, extracted from the fit of the Kerr rotation signal, which has been measured in this case with additional green laser illumination. One can distinguish here two regions and two regimes of spin dephasing time changes with increasing temperature. The spin dephasing time first increases in the temperature range between $T = 2 - 10$ K, to the maximum value of 1.9 ns and then increases. We assume that the spin relaxation is caused by the Dyakonov-Perel spin relaxation mechanism according to Eq. (1.21).

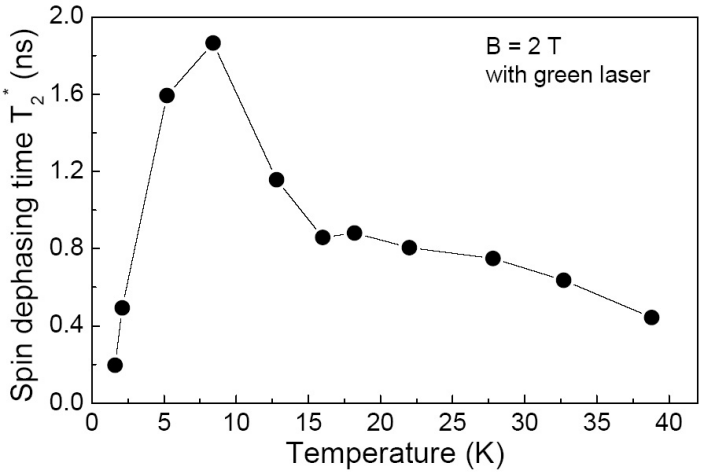

Figure 3.25: Dependence of the spin dephasing time on the temperature for 20 nm GaAs/(Al,Ga)As quantum well of the sample 32A21M7.

The theoretical explanaition of this effect is presented in Section 1.6. The appearance of the maximum in the spin dephasing time as a function of temperature originates from the electron-electron Coulomb scattering which dominates the scattering process at low temperature. It is understood that electron-electron Coulomb scattering has a nonmonotonic dependence on temperature: at low temperature (degenerate limit), the electron-electron scattering time $\tau_{ee} \sim T^{-2}$, while at high temperature (nondegenerate limit), $\tau_{ee} \sim T$ [86]. The minimum of τ_{ee} appears at the transition temperature where the crossover from the degenerate to the nondegenerate regime occurs. Therefore, the contribution of electron-electron Coulomb scattering to inhomogeneous precession broadening due to Dyakonov Perel mechanism has a minimum at the transition temperature. Consequently, the spin dephasing time versus temperature curve exhibits a maximum. This feature agrees with the recent theoretical prediction [86]. Note that the Fermi energy E_F of the 2DEG estimated from the electron density is about 10 K, and coincides with the transition temperature. We now turn to the second region of the temperatures, here the spin dephasing time decreases in the range from 15 to 40 K.

As one can see, the varying of the electron concentration in the studied structure provide evidence of two different systems for free and localized electrons. Additional illumination increases concentartion of the carrier in our structure, the role of the electron-electron collisions becomes important and this leads to the reduction in dynamics. Our results show the importance of the electron-elecron Coulomb scattering to the spin relaxation time due to the Dyakonov-Perel spin relaxation mechanism.

3.7 Spin dynamics in (110) GaAs quantum wells

Many studies of spin dynamics are focused on quantum wells, which are grown on the substrate with the standard crystallographic orientation (001). However, the other orientations of substrate, such as (110) and (111) might be of a great interest for stud-

ies of spin. The general interest for spin manipulation in (110) QWs based on III-V semiconductors started after the theoretically prediction of very long spin lifetimes by Dyakonov and Kacharovski [37]. The spin-orbit coupling associated with the bulk inversion asymmetry, which, in general, provides an important channel for spin relaxation in III-V semiconductors was predicted to be suppressed for spins parallel to the growth direction of (110) QWs. These theoretically results have been confirmed as well experimentally [45, 82, 105]. Very long spin lifetimes (about few nanoseconds) have been demonstrated, which significantly exceed the times achived in (001) structures [83]. For instance, TRFR measurements of T_2^* in (110)-oriented GaAs QWs yield significantly longer spin lifetimes compared with (100)- oriented samples [84]. In order to test the generality of these concepts for our structures, we measured time-resolved Kerr rotation signal in the (110)-oriented sample PDI-M4-2264 as a fuction of magnetic field and temperature. The experiments here are carried out on the sample, which

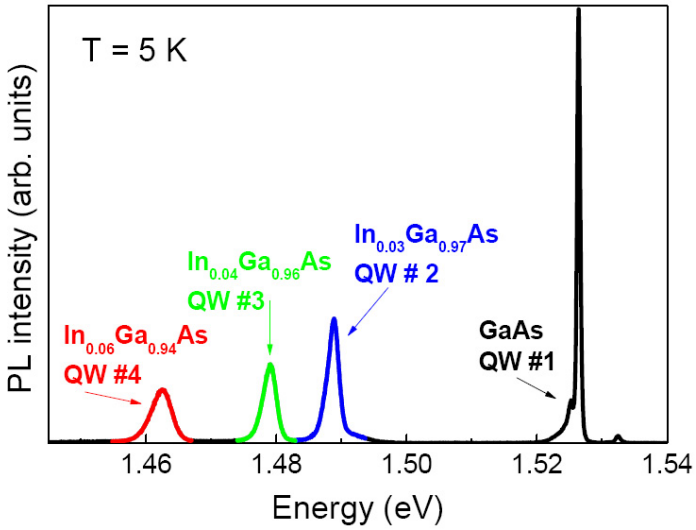

Figure 3.26: The photoluminescene characteristics of the PDI-M4-2264 sample measured at 5 K. For simplicity we mark every QW of the studied structure with a label # and number.

consist of four 20-nm-thick undoped (Ga,In)As QWs with AlGaAs barriers grown by molecular-beam epitaxy on a (110) GaAs substrate. The detailed description of the sample is given in the Chapter 2 and Appendix A. The Figure 3.26 shows the photoluminescence spectra of this structure, measured at $T = 5$ K. For simplicity in this section we mark every QW of the studied structure with a label # and number. The PL has been measured at different temperatures and magnetic fields, in order to have a possibility to control the shift of the spectral line. The all four quantum wells have been studied using the time-resolved Kerr rotation technique. The Kerr rotation signal has been measured as a function of temperature and magnetic fields. The magnetic field was applied in two configurations, parallel to the rough (along [1-10] direction) or to the smooth cleavage (along [001] direction) of the sample. In GaAs the (110) planes are cleavage planes. Looking onto a (110) GaAs substrate the main in-plane crystal direction are [1-10] and the perpendicular [001] direction. The [1-10] direction

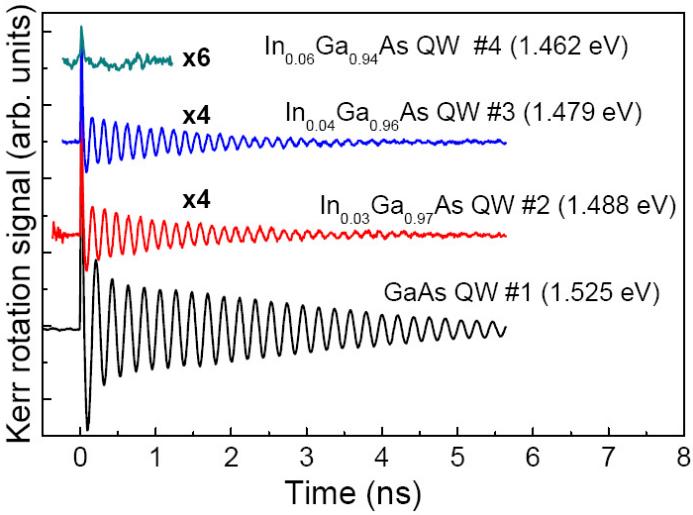

Figure 3.27: The time-resolved Kerr rotation signal measured for four (Ga,In)As QWs of the sample PDI-M4-2264.

is normal to the (1-10) plane (=cleavage plane), therefore if a (110) substrate is cleaved (smooth edge) the cleaved edge will be along [001], which lies in the substrate and in the [1-10] cleavage plane.

The Figure 3.27 displays the typical Kerr rotation signal measured at 1 T magnetic field applied along the rough cleavage. The decay of TRKR signal amplitude provides the spin dephasing time and as one can see here, the signal from the quantum well #1 shows the longest spin dephasing time compare to the other quantum wells of this structure, the beatings can be even observed at negative time delay. The signal from (In,Ga)As quantum wells decays very quickly. The quality of the signal from QW #4 is very bad and weak, that it is even impossible to distinguish here electron spin beats, which suppressed by the noise. We could not detect any significant differences in the signal decay depending on orientation of the magnetic field applied in the plane of the sample. There were no difference in the signals observed in (In,Ga)As and GaAs quantum wells. Figure 3.28 displays the g-factor values extracted from the fit of the Kerr rotation signal, measured for all four quantum wells. For InGaAs quantum wells there are no dependencies of the g-factor values on orientation of magnetic field in plane. On the contrary the g-factor observed in GaAs quantum well depends on magnetic field orientation. This difference in g-factor components along [001] and [110] axes should be studied more detailed theoretically.

Additional illumination was used to increase amplitude of the long-lived component of the oscillated signal,through probable increase of quantity of spin oriented electrons. However the illumination did not contribute any change in our signal. The Figure 3.29 shows the magnetic field dependence of the Kerr rotation signal for QW #1. One can see that the decay of spin beats is enhanced for increasing fields. The curves were fitted with exponential decay function. A non-monotonic form of the experimental curve decays could be occurring due to addition of the signal from photogenerated and resident carriers. The resulting B-field dependence of the spin dephasing time

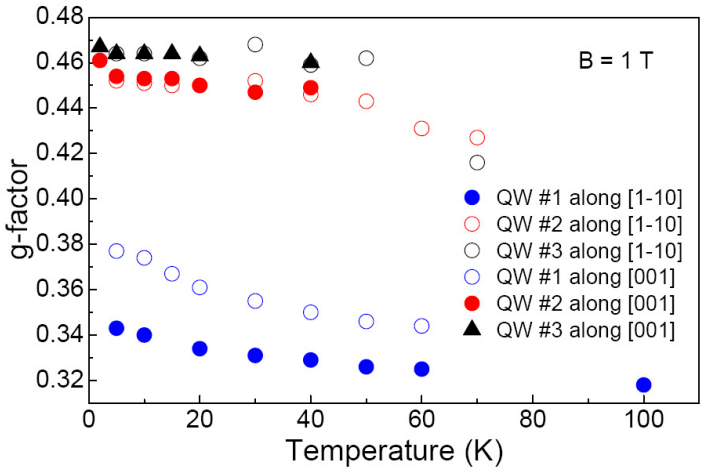

Figure 3.28: The electron g-factors values evaluated from the fit of the Kerr rotation signal, measured at $B = 1$ T for three (GaAs QW #1, $In_{0.03}Ga_{0.97}As$ QW #2, $In_{0.04}Ga_{0.96}As$ QW #3) QW of the structure, along smooth and rough cleavages.

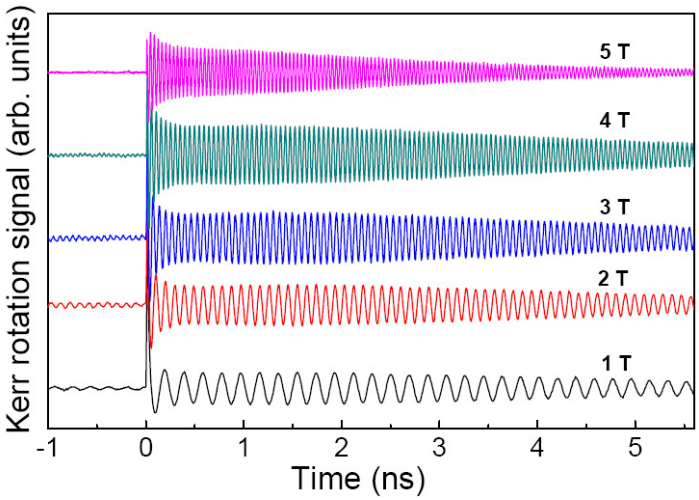

Figure 3.29: Magnetic field dependence of the Kerr rotation signal for GaAs QW #1 along smooth cleavage, at $T = 5$ K, $P_{Pump} = 0.2$ mW, $P_{Ppobe} = 0.08$ mW, $E_{exc} = 1.525$ eV.

T_2^* is given in the Fig. 3.30 (a). The decrease of T_2^* with growing magnetic field can not be described by the dependence $1/B$. The very small spread of the g-factor about ~ 0.001 was estimated approximately from decay in large magnetic field. The Zeeman splitting in Fig. 3.30 (b) shows typical linear dependence on the magnetic field. The resulting value of the electron g-factor equal to $|g_e| = 0.365$. Because of the relative long spin dephasing time observed in QW #1 , the RSA signal has been measured. From the fit of the RSA signal for the QW #1 shown in Fig. 3.31 the spin dephasing time of about 10 ns is extracted. It was measured only a small part of the signal corresponding to the small magnetic field values, we cannot define correctly a spread of the g-factor. The other feature of this structure was that long lived beatings

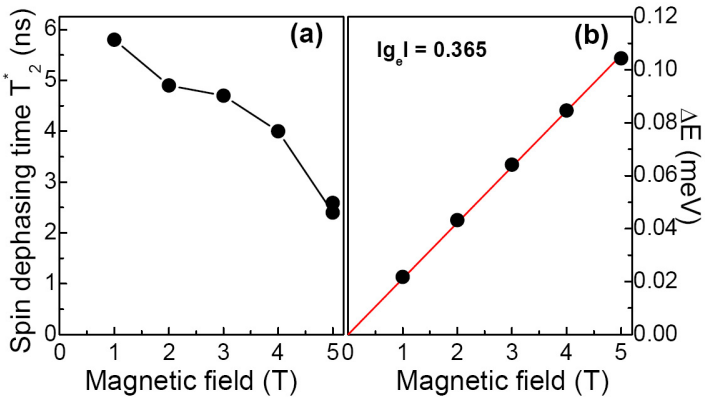

Figure 3.30: Dependence of the spin dephasing time (**a**) and the Zeeman splitting (**b**) on the magnetic field for GaAs QW #1 of the sample PDI-M4-2264.

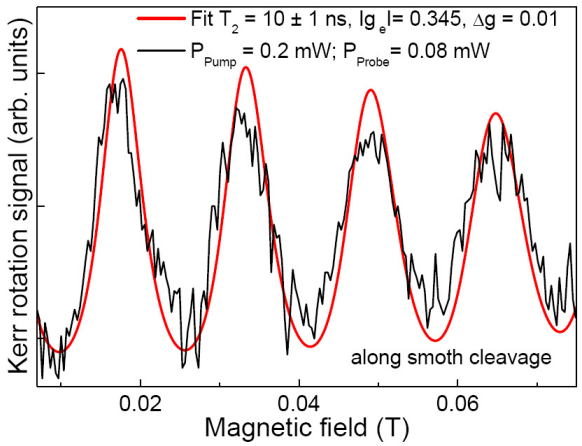

Figure 3.31: Resonant spin amplification signal scaned from 0.01 to 0.07 T bei $T = 5$ K. The spin relaxation time $T_2 = 10$ ns exctracted from the data fit (red line) by Eq. (2.14).

correspond to the very narrow spectral part about 0.5 nm ($E_{exc} = 1.525$ nm). Figure 3.32 shows the temperature dependence of the spin dephasing time for QW #1 at $B = 1$ T. Different values of the T_2^* (red dots) at the same temperature correspond to the different wavelength inside the same quantum well. At temperature of 10 K the spin dephasing time is longer than at 5 K, the results from the fit of the RSA signal present the opposite result, namely $T_2 = 10$ ns at $T = 5$ K and $T_2 = 6$ ns at $T = 5$ K. This temperature behavior may be explained by localization of electrons. At low temperatures the fact of localization plays important role and therefore spread of g-factors can be larger. It can leads to shortening of decay time T_2^* in magnetic field at low temperatures. With temperature rise the effect of delocalization takes over. As result the spin coherence decreases and spin dephasing time increases simultaneously with the growth of temperature. It is difficult to evaluate the spin dephasing time at 2 K, because one can observe there beatings, that could be caused by spectral nearness to the GaAs bulk. The significant result here is the spin dephasing time about 1.28 ns at the $T = 100$ K. In previous chapter we described the results of the temperature

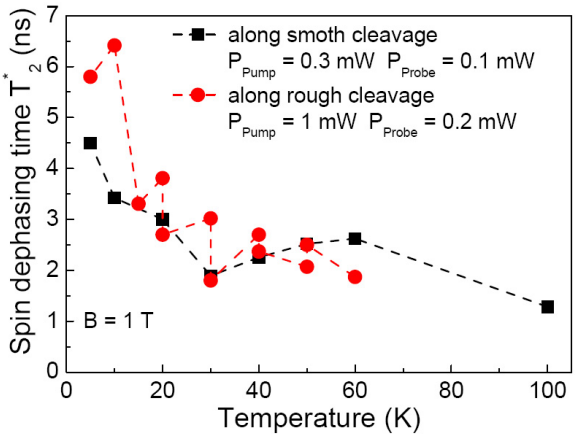

Figure 3.32: Dependence of the spin dephasing time on the temperature for GaAs QW #1 at $B = 1$ T. The results are extracted from the fit of the data measured in the magnetic field configuration parallel to the smooth (red filled circlesred) and to rough (black filled squares) split of the sample.

dependence of the Kerr rotation signal in GaAs quantum wells grown on (100) GaAs substrate. The T_2^* achieved only 0.4 ns at temperature of $T = 90$ K in this structure. In order to understand this effect, the temperature dependence in our structure should be studied more detailed in the future. In Figure 3.33 the temperature dependence

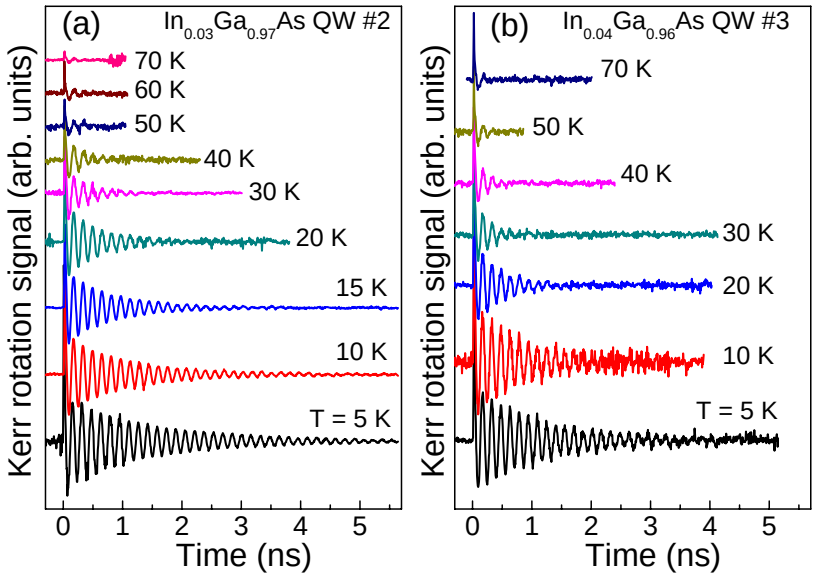

Figure 3.33: The temperature dependence of the Kerr rotation signal for $In_{0.03}Ga_{0.97}As$ QW #2 and $In_{0.04}Ga_{0.96}As$ QW #3.

of the measured Kerr rotation signal in qw #2 and in qw #3 is presented. The signal decays shows typically behavior and decreases with growth of the temperature. The evaluated values of the spin dephasing times, measured in quantum wells #2 and #3 are given in the figures 3.34. The spin dephasing time decreases with the temperature,

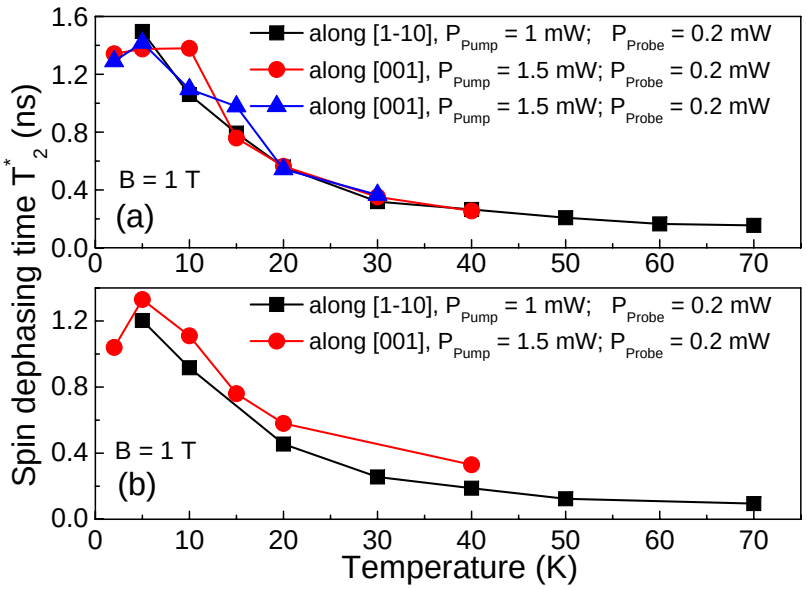

Figure 3.34: Spin dephasing time as a function of the temperature for (**a**) for $In_{0.03}Ga_{0.97}As$ QW #2 and (**b**) $In_{0.04}Ga_{0.96}As$ QW #3 . The results are the fit of the data, measured at different geometries.

it takes place only one small increase in the range of 2-5 K. The spin dephasing time achieves in this range the values about 1.4 - 1.5 ns. The increase of the spin dephasing time occurs because of the effect of the Dyakonov-Perel mechanism. In some cases, the DP dephasing can be considerably reduced, like in (110) oriented QWs, besides the quantum well should be very symmetrical. In other case it result in either suppression of the spin relaxation due to joint contributions from Dresselhaus and Rashba terms.

In order to distinguish contributions from photogenerated and resident electrons in Kerr rotation signal, time-resolved photoluminescence has been additionally measured. Figure 3.35 shows the PL decay curves of the exciton photoluminescence for three quantum wells, which differ in wavelength. These curves were measured using time-resolved PL, for which the wavelength of the pulsed laser was tuned to necessary energy and emission was dispersed by 100 μm monochromator and detected by a streak-camera with S1 photocathode. Excitation densities as low as possible were used to study pure exciton decay avoiding multiparticle occupation effects. The curves have been shifted vertically for clarity. The decay of the different quantum wells is quite similar. The observed decay has been analyzed by a single exponential fit, the decay times τ are indicated at the traces. These times coincide very well with the times that we observed from the fit of the Kerr rotation signal, that is why we can supposed, that the results of our measurements corresponds to the spindynamics of the exciton. As a conclusion one can say, that in (In,Ga)As quantum wells the main contribution to the Kerr signal comes from the photogenerated electrons, while in case of GaAs quantum well both type of carriers, namely photogenerated and resident contribute to the signal.

We observed quite usual spin dynamics in the structure, besides the long spin dephasing time (1.28 ns) measured at high temperature $T = 100$ K for GaAs quantum

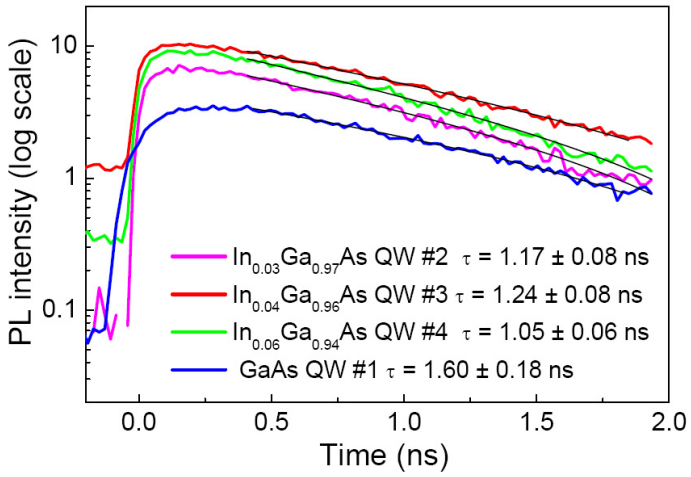

Figure 3.35: Photoluminescense decay for the PDI-M4-2264 sample on logarithmic scale ($T = 1.8$ K). Traces for four quantum wells with exponential fits (black curves). The exctacted decay times τ are displayed in the legend.

well. There is a small increase of the spin dephasing time in the range of 2 - 5 K, but it should be checked more carefully. No significant differences of the signals depending on orientation of the magnetic field applied in the plane of the sample were observed. We found that the g-factor in GaAs quantum well depends on magnetic field orientation. This should be more carefully studied in the future.

In contrast to expectations based upon known spin relaxation mechanisms, we find surprisingly small difference between the spin lifetimes for [1-10] and [100]-orientations of the sample.

3.8 Summary

In this Chapter, we present the study of the electron spin dynamic in GaAs/(Al,Ga)As quantum wells heterostructures using time-resolved Kerr rotation method.

To explore the spin relaxation mechanism, we performed a systematic study of the dependence of the spin dephasing time on the characteristic parameters as temperature, magnetic field and electron concentration.

Electron spin beats have been measured in magnetic field, which precession frequencies allows to determine the transverse component of the electron g-factor. Also we analyzed time-resolved Kerr rotation signal at different magnetic field and studied dependence of the spin dephasing time on the magnetic field. The decrease of the spin dephasing time with increasing temperature has been found to be consistent with the Dyakonov-Perel mechanism for spin relaxation of electrons.

In order to measure the longest electron spin coherence time for the studied samples we have been attending to the lowest possible magnetic fields. For that a modification of the pump-probe Kerr rotation technique known as a Resonant Spin Amplification (RSA) method was used. In our work the electron spin dephasing time $T_2^* = 25$ ns was measured, which is currently the longest time reported in literature for semiconductor GaAs quantum wells.

In addition we investigate the dependence of the spin dephasing time in magnetic field in n-doped QWs. Here we do not observe long electron spin times, the behavior of the time resolved Kerr rotation signal shows independents character on the magnetic field.

We describe an interesting behavior of the RSA signal at low temperature, which has a form of bat. From this shape information about the spin relaxation of both electrons and holes can be derived.

Finally, we studied spin dynamics in (110) GaAs quantum wells. We do not observe a difference between the spin lifetimes in [1-10]-oriented samples in comparison in comparison with [100]-oriented ones.

Chapter 4

All-optical nuclear magnetic resonance

Spins of various nuclear isotopes became currently of great research interest. Nuclei offer extended spin lifetimes and robust spin coherence properties [16]. In III-V semiconductors all nuclei posses non-zero spin and that opens a range of opportunities for addressing this quantum degree of freedom,both coherently and incoherently, using resonant technique or through optical or electrical pumping of spin polarized electrons. In many works [16] it has been shown that the coherence of the electron spin is reduced by fluctuations of the net nuclear spin. This shows, that nuclear and electrons spins in nano-structures should be studied and controlled in a complex.

In this Chapter, we analyze important results of investigation of the electron-nuclear spin system in quantum well heterostructure. We present the observation of effects in RSA signal due to interaction between nuclei and electrons. This chapter starts with an overview of basic interaction of electron and nuclei spins. Then will be given some theoretical results concerning resonant optical cooling of the nuclear spin system. An important parameter such as nuclear spin temperature will be defined.

4.1 Theory of dynamic nuclear polarization

4.1.1 Introduction

The theoretical discussion of consequences of the hyperfine coupling between electronic and nuclear spins presented in the following, are taken from the [78]. In a weak magnetic field $\mathbf{B}$ comparable to the local nuclear field the nuclear polarization due to oriented electrons brings about considerable lowering of the nuclear spin temperature. The cooling of the ensemble of nuclear spins gives rise to a large average nuclei spin $\mathbf{I}_{av}$ aligned along $\mathbf{B}$. The magnitude of $\mathbf{I}_{av}$ corresponds to the average spin in thermal equilibrium of the nuclear spin system in the field $\mathbf{B}_N \sim \mathbf{I}_{av}$ is also directed along $\mathbf{B}$ and leads to either strengthening or weakening of the action of field $\mathbf{B}$. But it is not always the case. Nuclear polarization under optical pumping depends on the average

electron spin $\mathbf{S}$, which in its turn is a function of the nuclear field $\mathbf{B}_N$. This process is similar to the action of the internal feedback in the electron-nuclear spin system. In III-V semiconductors conduction band electrons, as it was shown in the introduction of this thesis, are described by S-type wave functions, the hyperfine interaction being as a rule contact. The Hamiltonian of contact interaction for a lattice with a single spin can be written as

$$\hat{V} = \frac{16\pi}{31}\mu_0\mu_I \sum_{n,m}(\hat{\mathbf{S}}_n\hat{\mathbf{I}}_m)\hat{\rho_n}(\mathbf{r}_n - \mathbf{R}_m). \tag{4.1}$$

Here μ_I and $\mathbf{I}_m$ are the magnetic moment and the spin of the nucleus, μ_0 is the Bohr magneton, $\hat{\rho_n}(\mathbf{r}_n - \mathbf{R}_m)$ is the density operator for electron number n on nucleus number m. $\hat{\mathbf{S}}_n$ and $\mathbf{r}_n$ are the spin operator and radius vector of this electron, and $\hat{\mathbf{I}}_m$ and $\mathbf{R}_m$ are the spin operator and radius vector of nucleus number m.

If the average electron spin $\mathbf{S} \neq 0$ (electrons are polarized), nuclear spins are effected by an average electron field

$$\mathbf{B}_e = +b_e\mathbf{S}. \tag{4.2}$$

where $b_e = -(16\pi/3)\mu_0 n_e \xi^2$, n_e is the electron concentration and ξ is a parameter characterizing the localization of the electron wave function on the nuclei. In their turn the polarized nuclei give rise to an effective nuclear field affecting electron spins

$$\mathbf{B}_N = b_N\mathbf{I}_{av}/I. \tag{4.3}$$

Here $b_N = -(16\pi/3)\xi^2 N\mu_I/g_e$, N is the concentration of nuclei, g is the electron g-factor. These formulas for $\mathbf{B}_e$ and $\mathbf{B}_N$ are obtained under the assumption that the hyperfine interaction is the same for all lattice nuclei. This is realized for electrons in the conduction band. The situation is different in case of localized electrons, which interact with a nucleus depending on the distance R between the nucleus and the localization center. In this case b_e and b_N also depend on R.

The back action of the nuclear polarization on the electron spins comes to their precession in a total field $\mathbf{A} = \mathbf{B} + \mathbf{B}_N$. The magnitude of $\mathbf{S}$ is governed by the balance of the processes leading to generation of oriented electrons, to their disappearance, and to precession in the field $\mathbf{A}$. In the simplest case, when these processes are uniform all over the crystal volume, one can write the following equation for $\mathbf{S}$:

$$B_{1/2}(\mathbf{S} - \mathbf{S}_0) = [\mathbf{A} \times \mathbf{S}], \tag{4.4}$$

where $\mathbf{S}_0 = \mathbf{S}_i\tau_s/(\tau + \tau_s)$ is the magnitude of the average electron spin at $\mathbf{A} = 0$. $\mathbf{S}_i$ is the average spin of the photoexcited electrons at the moment of their generation, τ and τ_s are lifetime and spin relaxation time of the oriented electrons, and $B_{1/2} = \hbar(\tau + \tau_s)(\mu_0 g\tau\tau_s)$ is the characteristic magnitude of the magnetic field. According to the Ref. [78] one obtains the following general expression for $\mathbf{S}$:

$$\mathbf{S} = \frac{\mathbf{B}_{1/2}^2\mathbf{S}_0 + (\mathbf{S}_0 \cdot \mathbf{A})\mathbf{A} + \mathbf{B}_{1/2}[\mathbf{A} \times \mathbf{S}_0]}{\mathbf{B}_{1/2}^2 + \mathbf{A}^2}. \tag{4.5}$$

This complex non-linear dependence of $\mathbf{S}$ on $\mathbf{A}$ causes wide variety of effects under optical orientation of the electron-nuclear spin system of a semiconductor.

4.1.2 Polarization of the nuclear spin system by oriented electrons.

The polarization of optically oriented electrons is transferred to the lattice nuclei due to the hyperfine interaction. For the $I = 1/2$ the spin flux $\mathbf{j}$ to the nuclear spin system can be expressed in the following approximate relation:

$$\mathbf{j} = \mathbf{S}/T_{1s}, \tag{4.6}$$

where T_{1s} is the characteristic time of nuclear polarization due to hyperfine interaction ($T_{1s} > 10^{-2}$ s). If the nuclei Zeeman energy $\mu_I \mathbf{B}$ is of the same order as that of dipole-dipole interaction between neighboring nuclei,this interaction leads to rapid relaxation of the nonequilibrium nuclear spin. The dipole-dipole interaction is characterized by a local field $\mathbf{B}_L$. which is of the order of 1 G for the crystals under consideration. The dipolar relaxation time $T_2 \sim 10^{-4}$s. Thus, $T_{1s} \gg T_2$ and, as a rule, nonequilibrium nuclear polarization can be ignored. Taking into account these estimates one could suppose that significant nuclear polarization due to optical orientation in a weak magnetic field is impossible. However, the experimental results in [78] and theory developed by Dyakonov and Perel give evidence that under optical pumping in a weak field considerable nuclear polarization does occur. We observe this effect as well in our experimental results. One can understand this phenomenon on the basis of the spin-temperature conception. The spin system of the lattice nuclei in a magnetic field is effectively isolated from the lattice since the spin-lattice relaxation time T_1 exceeds by far the spin-spin relaxation time T_2. In other words, spin-spin interaction originating the relaxation to the thermal equilibrium in the nuclear spin system is much stronger than interaction of the nuclei spins with the lattice playing the role of a thermostat. The inequality $T_1 \gg T_2$ makes it possible to characterize the nuclear spin system by the spin temperature Θ.

Under thermal equilibrium nuclear polarization is proportional to the ratio $\mathbf{B}/\Theta$. In a field $\mathbf{B} \neq 0$ a state of the nuclear spin s¡stem may be characterized by the polarization as well as by the spin temperature. The non-triviality of the description of the nuclear spin system by means of the spin temperature conceptions as wells as the physical sense of the spin temperature may be clearly illustrated in the case of zero magnetic field. In this case polarization is zero. At the same time the spin temperature may be well below than that of the lattice. The point is that the polarization in zero field disappears with the relaxation time $T_2 \sim 10^{-4}$ s due to dipole-dipole interaction which violates nuclear spin conservation and is responsible for the rapid angular momentum transfer into the lattice. However, the energy of the nuclear spin system may be changed only in the time $T_1 \gg T_2$ due to the weakness of spin-lattice interaction. Hence during a time T_1 after the magnetic field is switched off and the polarization disappears the state of the nuclear spin system can be characterized by the spin temperature. The essential peculiarity of the optical cooling is a considerable change of the spin temperature directly in a weak field of the order of the local field.

The Zeeman energy change due to optical pumping in an external field comparable with the local one results in cooling of the nuclear spin system.

Let us calculate the reciprocal spin temperature $\beta = 1/\Theta$ in the presence of the oriented electrons. The energy flux into the nuclear spin system due to hyperfine interaction is

$$\mathbf{q}_s = -2\mu_I(\mathbf{B}\cdot\mathbf{j}) = -\frac{2\mu_l}{T_{1s}}(\mathbf{B}\cdot\mathbf{S}). \tag{4.7}$$

on the other hand, as well known from NMR theory [79], the relaxation of the nuclear spin system to the lattice temperature is described by the equation

$$\frac{\partial\beta}{\partial t}|_{rel} = -\beta/T_1, \tag{4.8}$$

where the characteristic time T_1 is of the order of T_{1s}. The energy flux due to this relaxation is

$$\mathbf{q}_i = \frac{dE}{d\beta}\frac{\partial\beta}{\partial t}|_{rel} \approx \mu_l^2(\mathbf{B}^2 + \mathbf{B}_L^2)\beta/T_1. \tag{4.9}$$

Under steady-state conditions and making use of Eq. (4.7) and Eq. (4.9) one get for the reciprocal spin temperature:

$$\frac{1}{\Theta} = \beta = \frac{2T_1}{\mu_I T_{1s}}\frac{(\mathbf{B}\cdot\mathbf{S})}{\mathbf{B}^2 + \mathbf{B}_L^2} \tag{4.10}$$

If spin temperature relaxation is only due to hyperfine interaction, a detailed calculation from **??**Abrah) gives for the ratio $T_1/T_{1s} = T_{1s}/T_{1s}$:

$$\frac{T_{1e}}{T_{1s}} \approx \frac{\mathbf{B}^2 + \mathbf{B}_L^2}{\mathbf{B}^2 + \xi B_L^2}. \tag{4.11}$$

here the parameter ξ depends on the type of spin-spin interaction. For magnetic dipolar interaction $\xi = 2 - 3$ dependent on the correlation degree of the fluctuating electron field on neighboring nuclei. Substitution of Eq. (4.11) into Eq. (4.10) leads to the following expression for β:

$$\beta = \frac{2}{\mu_l}\frac{(\mathbf{BS})}{B^2 + \xi B_L^2}. \tag{4.12}$$

This result is obtained for nuclear spin $I = 1/2$ and is a particular case of the general formula deduced by Dyakonov on the basis of a kinetic equation for the nuclear spin density matrix:

$$\beta = \frac{4I}{\mu_I}\frac{(\mathbf{BS})}{B^2 + \xi B_L^2}. \tag{4.13}$$

As follows from Eq.(4.13), the sign of the spin temperature is defined by the relative orientation of the vectors $\mathbf{B}$ and $\mathbf{S}$. It is easy to change a sign in case of optical orientation.

According to Eq. (4.13) for GaAs in field $\mathbf{B} = \sqrt{\xi}\mathbf{B}_L \simeq 3$ G at $\mathbf{S} = 0.25$, Θ is of the order of 10^7 K. Such cooling makes it possible to obtain the high nuclear polarization in the weak magnetic field $\mathbf{B} \sim \mathbf{B}_L$

$$\mathbf{I}_{av} \simeq \frac{1}{3}\mu_I(I+1)\beta\mathbf{B}. \tag{4.14}$$

At the maximum value $S = 0.25$ with magnetic field $\sqrt{\xi}\mathbf{B}_L$, it comes for GaAs $\mathbf{I}_{av}/\mathbf{I}$=0.42 [78].

4.1.3 Cooling of nuclear spin system in electron field

Inspection of expression eq. (4.13) for quantity $\beta = 1/\Theta$ seems to show that cooling is impossible at $\mathbf{S} \perp \mathbf{B}$. It was found experimentally, however, that the nuclear field affects the electron orientation in an invariable perpendicular geometry ($\mathbf{B} \perp \mathbf{S}$). This effect could be attributed to the nonequilibrium component of nuclear polarization. However since the lifetime of nonequilibrium nuclear polarization is actually the transverse relaxation time T_2, this effect of nuclei , should become negligible already in a transverse field as low as 1G. Experiments reveals though strong manifestations of nuclear polarization at tens of G. This is convenient evidence for the existence of equilibrium nuclear polarization also at $\mathbf{B} \perp \mathbf{S}$. Cooling in this case occurs in the field generated by optically polarized electrons ($\mathbf{B}_e$). It is obvious that the field $\mathbf{B}_e$ is always collinear with $\mathbf{S}$. Taking into account the electronic field $\mathbf{B}_e = b_e\mathbf{S}$ according to [78], one has instead of Eq. (4.13):

$$1/\Theta = \frac{4I}{\mu_I} \frac{(\mathbf{S}_0 \cdot \mathbf{B}) + b_e S^2}{(\mathbf{B} + b_e\mathbf{S})^2 + \xi B_L^2}. \tag{4.15}$$

At $\mathbf{S} \perp \mathbf{B}$ the first term in Eq. (4.15) goes to zero and cooling is only due to the electronic field. Cooling is detected by means of nuclear polarization. The field $\mathbf{B}_N$ is always directed along the sum field $\mathbf{B} = \mathbf{B} + \mathbf{B}_e$. Nevertheless, the precession of the vector $\mathbf{S}$ is determined only by the $\mathbf{B}_N$ component directed along $\mathbf{B}$ since the equation of motion for $\mathbf{S}$ is

$$\mathbf{S} - \mathbf{S}_0 = [\mathbf{B} \times \mathbf{S}](1 + b'_N\beta\mu_I/(4I))/\mathbf{B}_{1/2} = [\mathbf{B} \times \mathbf{S}]\mathbf{K}/\mathbf{B}_{1/2}. \tag{4.16}$$

Equation (4.16) is a direct consequence of eq. (4.4). Here $b'_N = 4b_N(I+1)/3$. Since the component of $\mathbf{B}_N$ along $\mathbf{S}$ does not lead to precession of $\mathbf{S}$ ($[\mathbf{B} \times \mathbf{S}]$), all the role of the field $\mathbf{B}_e$ is to cool the nuclear spin system. The expression (4.16) shows that under optical pumping there arises amplification in the action of the external field $\mathbf{B}$. Hereafter we will refer to the constant K in Eq. (4.16) as the amplification factor. Thus the nuclear spin system plays the role of "amplifier" of the external magnetic field. It is also important that at $\mathbf{S} \perp \mathbf{B}$ the value of β depends only on $\mathbf{S}^2 = (\mathbf{S} \cdot \mathbf{S}_0)$. Thus only $S_z = (\mathbf{S} \cdot \mathbf{S})/S_0$ determines the nuclear spin temperature.

4.1.4 Cooling of optical spin system under modulation of pump light polarization.

The angular momentum of electrons undergoing optical orientation in semiconductors is transferred through hyperfine interaction to the nuclear spin system of the lattice[80]. Thus the nuclear spin system is cooled and in case of applied magnetic field becomes polarized. If the circular polarization of the pump light is keeping constant, the nuclei are polarized with a high efficiency. The polarization is observed to set in over a wide range of magnetic fields in bulk crystals. If the pump light is alternating circularly polarized, this should lead to the completely suppression of polarization of the nuclei.

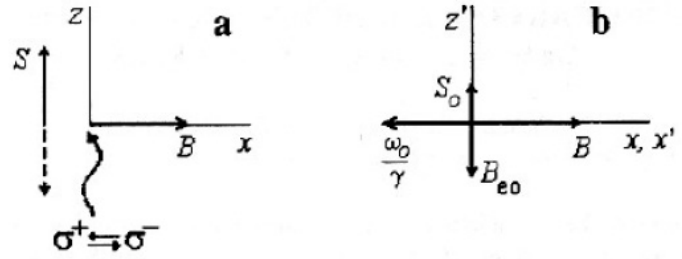

Figure 4.1: Experimental arrangement (**a**) laboratory frame, (**b**) frame rotating about the x-axis with frequency ω_0 in the direction of nuclear spin precession. $\mathbf{S}_0$ and $\mathbf{B}_{e0}$ are, respectively, the average electron spin and field, which are fixed in the rotating frame and rotate with frequency ω_0 about the x-axis in the laboratory frame. $(B_0 - \omega_0\gamma)$ is the x' component of the effective magnetic field in the rotating frame [80].

As it was explained in previous section, it happens, because due to the large nuclear spin relaxation times the average nuclear spin cannot follow fast enough the rapid reversal of the electron polarization. According to this circumstance, the nuclear spin system can become polarized only through its cooling in the polarized-electron field (the Knight field), which oscillates with the frequency of the pump light polarization modulation. If the external magnetic field is perpendicular to the pump beam, the nuclei are polarized within a narrow field interval near the resonant value $B_0 = \omega_0/\gamma$, where ω_0 is the light polarization modulation frequency, and γ is the nuclear gyromagnetic ratio [80, 81]. This resonant cooling of nuclei is accompanied by the resonant change of nuclear polarization and formally can be also assigned to the all-optical NMR. At the same time the resonant cooling has quite different physical nature since it creates the dynamic nuclear polarization by oscillating Knight field. The observation of this effect in bulk semiconductors was shown in the work Ref. [80] Here are presented the theoretical results of observation of a resonant cooling in quantum wells, which was developed by the Ref [82]. In their experiment the sign of the circular polarization alternate at the frequency ω_0 and the external magnetic field $\mathbf{B}$ is applied perpendicular to the pump beam (Fig. 4.1 (a)). The average spin of the optically oriented electrons, $\mathbf{S}$, and the hyperfine interaction field, $\mathbf{B}_e \times (\mathbf{B}_e \propto \mathbf{S})$, generated by electrons on the nuclei are directed along the z axis and oscillate in time: $\mathbf{S} = 2\mathbf{S}_{e0}\cos\omega_0 t$, $\mathbf{B}_e = 2\mathbf{B}_{e0}\cos\omega_0 t$. They conveniently use a rotating (dashed) where both the average spin and the electron field will not explicitly depend on time: $\mathbf{S}' = \mathbf{S}_0$,$\mathbf{B}' = \mathbf{B}_{e0}$ (Fig. 4.1). This allows to use the expression for the nuclear spin temperature, β, obtained for the case of time independent electron polarization. In a rotating frame

$$\beta' = \frac{4I(\mathbf{S}_0\mathbf{B}_{e0})}{\mu\left[(B-B_0)^2 + B_{e0}^2 + \tilde{B}_L^2\right]}, \tag{4.17}$$

where I, μ, and $\tilde{B}_L \sim 1$ Oe are, respectively, the spin, the magnetic moment, and the local field of the nuclei. Recalling that the Overhauser field $\mathbf{B}_{Nx'} \sim \langle \mathbf{I}_{x'} \rangle$, the average nuclear spin $\langle \mathbf{I}_{x'} \rangle = \mu(I+1)\beta'(\mathbf{B} - \mathbf{B}_0)/3$ and $\mathbf{B}_{e0} \sim \mathbf{S}_0$, one can write for the

experimentally observable x-component of the nuclear field

$$B_{Nx} = B_{Nx'} = \frac{-\gamma}{g_x(B - B_0)^2 + B_{e0}^2 + \tilde{B}_L^2}, \tag{4.18}$$

where g_x is the x-component of the conduction-electron g-factor. As readily seen from Eq. (4.18), near $B = B_0$ the B_{Nx} vs B dependence has the shape of dispersion curve, the sign of B_{Nx} being determined by those of the detuning, $(B - B_0)$, and of the γ/g_x ratio. By adding to or subtracting from the external field, the B_{Nx} field affects accordingly the $S_z(B)$ dependence, the resultant curve acquiring the shape of a dispersion signal.

4.2 Experimental results

The polarization of the nuclei by optically spin-polarized electrons takes place on macroscopic time scale of about 10 minutes at low temperatures. This makes spin polarized nuclei interesting for quantum information procession, for instance to use nuclei as a spin memory. In this chapter are presented experimental results for the sample #p340 GaAs/(Al,Ga)As quantum well. All stable isotopes of the GaAs constituents, i.e. ^{69}Ga, ^{71}Ga, and ^{75}As carry a nonvanishing nuclear spin (see Table 4.2, which couples to the electronic system via a Fermi contact interaction, also called nuclear hyperfine interaction. Additionally, even Al has the isotope ^{13}Al, which carriers a nuclear magnetic moment. The basic nuclear parameters for our structure are composed in the following table. During our experiments, sometimes long-term effects

Isotope	***Isotopic* abundance,%**	***Spin***	***Magnetic* moment, μ_N**	***g-factor***	***Frequency,*** T/MHz	B_{res}***(mT)*** at 50 KHz
^{27}Al	100	5/2	3.641	-1.457	0.091	4.50
^{69}Ga	60.4	3/2	2.016	-1.344	0.098	4.88
^{71}Ga	39.6	3/2	2.562	-1.708	0.077	3.84
^{33}As	100	3/2	1.439	-0.959	0.137	6.84

Table 4.1: Basic nuclear data for stable isotopes of GaAs. The magnetic moment is given in units of the nuclear magneton $\mu_N = 5.051 \times 10^{-27}$ J/T.

have been observed on the second and minute timescale, that were small in their effects. Some resonances appear by measuring RSA signal. We attribute these resonances to the nuclei effects. This section will prove, that coupling to the nuclear system is possible, even when using a PEM, and that nuclear fields build up even at small external fields, that have a significant influence on the spin precession. All the data presented here were obtained at low temperatures (2 to 10 K) for the 17.2 nm GaAs quantum well, which has the long spin dephasing times. In order to measure RSA signal, we used general time-resolved pump-probe Kerr rotation technique (see Chapter 2 for details). A Ti:Sapphire laser generated 1.5 ps pulses at a repetition frequency of 75.6 MHz. The laser beam was split in pump and probe beams and the time delay between the pump

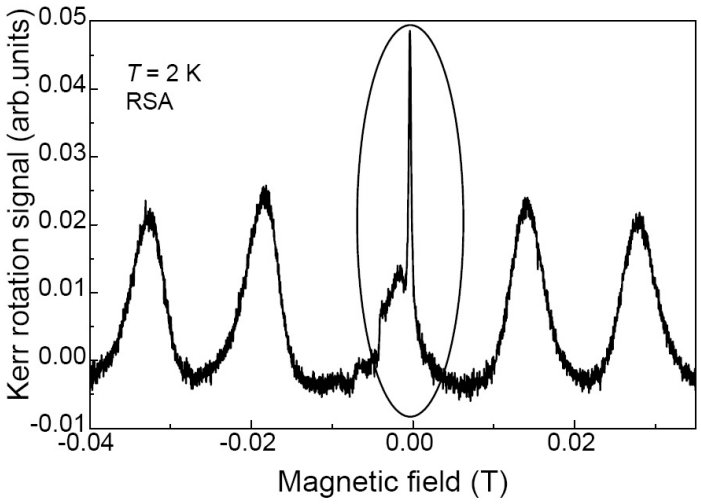

Figure 4.2: Resonant spin amplification signal for a 17.2 nm GaAs/$Al_{0.34}Ga_{0.66}As$ QW sample #p340 measured in the range from -0.05 T to +0.05 T at $T = 2$ K.

and probe pulses was varied by a mechanical delay line. The probe beam was linearly polarized. The pump beam was circular polarized by means of an photo-elastic modulator (PEM) operated at 50 kHz. In other words a photo-elastic modulator (PEM) placed at 45 $^\circ$ to the vertical axis changes the polarization at a frequency of 50 kHz. For a retardation of $\lambda/4$ of the modulator, the polarization state is periodically modulated from left circular to right circular light. In between, the polarization changes from elliptical to linear. In the figure 4.2 is presented RSA signal measured from -0.04 T to +0.04 T at temperature $T = 2$ K. In the picture of the RSA signal is revealed complex structure in the near of the zero peak, which manifests in the splitting of the RSA peak. We suppose to attribute this phenomena to the effect of dynamical nuclear polarization (DNP).

In the Fig. 4.3 a part of the RSA signal, observed by scanning the magnetic field in the range from -0.05 T to +0.05 T at $T = 2$ K is shown. The signal has very unusual form, some peaks appear in the near of zero magnetic field. We assign these unusual behavior to the effect of nuclear spin polarization. In our experiment the pump beam was circular polarized and alternatively pumped with help of PEM at frequency 50 kHz, in this case, according theory given in Ref. [78], the modulation frequency of the order of 10^4 should should eliminate nuclear spin system cooling. In other words polarization of the nuclei will be suppressed. But our experimental results contradict this theory, we observe effects caused by nuclear spin polarization, even in case of alternative pumping by PEM at 50 kHz.

Appearance of the unusual peaks in Fig. 4.3 is one of such examples, proving the presence of nuclear effects. These modulation effects have been explained in Ref. [80], in the following way: if the modulation frequency approach the frequency of nuclear magnetic resonances, it takes place effect - resonance cooling of the lattice nuclei or in other words nuclear spin system cooling in the rotating frame [80]. Such kind of nuclear spin system cooling in the rotating frame is detailed described in Section 4.2.

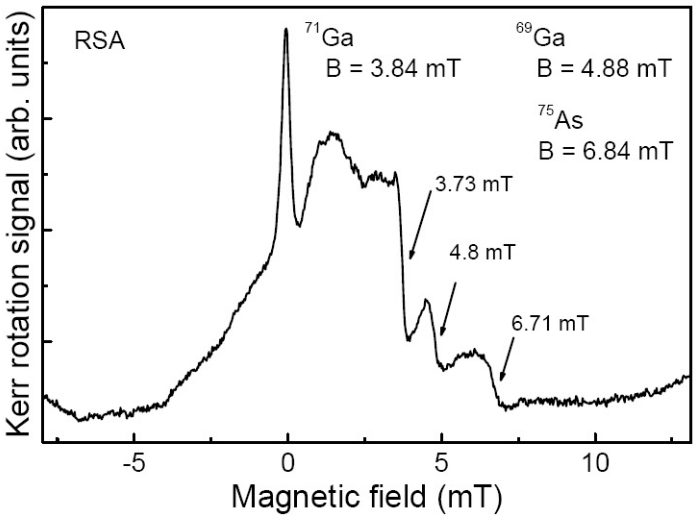

Figure 4.3: Resonant spin amplification signal measured in the range from -50 mT to 50 mT for 17.2-nm-thick GaAs/$Al_{0.34}Ga_{0.66}As$ QW of sample #p340 at temperature $T = 2$ K, $E_{exc} = 1.525$ eV and $P_{Pump} = 0.04$ mW, $P_{Probe} = 0.1$ mW.

Our studied quantum well structure is based on such elements like Ga, As and Al and all these elements have isotopes. Taking into account the frequency of signal modulation 50 kHz we have calculated corresponding resonant values of the magnetic field. Three field position expected for the resonances of three nuclear spin species contained in GaAs, namely ^{69}Ga(60.1%), ^{71}Ga(39.6%) and ^{75}As, are observed (Fig. 4.3). It shows the effect of cooling of the nuclear spin system in semiconductor quantum wells under high-frequency modulation of the polarization of optically oriented electrons [80].

In Figure 4.4 is shown RSA spectra scanned in the range from +0.05 T to -0.05 T at the temperature $T = 2$ K. In this scan are again three resonances comprised. First of these resonance corresponds to ^{71}Ga at $B_{res} = 3.84$ mT, the second to ^{69}Ga isotope with a value of $B_{res} = 4.86$ mT. The third resonance corresponds to As with $B_{res} = 6.838$ mT. In Figure 4.5 is depicted another example of the RSA signal measured at $T = 2$ K, where the effect of nuclei polarization persists as in previous two cases. Here are resonances from the isotopes ^{69}Ga(60.1%), ^{71}Ga(39.6%) and ^{75}As to find. Here in contradistinction to the previous Fig. 4.3, the resonances look less pronounced, this is due to increase of pump power from 0.04 mW to 0.1 mW. Usually, increase of the pump power reduce RSA signal through additional carriers. This means, that excitation power, i.e. the density of optically oriented spins, must have a significant influence on the nuclear field.

As seen from the Fig. 4.3 nuclear field B_{Nx} reverses its sign from positive to negative, as the field B crosses the resonant value for ^{71}Ga nuclei in passing from lower to higher field. Under resonant cooling condition there is the possibility to determine the sing of the electron g-factor. It has been shown in Section 4.3, that according Eq. (4.18) the sign of the effective nuclear field B_{Nx} is determined by the sign of $(B - B_0)$, of the nuclear gyromagnetic ratio γ and of electron g-factor. In case $\gamma > 0$ at $B_0 > \omega_0\gamma$, $B_{Nx} > 0$ for $g > 0$ and $B_{Nx} < 0$ for $g < 0$. At $B_0 > \omega_0\gamma$, the sign of B_{Nx} is

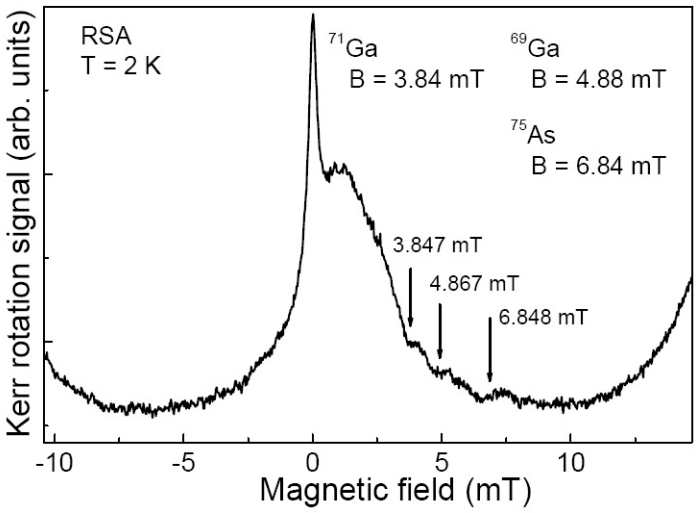

Figure 4.4: Resonant spin amplification signal measured in the range from -50 mT to 50 mT for 17.2-nm-thick GaAs/$Al_{0.34}Ga_{0.66}As$ QW of sample #p340 at temperature $T = 2$ K, $E_{exc} = 1.525$ eV and $P_{Pump} = 0.1$ mW, $P_{Probe} = 0.1$ mW

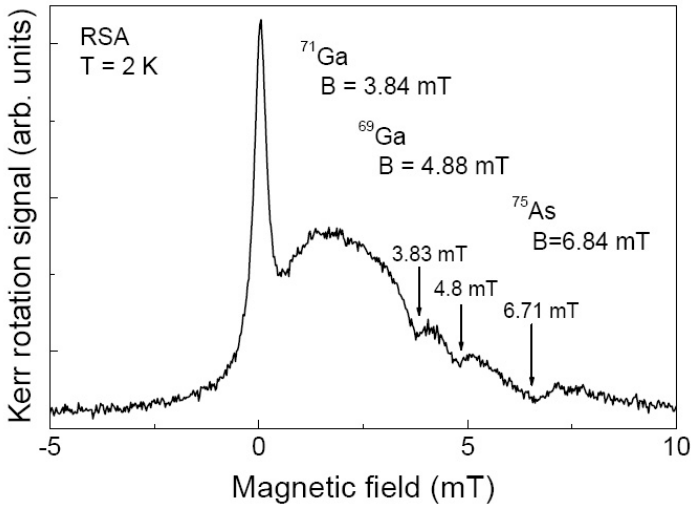

Figure 4.5: Resonant spin amplification signal measured in the range from -50 mT to 50 mT for 17.2-nm-thick GaAs/$Al_{0.34}Ga_{0.66}As$ QW of sample #p340 at temperature $T = 2$ K, $E_{exc} = 1.525$ eV and $P_{Pump} = 0.1$ mW, $P_{Probe} = 0.1$ mW.

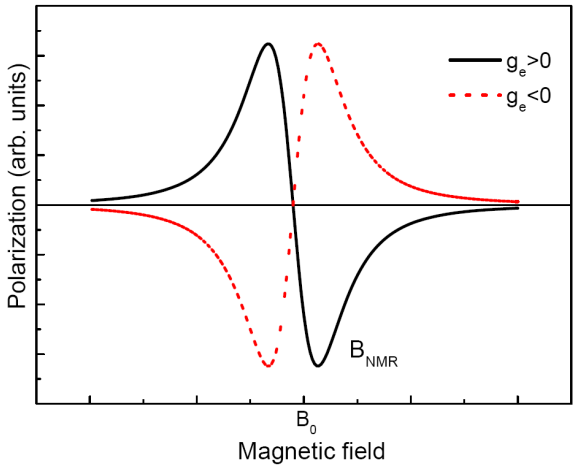

Figure 4.6: Schematically dependence of the B_{Nx} vs B according Eq.(4.18) near $B = B_0$. The sign of B_{Nx} being determined by those of the detuning, $(B - B_0)$, and of the γ/g_x ratio.

reversed [78]. This is schematically displayed in the Fig. 4.6. Near $B = B_0$ the B_{Nx} vs B dependence has the shape of dispersion curve, the sign of B_{Nx} being determined by those of the detuning, $(B - B_0)$, and of the γ/g_x ratio. The sign of the g-factor determines the direction of the total nuclear field created by all nuclear species of crystal lattice. As result we can be determined not only the magnitude of the g-factor by the spin evolution under transverse magnetic field from Kerr signal, but also the sign of g-factor of conduction electrons in semiconductors heterostructures with a help of RSA technique by scanning magnetic field at a fixed time delay.

4.3 Summary

Usually, coupling of the electronic spin system to the nuclear spin system is neglected, because the hyperfine interaction is rather small. However, under certain circumstances, the coupling to the nuclear system can be quite large and, once the nuclear spins are partially polarized, the nuclear magnetic fields may influence the electron spin lifetimes and dynamics significantly. Although it is known, that coupling of the electronic to the nuclear spin system exists at low temperatures [50, 27], it has not been expected to happen when using the photo-elastic modulator, because then, both spin polarizations are being pumped alternatingly at a frequency of $f_{PEM} = 50$ kHz. Thus, no net spin polarization parallel to the external field should build up, which may cause dynamic nuclear polarization. In this section it has been shown, that coupling to the nuclear system is possible, even when using a PEM, and that nuclear fields build up even at small external fields, that have a significant influence on the spin precession. All the data presented within this section were obtained at low temperatures (2 to 10 K) for the 17.2 nm GaAs/(Al,Ga)As quantum well, which has the long spin dephasing times. We demonstrate, that optical detection of nuclear magnetic resonance under modulation of exciting light polarization enables us to determine the sign of the conduction electrons g-factor for nuclei spins.

Chapter 5

Spin dynamics of electrons and holes in (In,Ga)As/GaAs quantum wells at milliKelvin temperatures

Spin dynamics in nanostructures is extensively studied last several years due to promising prospects for spin memory [37]. (In,Ga)As/GaAs quantum wells(QWs) are less studied nanostructures in this respect relative to other type of A_3B_5 heterostructures like GaAs/(Al,Ga)As QWs and (In,Ga)As/GaAs quantum dots. The first investigations of the spin dynamics in (In,Ga)As/GaAs QWs were performed by R.Harley and coworkers [38, 39]. Advantage of structures with the (In,Ga)As/GaAs QWs is transparency of GaAs substrate at the QW exciton transition that allows one to perform experiments in transmission geometry. Investigation of the spin dynamics in (In,Ga)As/GaAs QWs is of large interest. Understanding of the basic mechanisms providing spin relaxation and spin decoherence of electrons and hole as well as appearance of these mechanisms in various experimental conditions, e.g. external magnetic field, lattice temperatures, etc., is of great importance. From this point of view it is very important to observe one of such parameters like temperature and its influence on the spin relaxation times. In quantum well structures two-dimensional electrons are need to be localized at liquid helium temperatures to demonstrate relaxation times in the order of tens of nanoseconds [28, 36]. Under these conditions the spin relaxation times for resident hole can exceed the values about of few nanoseconds [13, 73, 14, 72]. The temperature range below the boiling temperature of pumped ^{4}He of 1.5 K is essential for carrier spin dynamics in quantum wells. However the available experimental data are very limited here, mostly due to the demanding efforts for performing experiments with ^{3}He and the complicated direct optical assess to the sample in this case.

5.1 Detection of Faraday rotation and ellipticity signals

In this Chapter results of Faraday rotation (FR) and ellipticity measurements for n-doped (In,Ga)As/GaAs quantum well of the sample #11708 are presented. The detailed description of this sample is given in Section 2.4. The structure was optically characterized measuring the photoluminescence (PL) spectra and kinetics. At an excitation to the barrier GaAs exciton, two PL peaks separated by $\Delta E_{XT} = 1.4$ meV are observed as shown in Fig. 5.1. We attribute these peaks to the exciton ($E_X = 1.440$ eV) and negative trion ($E_T = 1.438$ eV) transitions [36]. When the excitation photon energy corresponds to the intra-well InGaAs optical transitions, the only trionic PL is observed. This is probably due to smaller absorption coefficient for the transitions that results in the less efficient exciton creation. Examples of the PL spectrum are shown in Fig. 5.1. We also found that the excitation much above the GaAs exciton transition also results in the single intense PL peak which corresponds to the trionic transition. We explain this effect by effective generation of the hot electrons and holes in the GaAs barrier layers. Due to higher mobility of the electrons, they more efficiently occupy the quantum wells. The inset of the Fig. 5.1 shows typical PL kinetics measured at the

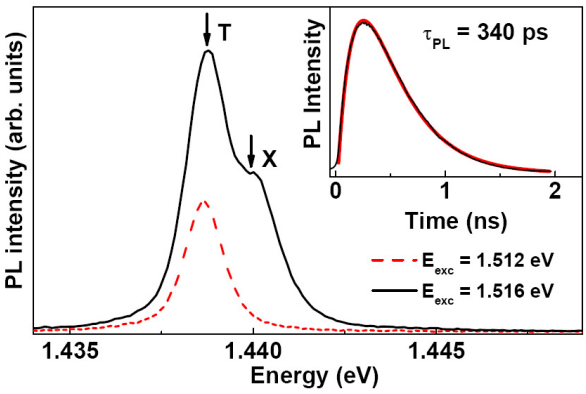

Figure 5.1: The photoluminescence spectrum of $In_{0.09}Ga_{0.91}As/GaAs$ QWs (sample #11780) for the excitation in the barrier GaAs exciton (red line) and below the barrier (dashed black line). The insert gives PL decay measured with low excitation. The red curve is the fit by Eq. (5.1).

trionic peak. It is well fitted by equation

$$I_s = I_0[\exp(-t/\tau_{PL}) - \exp(-t/\tau_r)] \tag{5.1}$$

which includes the PL rise and decay terms with characteristic time constants τ_r and τ_{PL}, respectively.

For experimental results presented in this chapter we performed pump-probe measurements in two regimes, namely in degenerate and in nondegenerate. In degenerate regime the probe comes from the same laser as the pump, in nondegenerate two lasers are synchronized.

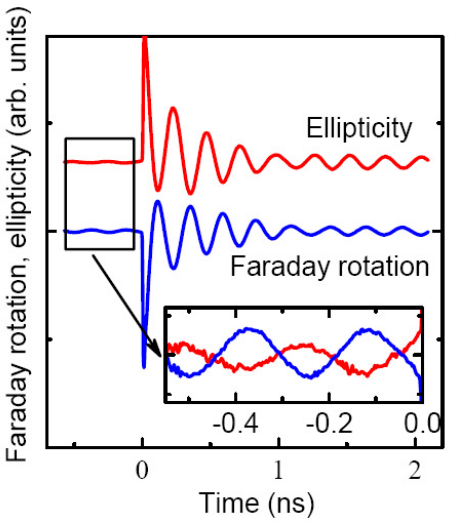

Figure 5.2: Time-resolved Faraday rotation and ellipticity signals measured for $In_{0.09}Ga_{0.91}As/GaAs$ QWs in nondegenerated regime (pump at 1.440 eV, probe at 1.439 eV). Signals are vertically shifted for clearness. $T = 1.6$ K. Inset: Long-lived parts of the signals shortly before pump pulse arrival.

Figure 5.2 shows Faraday rotation and ellipticity signals obtained in nondegenerated regime at $B = 0.5$ T. This experiment was performed in Voigt configuration, i.g. magnetic field $\mathbf{B} \perp \mathbf{k}$, where $\mathbf{k}$ is the light propagation direction. The direction of light propagation coincides with the structure growth axis, noted as z-axis, x-axis is chosen for the magnetic field direction. The pump energy was tuned to the exciton resonance and signal was probed at a different energy in vicinity of the trion resonance. Pump and probe spectral positions are shown by arrows in Fig. 5.1. The Faraday rotation and ellipticity signals look similar to each other. They contain fast decaying part with a time of 360 ps which is a typical recombination times for excitons and trions in such QWs (see the inset of Fig. 5.1). Therefore we assign this component to the spin dynamics of photogenerated carriers [54, 34]. Additionally a long-lived component can be seen at times exceeding 1 ns, which can be even traced at delays of about 13 ns in the inset of Fig. 5.2, i.e. shortly before the pump pulse arrival. The long-lived signal is caused by a generation of spin coherence for the resident electrons and its decay is solely controlled by the electron spin dephasing time, which can be as long as 55 ns in the studied structure [36].

The mechanism of generation spin coherence for the resident electrons are shortly described in Section 1.7, the more detailed explanation is given in Ref. [34]. The main point is formation of trion from a spin oriented exciton generated by the pump. The trion formation is accompanied by a capture of a resident electron with defined spin orientation, which results in polarization of the resident electron ensemble.

Spectral dependencies of the long-lived oscillations in the Faraday rotation and ellipticity signals are shown in Fig. 5.3. The experimental data measured at relatively large positive pump-probe delay of 2 ns and a small negative delay (shortly before pump pule arrival) are given in panels (a) and (b), respectively. The Faraday rotation

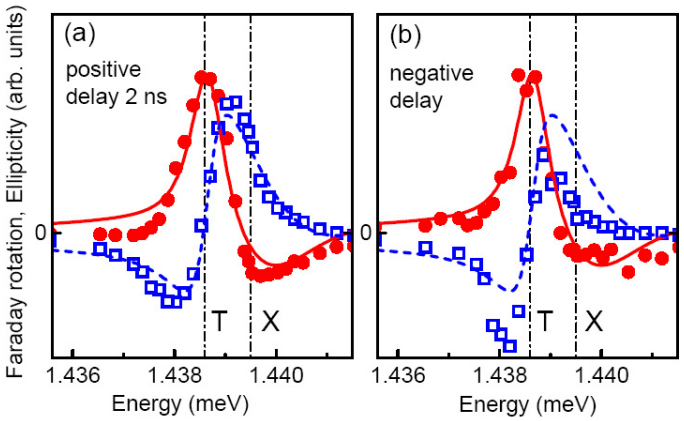

Figure 5.3: Dependencies of long-lived signal amplitudes of Faraday rotation (open squares and dashed lines) and ellipticity (closed circles and solid lines) on spectral position of probe for the sample #11708. $B = 0.5$ T and $T = 1.6$ K. Experimental data are shown in panel (a) for a positive pump-probe delay of 2 ns and in panel (b) for a small negative delay. Pump at 1.4395 eV. Lines in both panels are fits by Eqs. (5.4) and (5.5) with the following parameters: $\hbar\Gamma_{\rm T} = 0.65$ meV, $\hbar\bar{\Gamma}_{\rm X} = 2.5$ meV, $\hbar\beta_{\rm X}/\alpha_{\rm T} = 1.56$ meV, $\hbar\omega_{\rm T} = 1.4386$ eV, $\hbar\omega_{\rm X} = 1.4395$ eV.

and ellipticity signals obviously demonstrate quite different spectral behaviors. The maximum of the ellipticity signal and the zero of the FR signal are close to the trion resonance energy. Also, there is an extra feature in the ellipticity signal around the exciton resonance.

The Faraday rotation, $\mathcal{F}$, and ellipticity, $\mathcal{E}$, of the probe pulse are proportional to the imaginary and real parts of the difference of quantum well transmission coefficients for σ^+ and σ^- polarizations, $t_\pm$, respectively. Taking into account that for the relatively thin quantum wells studied here $t_\pm = 1 + r_\pm$ where $r_\pm(\omega)$ are the corresponding quantum well reflection coefficients [34, 74]

$$\mathcal{E} + \mathrm{i}\,\mathcal{F} \propto r_+(\omega) - r_-(\omega). \tag{5.2}$$

Equation (5.2) is valid provided that $r_\pm(\omega) \ll 1$ which is the case for the studied system. The difference between r_+ and r_- arises from the pump-induced spin polarization of the resident carriers. The quantum well reflection coefficients contain contributions from the exciton (X) and trion (T) resonances:

$$r_\pm(\omega) = \sum_{i={\rm T,X}} \frac{\mathrm{i}\Gamma_{0,i}^\pm}{\omega_i^\pm - \omega - \mathrm{i}(\Gamma_{0,i}^\pm + \Gamma_i^\pm)}. \tag{5.3}$$

Here $\omega_i^\pm$ are the resonance frequencies of exciton (i =X) and trion (i =T) for the corresponding circular polarizations, $\Gamma_{0,i}^\pm$ and $\Gamma_i^\pm$ are the radiative and non-radiative dampings, respectively (see Section 2.1.2).

When the spin polarized resident electrons are probed by linearly polarized light different physical processes are responsible for the Faraday rotation and ellipticity signals, depending on whether the probe is resonant with either the trion or the exciton

resonance. This is explained schematically in Fig. 5.4. The linearly polarized probe pulse can be decomposed into two circularly polarized components, one of which interacts with the spin-polarized resident electrons more efficiently compared with the other. For the trion resonance shown in Figs. 5.4(a) and 5.4(c) the main modulation

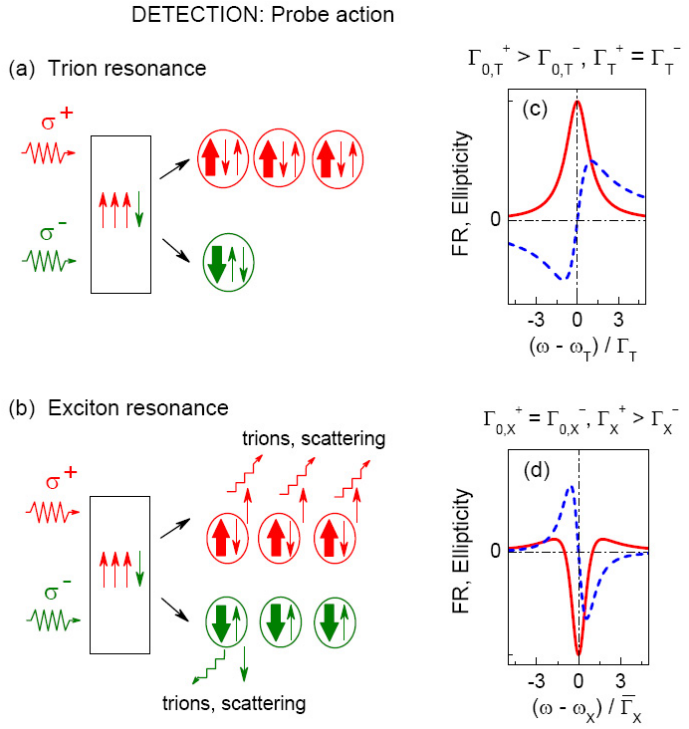

Figure 5.4: Schematic illustration of the Faraday rotation and ellipticity signal formation for probing the trion [panels (a) and (c)] and exciton [panels (b) and (d)] resonances. Thin arrows show electron spins, thick arrows show z component of a photocreated hole spin. The imbalance of spin-up and spin-down resident electrons results in different interaction efficiencies of the σ^+ and σ^- probe components with the resident carriers. In case of trion resonance detection the trion oscillator strength for a given polarization is directly proportional to the number of electrons with corresponding spin z component, i.e. if $N_+ > N_-$ the σ^+ component of the linearly polarized probe is reflected more efficiently compared with the σ^- component because more trions can be formed then. In case of exciton resonance detection the damping rates for excitons created by the σ^+ and σ^- components of the probe are different. For $N_+ > N_-$ the non-radiative broadening of σ^+ created excitons is higher since they participate more efficiently in the formation of trions and in the exchange electron-exciton scattering processes and the reflectivity in this polarization is smaller.

contribution is caused by the trion radiative broadening $\Gamma^{\pm}_{0,\mathrm{T}}$ (trion oscillator strength). The trion oscillator strength in the $\sigma^{\pm}$ polarizations is proportional to the number of electrons with z spin component $\pm 1/2$, $N_{\pm}$. Hence, $\Gamma^{\pm}_{0,\mathrm{T}} = \alpha_{\mathrm{T}}\Gamma_{0,\mathrm{X}}N_{\pm}$, where $\Gamma_{0,\mathrm{X}}$ is the exciton radiative broadening calculated by neglecting electron spin polarization, and α_{T} is a constant related with the effective trion area [75]. As a result, the difference

of reflection coefficients in Eq. (5.2) takes the form

$$\mathcal{E} + \mathrm{i}\,\mathcal{F} \propto \frac{\mathrm{i}\alpha_\mathrm{T}\Gamma_{0,\mathrm{X}}(N_+ - N_-)}{\omega_\mathrm{T} - \omega - \mathrm{i}\Gamma_\mathrm{T}}, \tag{5.4}$$

where we exploited the fact that the non-radiative broadening Γ_T exceeds by far the radiative one, $\Gamma_{0,\mathrm{T}}$. The corresponding shapes of the FR and ellipticity signals are shown in Fig. 5.4(c). The FR is an odd function of the detuning of the probe energy from the trion resonance, while the ellipticity is an even function.

For the exciton resonance shown in Figs. 5.4(b) and 5.4(d) the situation is different compared to the trion resonance. At low temperatures and in presence of spin polarized resident electrons the dominant modulation effect results from the spin dependent non-radiative damping of the excitons: $\Gamma_\mathrm{X}^\pm = \bar{\Gamma}_\mathrm{X} + \beta_\mathrm{X} N_\pm$. Here $\bar{\Gamma}_\mathrm{X}$ is the exciton non-radiative broadening, which does not depend on the exciton spin orientation. The spin-dependent part of the exciton broadening, $\beta_\mathrm{X} N_\pm$, is caused by two processes: the exchange electron-exciton scattering and the trion formation by the photogenerated exciton and a spin-polarized resident electron, see Fig. 5.4(b). Here β_X is a constant characterizing the efficiency of these spin-dependent mechanisms [75, 34]. As a result the exciton contributions to the ellipticity and FR signals has the form

$$\mathcal{E} + \mathrm{i}\,\mathcal{F} \propto -2\frac{\Gamma_{0,\mathrm{X}}\beta_\mathrm{X}(N_+ - N_-)}{(\omega_\mathrm{X} - \omega - \mathrm{i}\bar{\Gamma}_\mathrm{X})^2}, \tag{5.5}$$

where we also neglected $\Gamma_{0,\mathrm{X}}$ compared with $\bar{\Gamma}_\mathrm{X}$. The corresponding exciton contributions to the FR and ellipticity signals are plotted in Fig. 5.4(d). The signs of the signals are inverted as compared with the trion case in Fig. 5.4(c). This is because for a given circular polarization the presence of spin polarized electrons decreases the reflectivity of an exciton, while the reflectivity of a trion is enhanced [75]. The ellipticity signal has its minimum at the exciton resonance frequency and changes its sign at the wings, while the FR signal is an odd function of the detuning between exciton resonance and probe optical frequency.

In Figs. 5.3(a) and 5.3(b) the measured dispersions of the FR and ellipticity signals are compared with the theoretical model. The signals are the superpositions of the exciton and trion contributions, as clearly seen at the higher energy side of the ellipticity signal measured for positive delays where it changes sign, Fig. 5.3(a). A similar trend is also observed for negative delays, Fig. 5.3(b), however the exciton contribution is less pronounced there.

We attribute the differences in the spectral behavior of the measured signals at positive and negative delays to the fact, that there are two subensembles of resident electrons, see Ref. [34]. The electrons with stronger localization demonstrate longer spin relaxation time. They make a major contribution to the pump-probe signal at negative delays and modulate the signal at the trion frequency more efficiently as compared with the less localized carriers. The latter have shorter spin relaxation times so that their contribution is more pronounced in the signals at positive delays. This conclusion is supported by the observation, that two Larmor frequencies which lie quite close to each other are detected for the long-lived signalthis results are presented in the next Section.

5.2 Spin coherence initialization and resonant spin amplification

The observation of electron spin polarization before the next pump pulse arrival indicates that the spin relaxation time is comparable or longer than the laser repetition period of 13.2 ns and that spin polarization may accumulate from pulse to pulse. The resonance spin amplification technique (RSA), which is considered in Sec. 2.2 allows to extract values of long spin relaxation times with high accuracy [35].

In the following part we will discuss results of the Faraday rotation RSA experiments measured under degenerate conditions, in this case the pump and probe beams are produced by the same laser pulse. We have checked that the ellipticity RSA data bring us to the same values of the spin relaxation times as extracted form the FR results. Figure 5.5 shows RSA signals measured for degenerate pump/probe conditions

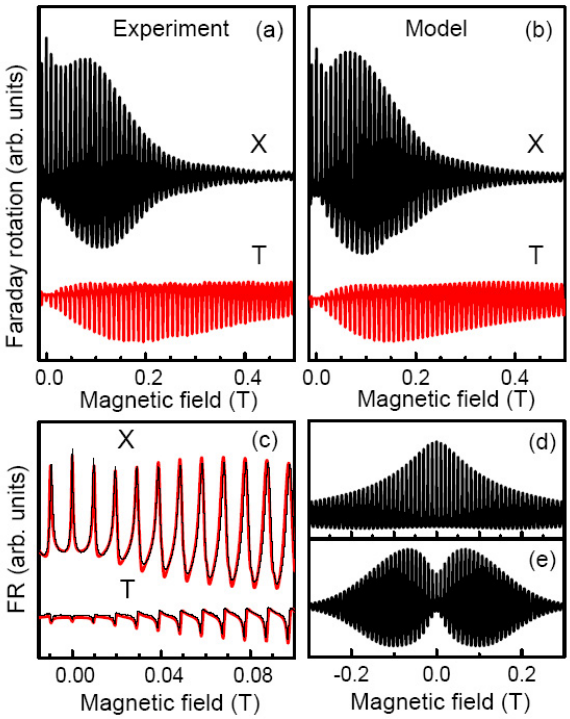

Figure 5.5: (a) and (c) RSA signals measured in degenerate pump/probe regime at the trion and exciton resonances at $T = 1.8$ K for $In_{0.09}Ga_{0.91}As/GaAs$ QWs of the sample #11708. Black curves in panel (c) are RSA experimental data and thick red (grey) curves are fits by Eq. (2.14). (b) Modeled RSA signals for the trion and exciton resonances. The two components in the theoretical RSA signal for exciton resonance due to spin orientation by exciton or trion absorption are shown separately in panels (d) and (e), respectively. Calculation parameters are: $T_s^e = 45$ ns and $\tau_r = 120$ ps. For RSA on trion resonance: $|g_e| = 0.555$, $\Delta g_e = 0.002$, $T_s^h = 2.5$ ns. For RSA on exciton resonance: (i) spin orientation by excitons $|g_e| = 0.535$, and $\Delta g_e = 0.003$; (ii) spin orientation by trions: $|g_e| = 0.550$, $\Delta g_e = 0.008$, $T_s^h = 1.8$ ns.

at the trion and exciton resonance energies. The peaks in the RSA signals correspond to the spin precession frequencies which are commensurable with the laser repetition frequency. From the peak width the electron spin relaxation time T_s^e, which in this case corresponds to the spin dephasing time $T_{2,e}^*$ of the electron spin ensemble precessing about the magnetic field, can be evaluated [35].

The spin amplification signals measured on the exciton and trion resonance qualitatively differ from each other, see Fig. 5.5(a). They deviate also from the typical RSA shape with decreasing peak amplitude and increasing peak width with increasing magnetic field, see Section 2.2 and Fig. 5.5(d). For the trion resonance the signal amplitude is strongly suppressed at zero magnetic field and the amplitude increases with growing field strength. For the exciton resonance the signal has a complicated shape, which results from a combination of the typical RSA signal from Fig. 5.5(d) and the trion bat-like signal shown in Fig. 5.5(e).

The strong difference between the signals measured at the exciton and trion energies suggests that different mechanisms are involved in spin coherence generation. The strong suppression of the RSA signal at $B = 0$ for trion excitation and its bat-like shape serves as direct evidence of the long spin relaxation time of the hole involved in the trion [36]. Indeed, in absence of the magnetic field the long-lived electron spin coherence at trion excitation can be generated only as much as the hole spin in trion flips, compare Figs. 5.6(a) and 5.6(b). If the hole spin relaxation time T_s^h exceeds by far the trion recombination time, τ_r, the resident electron left behind after trion recombination has the same spin as before and no long-living spin coherence for the resident electrons is generated, Fig. 5.6(a). With increase of the magnetic field the resident carrier spins and the spins of the electron returning from the trion are no longer parallel to each other and the RSA signal increases, see Fig. 5.6(c). Interestingly, for exciton resonant excitation (see Fig. 5.5) the signal is not suppressed at $B = 0$, which shows that electron spin coherence is efficiently excited even in the absence of electron spin rotation. The corresponding mechanism of resident electron spin coherence generation can be related with the spin flip-flop exchange scattering between a resident electron and a photoexcited electron in the exciton. In such a case the hole spin-flip is not needed: right after the flip-flop scattering an uncompensated resident electron spin appears (Fig. 5.7). This exchange scattering process may be the dominant channel for spin coherence generation at weak magnetic fields, while with increasing magnetic field the spin coherence generation via the trion state becomes more efficient. This results in the increase of the RSA amplitude for fields $B > 50$ mT, as one can see in the Fig. 5.5(a).

The bat-like trion signal shown in Fig. 5.5(a) can be modeled with good quantitative agreement, as seen from the comparison of the black and grey lines in Fig. 5.5(c), according to the model developed in the Ref. [36] and briefly described in Section 2.2. An infinite sequence of pump pulses with repetition period T_R creates an electron spin polarization periodic in time [42, 36]. The electron spin polarization, $\widetilde{s}_z$, shortly before pump pulse arrival is described by Eq. (2.14).

In order to fit the complicated shape of the RSA signal measured at the exciton resonance we used a sum of contributions due to spin orientation by trion and by exciton.

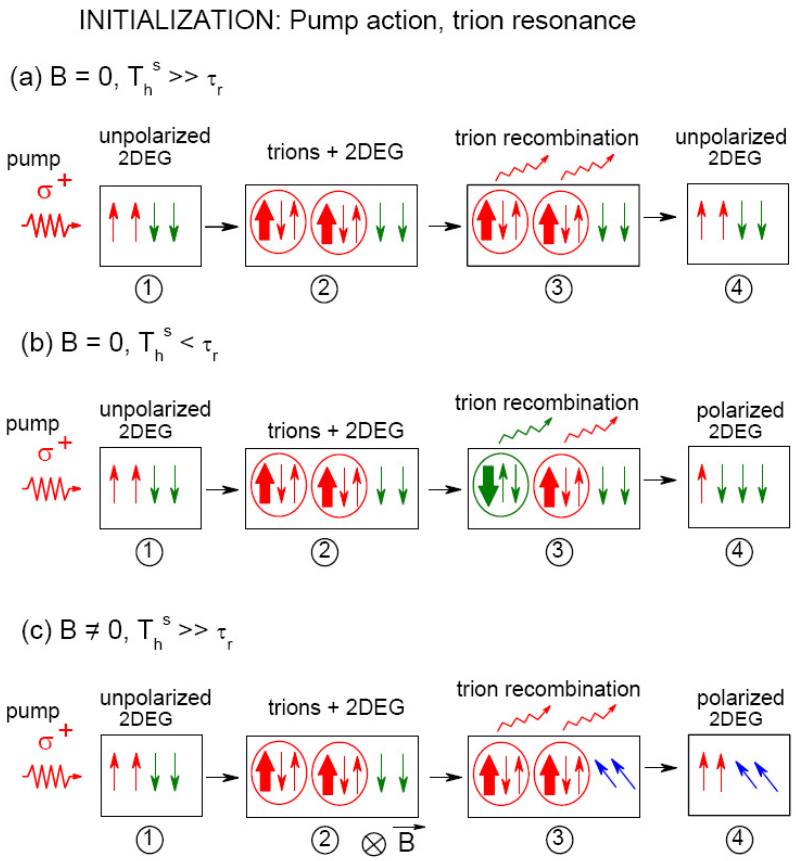

Figure 5.6: Spin orientation of resident electrons denoted as 2DEG (two-dimensional electron gas) for trion resonant excitation. The following four stages are shown: (1) unpolarized 2DEG before excitation; (2) result of action of a σ^+-polarized pump pulse, part of the resident electrons are bound to trions; (3) trions and resident electrons shortly before trion recombination; (4) 2DEG after trion recombination. Panels (a) and (b) show the situation for zero external magnetic field. (a) $T_s^h \gg \tau_r$, hole spin flip is absent and resident electrons stay unpolarized after trion recombination. (b) $T_s^h < \tau_r$, hole spin relaxes before trion decay and resident electrons become spin polarized. (c) Non-zero external magnetic field. Even in the absence of hole spin relaxation the resident electrons become polarized due to electron spin precession about magnetic field during trion lifetime [93].

The grey line fit for the exciton in Fig. 5.5(c), results from two signals shown separately in Figs. 5.5(d) and 5.5(e). These two contributions have not only different shapes but also slightly different electron g-factors and spreads of g-factors, as given in the figure caption. The variation of g-factors can be traced to its energy dependence [76]. The weaker localized carriers, which have a stronger impact on the exciton resonance, have a smaller g-factor and a smaller dispersion.

It is worth mentioning that for exciton resonant excitation higher energy trions can be formed as compared to the case of trion resonant excitation. These trions can be weaker localized so that they demonstrate short hole spin relaxation times,

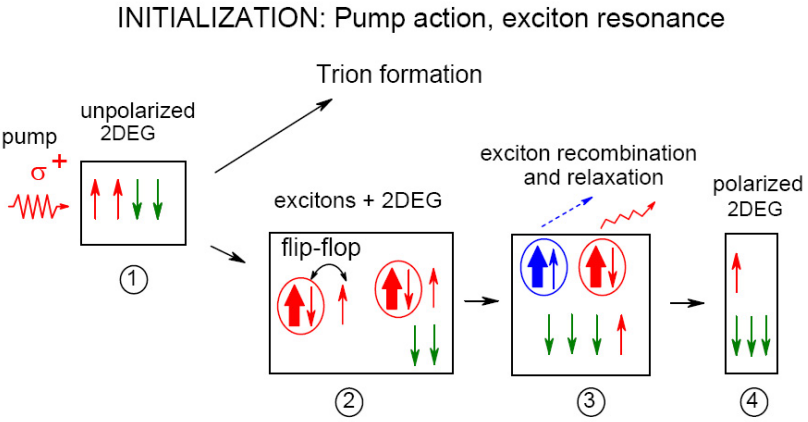

Figure 5.7: Spin orientation of resident electrons at exciton resonant excitation. Two possible scenarios are depicted: trion formation from the photocreated exciton and flip-flop scattering of an exciton with a resident electron. In this case the exciton is transformed into ta dark state and the resident electrons become polarized after the dark state has decayed (shown by blue dashed arrow) [93].

resulting in efficient spin coherence generation for resident electrons at $B = 0$. The contribution of such a channel can be described by the conventional RSA shape shown in Fig. 5.5(d). However, in the studied sample the role of the exciton under these experimental conditions dominated over the possible trion contribution. There are two arguments for this conclusion: (i) the spectral dependence of amplitude of the RSA signal with usual shape [Fig. 5.5(d)] has maximum at exciton pumping and (ii) this amplitude increases with increasing of pump power and disappears with decrease of pump power. It allows us to conclude that the main contribution to the RSA signal with shape shown in Fig. 5.5(d) is due to electron spins polarized by electron-exciton scattering or due to fast spin relaxation of hole in the resonantly excited exciton.

5.3 Low temperature spin dynamics

We turn now to the evolution of the spin dynamics of electrons and holes and in particular to the mechanisms providing carrier spin relaxation at extremely low temperatures down to 430 mK. Compare to the previous measurements, here we present results of the measurements using cryostat with ^{3}He inset (see chapter 2 for details), which allows to measure Faraday rotation and RSA signals at millikelvin temperatures. The sample was then in contact with ^{3}He in the inset, whose temperature could be changed between 0.3 and 100 K. Windows on the ^{3}He inset allow direct optical access to the sample. We tried to minimize the laser power as much as possible using this milliKelvin inserts in order to avoid overheating of the sample.

We focus here also on the Faraday rotation RSA signals measured at the trion resonance, where the hole spin dynamics is most pronounced. Figure 5.8 shows RSA signals measured at the trion resonance energy for various temperatures. We fit the

experimental RSA spectra from Fig. 5.8 by Eq. (2.14) and get very good agreement in all cases. The g-factors and spin relaxation times determined in that way are given in the figure caption. The electron and hole spin relaxation times measured at different

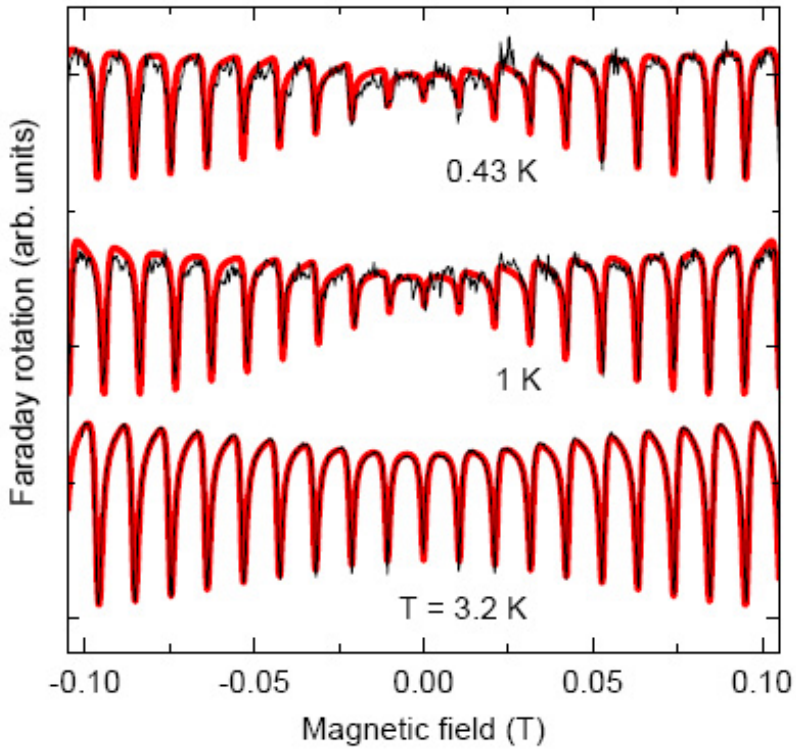

Figure 5.8: RSA signals measured for $In_{0.09}Ga_{0.91}As/GaAs$ QWs of the sample #11708 by degenerate pump-probe Faraday rotation at the trion resonance for various temperatures. Black curves are experimental data and thick red curves are fits by Eq. (2.14). Calculation parameters are: $|g_e| = 0.555$, $T_s^e = 45$ ns, for $T = 0.43$ K: $T_s^h = 2$ ns, $\tau_r = 200$ ps; for $T = 1$ K: $T_s^h = 2$ ns, $\tau_r = 200$ ps; for $T = 3.2$ K: $T_s^h = 0.6$ ns, $\tau_r = 120$ ps.

temperatures are collected in Fig. 5.9. The data for temperatures below 15 K were determined from RSA spectra and for higher temperatures, at which the RSA signals vanish, we fit the decay of the FR signals at positive delays. The data in the temperature range 0.4-10 K have been measured using the ^{3}He insert, and in the temperature range 1.6-80 K in a ^{4}He insert. The two temperature ranges were chosen to have overlap, in order to confirm consistency of the data. The temperature dependencies of spin relaxation times for electrons and holes are qualitatively similar. The times almost do not change at very low temperatures, which shows that the spin dynamics in these regimes are controlled by temperature independent mechanisms. At elevated temperatures the times drop by more than an order of magnitude. As can be seen from the solid lines in Fig. 5.9 these behaviors can be well fitted by the following function describing thermal activation from the ground state with a long relaxation time to an

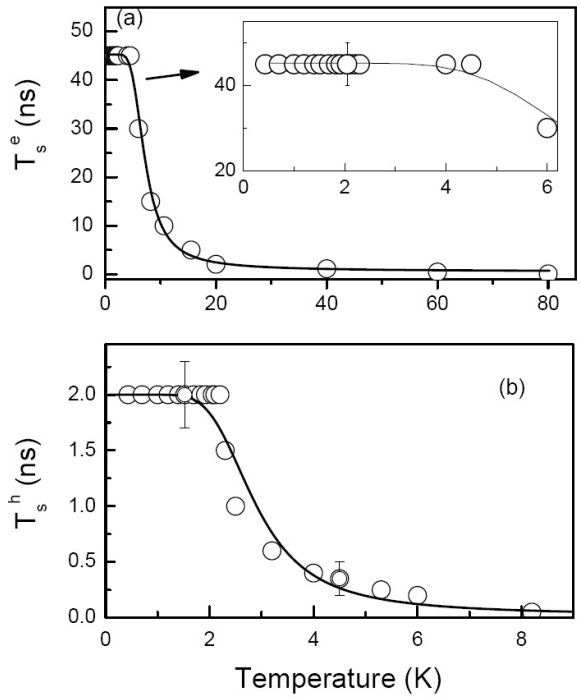

Figure 5.9: Temperature dependencies of electron (a) and hole (b) spin relaxation times in $In_{0.09}Ga_{0.91}As/GaAs$ QW of the sample #11708. Symbols are experimental data and lines are fits with Eq. (5.6) using the following parameters: $T_0^e = 45$ ns, $T_{exc}^e = 0.5$ ns and $\Delta E_e = 3$ meV for electrons in panel (a), and $T_0^h = 2$ ns, $T_{exc}^h = 10$ ps and $\Delta E_h = 1.4$ meV for holes in panel (b).

excited state with a shorter relaxation time:

$$\frac{1}{T_s^{e(h)}} = \frac{1}{T_0^{e(h)}} + \frac{1}{T_{exc}^{e(h)}} \exp\left(-\frac{\Delta E_{e(h)}}{k_B T}\right). \tag{5.6}$$

Here $T_0^{e(h)}$ are the spin relaxation times in the electron (hole) ground states, $T_{exc}^{e(h)}$ are constants characterizing the transitions between the ground and excited states which depend on the electron-phonon interaction, $\Delta E_{e(h)}$ are the characteristic activation energies, and k_B is the Boltzmann constant. One should note that this approach is rather simplified and gives physically feasible values of the fitting parameters for a relatively narrow temperature range. Therefore, it should be valid for holes in a temperature range not exceeding 8 K, while for electrons, for which experimental data have been recorded up to 80 K, additional mechanisms may cause the temperature dependencies of T_{exc}^e and ΔE_e so that more elaborated approach may be required.

The electron spin relaxation time, T_s^e, is constant in the temperature range from 0.43 to 4.5 K at an extremely large value of 45 ns, see insert in Fig. 5.9(a). At these temperatures the resident electrons are localized and their spin relaxation is provided by the hyperfine interaction with the nuclei spins, which is almost temperature independent. At temperatures above 5 K the resident electrons are thermally activated and the Dyakonov-Perel relaxation mechanism [16] which is very efficient for free electrons

starts to act. As a result the relaxation time drops to 1.1 ns at 40 K and further down to 110 ps at 80 K. Such a behavior is typical for n-doped QWs with a diluted concentration of the resident electrons [28, 54, 36].

Let us turn now to the temperature dependence of the hole spin relaxation time, T_s^h, in Fig. 5.9(b). Below 2.2 K T_s^h saturates at a value of 2 ns. At the moment it is not clear to us what relaxation mechanism is controlling the hole spin dynamics in the range from 0.43-2.2 K. Most probably it is due to the admixture of the light-hole to the heavy-hole states, enhancing strongly the possibility for spin-flip scattering.

The hyperfine interaction with the nuclei is significantly weaker for the holes than for the electrons. This has been confirmed by the recent report on ultralong hole spin relaxation with about 70 ns relaxation time, measured in the range from 0.4-1.2 K for a p-doped 4-nm GaAs/$Al_{0.3}Ga_{0.7}$As QW [77]. Our experimental situation differs from the one in p-doped samples with resident holes, as in n-doped samples we detect the spin dynamics of photogenerated holes bound in negatively charged trions. However, in the trion ground state, which is a singlet state, the two electrons have antiparallel spin orientations and flip-flop electron-hole process are not possible without exciting the trion complex into a triplet state, which requires an energy similar to the trion binding energy of 1.4 meV. In fact this energy is in very good agreement with the activation energy $\Delta E_h = 1.4$ meV, which has been obtained from fitting the experimental data in Fig. 5.9(b) by Eq. (5.6). Therefore we suggest that the strong decrease of the hole spin relaxation time at temperatures above 2.2 K is either due to trion thermal dissociation, which excites the hole into the continuum of free states with a strong spin-orbit interaction leading to a fast spin relaxation, or due to flip-flop process involving the trion triplet state.

5.4 Summary

Carrier spin dynamics in an n-doped (In,Ga)As/GaAs QW has been studied by the resonant spin amplification technique at very low lattice temperatures down to 0.43 K. In order to achieve such low temperatures, the pump-probe setup was modified by ^{3}He inset. The RSA signal carries not only information on the electron spin relaxation but also on its generation, from which one can obtain information on the hole spin relaxation. This allows us to measure hole spin relaxation times exceeding by orders of magnitude their lifetimes. Carrier localization leads to a saturation of the spin relaxation times at 45 ns for electrons below 4.5 K and at 2 ns for holes below 2.3 K. Also the spectral dependencies of the Faraday rotation and ellipticity signals have been studied experimentally around the trion and exciton resonances. The mechanisms responsible for spin polarization of the resident electrons under resonant pumping into the trion and exciton resonances have been discussed.

Chapter 6

Optical control of electron spin coherence in CdTe/(Cd,Mg)Te quantum wells

One of the most important requirements in studying of the semiconductors, is a possibility to control the electron spin by non-magnetic means and to proceed at high operation frequencies approaching pico- and femtosecond time domain [16, 87, 37]. Optical methods such as the pump-probe technique allows to study the optical orientation of electron spins, generation and control of the electron spin coherence in semiconductors. The main idea and its work principe are detailed explained in the Chapter 2.

In this chapter are presented experimentally and theoretically results of the studying of the coherent spin dynamics in n-doped CdTe/(Cd,Mg)Te quantum well structure with a help of such method. But in contrast to previous pump-probe measurements, we used here additional control pulse, which comes from he second laser and time delayed to the pump-pulse. Such control pulse induces amplitude and phase modification of the electron spin beats signal in external magnetic field, depending on the pump-control delay and polarization of the control. We experimentally separate additive and non-additive contributions to these modifications and give theoretical explanation using theoretical model considering two-level electron-trion system. Surprisingly, also the linearly polarized control induces very efficient suppression of the electron spin coherence, while the excitation with the linearly polarized pulses does not lead to any spin polarization as a rule. The developed quantitative theory allows us to explain these experimental data and to reach good quantitative agreement.

6.1 Experimental method and discussion

The electron spin coherence in CdTe/(Cd,Mn)Te quantum wells with a low dense electron gas is observed. The spin coherence was generated by the resonant excitation into the negatively charged exciton (trion) resonance.

The studied CdTe/$Cd_{0.78}Mg_{0.22}$Te QW heterostructure (sample 031901D) was grown by molecular-beam epitaxy on a (100)-oriented GaAs substrate followed by a 2 μm CdTe buffer layer. The sample has electron density about $n_e = 1.1 \times 10^{10}$ cm^{-2}. The other properties of the sample are given in the chapter 2.4. Photoluminescence (PL) and reflectivity spectra of the studied QW structure are shown in Fig. 6.1(b). The heavy-hole exciton (X) and negatively charged trion (T) resonances are clearly seen as minima in the reflectivity spectrum and as lines in the PL spectrum. They are separated by 2 meV, which corresponds to the trion binding energy [91, 85]. The broadening of these lines is mainly due to exciton and trion localization on QW width fluctuations. From the relative oscillator strengths of the exciton and trion resonances in the reflectivity spectrum we evaluate the resident electron concentration in the QW as $n_e = 2 \times 10^{10}$ cm^{-2} using the method described in Ref. [92]. For the study the co-

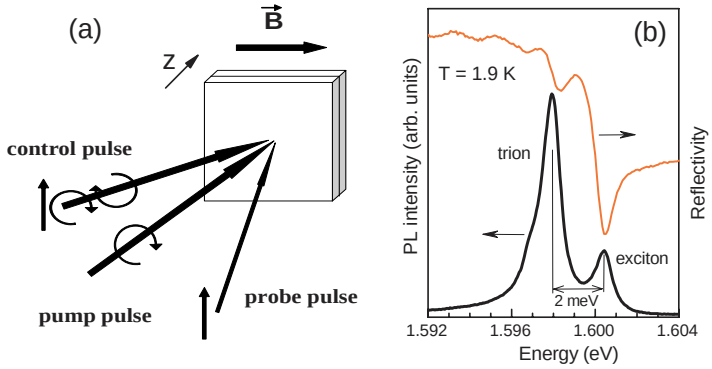

Figure 6.1: (**a**) Scheme of the three-pulse time-resolved Kerr rotation experiment. (**b**) Photoluminescence and reflectivity spectra of a 20-nm-thick CdTe/$Cd_{0.78}Mg_{0.22}$Te QW. PL was measured under nonresonant *cw* excitation with photon energy of 2.33 eV [85].

herent spin dynamics of resident electrons [34] and measurement of the Kerr rotation signal, the pump-probe setup was modified through additional control pulse from the second laser. The schema of such three-pulses experiment is displayed in the figure 6.1a. The electron spin coherence was excited by the pump and control pulses, for which different polarization configurations were used: The control was either co- or cross-circularly polarized with respect to the pump of fixed circular σ^+ polarization, or it was linearly polarized.The time delay between pump and probe pulses could be varied up to 7 ns by a mechanical delay line. A second delay line was used to set a fixed delay of the control pulse relative to the pump pulse. This delay could be changed up to $t_{pc} \leq 2$ ns in order to tune the phases of the spin coherences initiated pump and control with respect to each other. Two protocols of pump and control beam modulation were used. First we present experiments, where the signals are mainly given by the additive effect of the pump and control actions. Here both pump beam and control beam were modulated by a chopper at a frequency of 1 kHz, so that the detected Kerr rotation signal reflects the effect of both beams. In order to study the "non-additive" effect of the control on the pump induced signal we used a protocol in which only pump beam was modulated. It was sent through a photoelastic modulator operated at 50 kHz frequency so that the polarization was modulated between σ^+ and σ^-. The polarization

of the control beam was constant in time. The Kerr rotation signal was detected at the pump modulation frequency of 50 kHz, which allows us to suppress the additive contribution to the electron spin polarization induced by the non-modulated control beam. These results are reported in Sec. 6.4. Typical Kerr rotation signal measured by

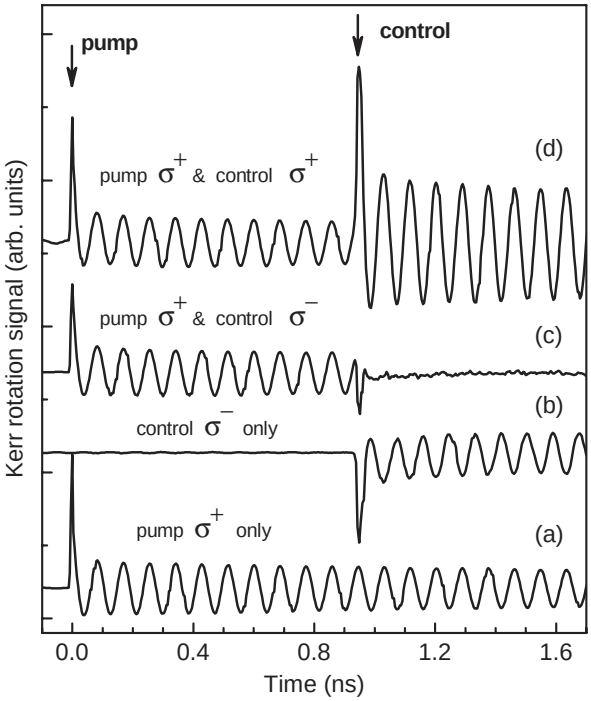

Figure 6.2: Kerr rotation signals measured by degenerate pump-probe resonant with the trion energy: (**a**) Only pump pulse with σ^+ polarization and density of 0.3 W/cm^2. Evaluated $T_2^* = 4.2$ ns. (**b**) Only control pulse with σ^- polarization and density of 0.3 W/cm^2. (**c**) σ^+ pump pulse and σ^- control pulse joint excitation. (**d**) σ^+ pump pulse and σ^+ control pulse joint excitation. $B = 0.5$ T, $T = 1.9$ K. For (**b**), (**c**) and (**d**) $t_{pc} = 0.96$ ns and $\varphi = 0$ [85].

the pump-probe technique at a magnetic field of 0.5 T is shown in Fig. 6.2 by a curve (a). The σ^+ circularly polarized pump pulses arrive at the sample at a zero time delay and induce coherent spin precession of the resident electrons about an external magnetic field. It is monitored by a periodically oscillating Kerr signal amplitude $K(t)$. The oscillation period corresponds to the electron Larmor frequency $\omega_e = \mu_B g_e B/\hbar$ with $|g_e| = 1.64$, which is in good agreement with the literature data [88]. This value was received from the fit of the experimental data by a single exponential decaying function [16]

$$K(t) = A \ \exp\left(-\frac{t}{T_2^*}\right)\cos(\omega_e t). \tag{6.1}$$

Here A is a constant corresponding to the signal amplitude, T_2^* is a dephasing time responsible to the signal decay. The evaluated dephasing time $T_2^* = 4.2$ ns is considerably longer than the trion recombination times being in the range 30-100 ps in CdTe-based QWs [34], which allows us to ascribe the Kerr signal to the resident elec-

trons. Here we start with describing of the effect of control pulses delayed by a time t_{pc} from pump pulses on the electron spin coherence generated by the pump. Modifications induced by the control pulses depend critically on a reduced phase φ at which the control hit the electron spin coherence excited by the pump. The reduced phase is defined as $\omega_e t_{pc} = \varphi + 2\pi N$, where N is an integer number corresponding to the number of full spin precession periods during the pump-control delay and $0 \leqslant \varphi < 2\pi$. We start with the pump-probe experiments where the circularly polarized control has been used. We also focus here on the signal amplitude modifications induced by the control, the changes of its phase are discussed in the next section Sec. 6.1.2. To that end we adjust the delay t_{pc} in order to achieve a phase $\varphi = 0$, when Kerr signal amplitude $K(t)$ has its maximum value. At a magnetic field of 0.5 T this condition is fulfilled, e.g. for $t_{pc} = 0.96$ ns, as one can see from Fig. 6.2 by comparing curves (a) and (b). For co-polarized pump and control pulses (both are σ^+) of the same power the Kerr signal is enhanced about twice after the control action, see curve (d). This is very expectable result, as in this case electron spin polarization generated by the control has the same orientation as the one generated by the pump and processing few full precessions. Cross-polarization of the pump (σ^+) and control (σ^-) pulses leads to the full suppression of the electron spin precession, as it is shown by curve (c). In this case electron polarizations generated by the pump and control are antiparallel to each other and compensate one another. It is important, that for the low excitation density regime presented in Fig. 6.2 only a small part of the resident electrons is affected either by pump or control pulses. In this case the effect of the joint action of the pump and control can be described in terms that each of them generate spin coherence for two independent subensembles of the resident electrons. The experimentally measured Kerr rotation signal results from their additive contributions, which are either add or subtract from each other. The very similar behavior has been previously reported for the Mn spin coherence in (Cd,Mn)Te/(Cd,Mg)Te QWs [89].

6.1.1 Effect of circularly polarized control on signal amplitude

Detailed results for the effect of control power on the Kerr signal amplitude for co- and cross-polarizations of pump and control are given in Fig. 6.3. The phase for control pulse arrival was chosen to be $\varphi = 0$, as in Fig. 6.2. Therefore, the spin polarizations induced by the pump ($\mathbf{S}_{pump}$) and the control ($\mathbf{S}_{control}$) are either parallel or antiparallel to each other for co- and cross-polarizations, respectively. The resultant polarization ($\mathbf{S}_{total}$) along the z-axis is reduced or increased, as shown schematically in the corresponding panels of Fig. 6.3. The Kerr amplitude increases for the co-polarized configuration shown in panel (a), in line with the intuitive expectations. It decreases for the cross-polarized case given in panel (b), crosses the zero level when the control power becomes about equal to the pump power and then shows increasing negative values. These dependencies can be seen in detail in Fig. 6.4, where the dependence of the Kerr amplitude on control power is plotted. To determine the spin beat amplitudes the signals after the control pulse arrival were fitted by Eq. (6.1). Triangles and circles give the experimental data for co- and cross-polarized pump and control pulses, respectively. The lines in Fig. 6.4 show the theoretical calculations obtained from Eq. (6.14) using

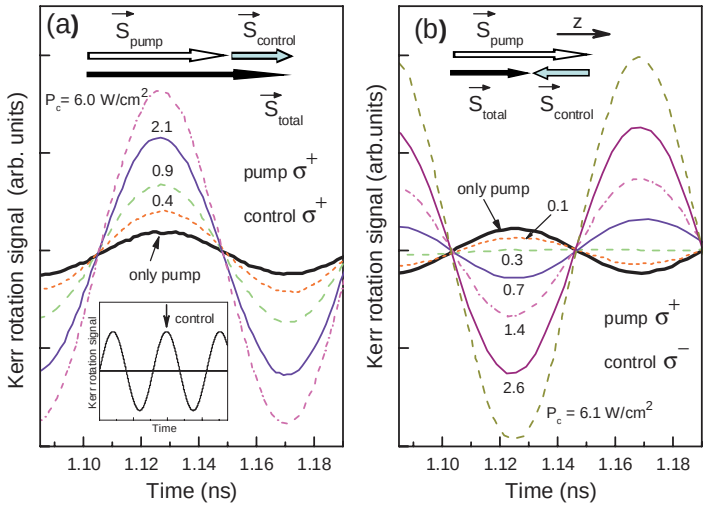

Figure 6.3: Kerr rotation signals measured for various control pulse power (P_c) at $B = 0.5$ T. Pump is σ^+ polarized and has power of $P_p = 0.3$ W/cm^2: (**a**) σ^+ control pulses; (**b**) σ^- control pulses. In insert arrow marks the time moment of the control pulse at $t_{pc} = 0.87$ ns, which corresponds to $\varphi = 0$. Arrows in the panels shows schematically contributions to the electron spin polarizations induced by the pump ($\mathbf{S}_{pump}$), control ($\mathbf{S}_{control}$) and result of their joint action ($\mathbf{S}_{total}$) [85].

the relation between the pulse area and control power Eq. (6.21) with the same value of $C = 0.63$ W/cm^2 as in Fig. 6.10. Good agreement between the experimental data and theoretical curves is seen. Figure 6.4 shows that for co-polarization the amplitude of the signal saturates faster than for cross-polarization. This is reasonable, because the spin projection of a single electron is limited by 1/2. Therefore, in co-polarization the spin should saturate faster because spin with projection of the same sign is added and, therefore, the spin reaches the maximum value faster. A more detailed theoretical explanation will be given in Sec. 6.5.

6.1.2 Effect of circularly polarized control on signal phase

When the control pulse acts on the pump induced polarization at an arbitrary phase φ, not only the amplitude of the Kerr rotation signal changes, but also the phase will be shifted by an angle θ after the control pulse arrival. Corresponding experimental data are shown in Fig. 6.5(a), where we chose cross-polarization for pump and control and $\varphi = \pi/2$. The insert in Fig. 6.5(b) shows schematically that for these experimental conditions the signal after the control pulse is expected to show a negative phase shift, i.e. to shift to earlier delays. The signal after control pulse arrival can be described by Eq. (6.1) when replacing $\cos(\omega_e t)$ by $\cos(\omega_e t + \theta)$:

$$K(t) = A \exp\left(-\frac{t}{T_2^*}\right)\cos(\omega_e t + \theta). \tag{6.2}$$

In the case, when the control pulse acts on the pump induced polarization at an arbitrary phase φ, not only the amplitude of the Kerr rotation signal will be changed,

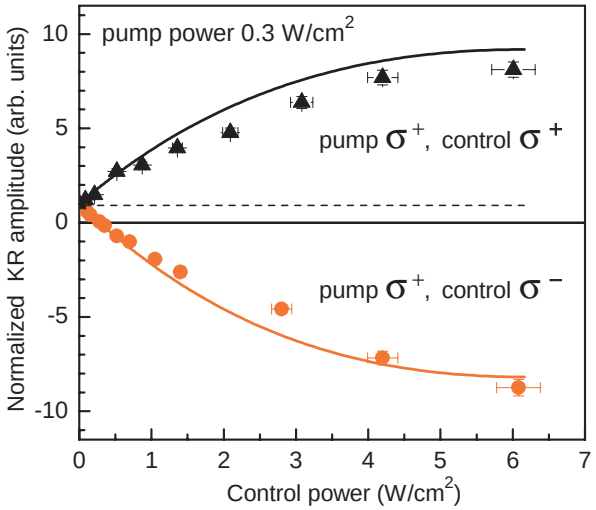

Figure 6.4: Amplitude of Kerr rotation signal as a function of control power. The amplitude is taken after a time moment of control pulse arriving for co- and cross-polarizations of pump and control: triangles - pump σ^+ and control σ^+ (regime of amplification); circles - pump σ^+ and control σ^- (regime of suppression). $B = 0.5$ T, $t_{pc} = 0.87$ ns, and $\varphi = 0$. Solid lines show calculated amplitudes of the signals according to Eq. (6.14) [85].

but also its phase after the control pulse arrival will be shifted by an angle θ. Experimental appearances of such behavior are shown in Fig. 6.5(a), where we chose cross-polarizations for pump and control and $\varphi = \pi/2$. In the insert of Fig. 6.5(b) is schematically shown that for these experimental conditions the signal after the control pulse arrival is expected to have a negative phase shift, i.e. to shift to earlier delays. The signal after control pulse arrival can be described by Eq. (6.1) when replacing $\cos(\omega_e t)$ by $\cos(\omega_e t + \theta)$:

$$K(t) = A \exp\left(-\frac{t}{T_2^*}\right)\cos(\omega_e t + \theta). \tag{6.3}$$

In agreement with our qualitative expectations, the signal phase shown in Fig. 6.5(b) by the filled circles decreases and saturates at $\theta = -\pi/2$ for control powers strongly exceeding the pump power.

The open circles in Fig. 6.5(b) show the signal phase evaluated from the experimental signal amplitudes without and with control using the simple additive model which is depicted in the insert of Fig. 6.5(a). As one can see from scheme the phase shift θ is determined in this case of perpendicular orientation of $\mathbf{S}_{pump}$ and $\mathbf{S}_{control}$ by

$$\theta = \arctan(S_{control}/S_{pump}). \tag{6.4}$$

The overall tendency of the dependencies shown by the closed and open circles is the same,however they deviate considerably from each other for control powers exceeding 0.5 W/cm^2. This fact point to the presence of some non-additive contribution of the control to the spin coherence generated by the pump which we will discuss in detail

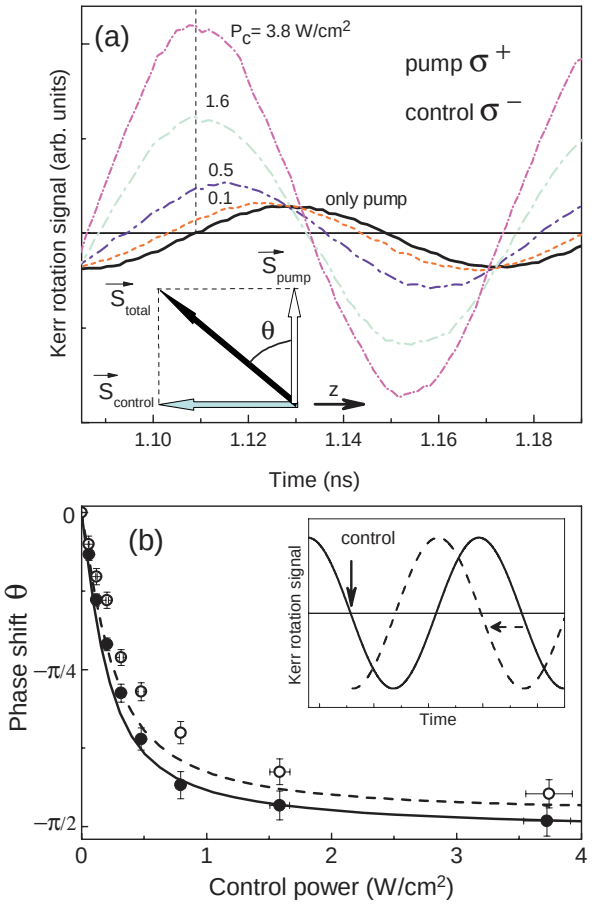

Figure 6.5: (**a**) Kerr rotation signals measured at different control powers (P_c): pump (σ^+, 0.15 W/cm^2), control (σ^-). Insert shows schematics of the generated electron spin polarizations. $B = 0.5$ T, $t_{pc} = 0.87$ ns, and $\varphi = \pi/2$. (**b**) The phase shift of Kerr rotation signal as a function of control power. Closed circles show phase shift determined from fitting of experimental data using Eq. (6.3). Open circles show the values calculated from the experimental data using the model of spins composition given by Eq. (6.4). Lines show the phase of spin beats calculated from the microscopic model (solid line) and within the additive model (dashed lines). Inset shows schematically the modification of the signal induced by the pump pulses (solid line) by the control pulses arrived at $\varphi = \pi/2$ and inducing phase shift of the resultant signal (dashed line) [85].

below. The results in Fig. 6.6 have been collected to confirm the conclusion drawn from the data in Fig. 6.5, that the phase shift of the Kerr rotation signal is mainly controlled by the ratio of the pump and control generated spin polarizations, $S_{control}/S_{pump}$. An increase of the control power for constant pump power causes a shift of the signal to earlier times, compare curves 1 and 2. This corresponds to an increase of the phase shift value, as shown by the left diagram. In turn, a pump power increase for constant control power (curves 2 and 3 and the right diagram) induces a signal shift to later times. For the chosen power densities these transformations are dominated by the

additive mechanism.

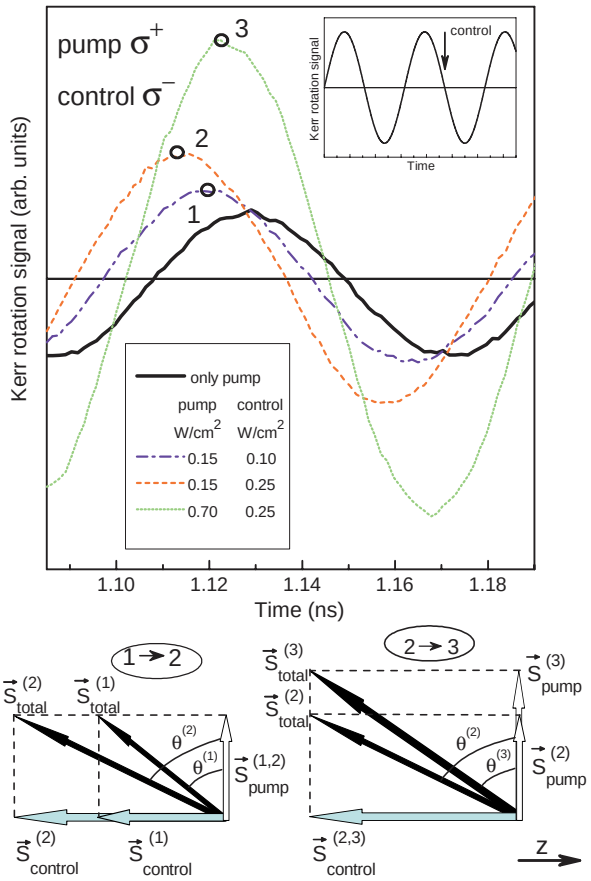

Figure 6.6: Kerr rotation signals measured at different pump (σ^+) and control (σ^-) powers. $B = 0.5$ T, $t_{pc} = 0.87$ ns, and $\varphi = \pi/2$. Inset illustrates the control pulse arrival time moment (arrow) in respect to the KR signal generated by the pump. Two bottom diagrams explains changes in the phase shift θ of the KR signal [85].

6.1.3 Effect of linearly polarized control

In our experimental geometry it is not expected that linearly polarized light would induce any spin polarization of the resident electrons. Indeed, we did not find any signal for a linearly polarized pump. However, we observed that the electron spin polarization induced by a circularly polarized pump is strongly sensitive to a linearly polarized control. One can see in Fig. 6.7 that irrespective of the delay t_{pc} the Kerr rotation signal is suppressed by a linearly polarized control. The suppression effect increases for higher control powers as shown in the insert. One should note that this effect changes only the signal amplitude but does not induce any phase shift θ, independently of t_{pc}. The suppression is clearly a non-additive effect: generation of spin coherence by the control pulse is absent, but the signal is still modified. These, at first glance, surprising experimental findings can be explained by the qualitative model presented in the following section.

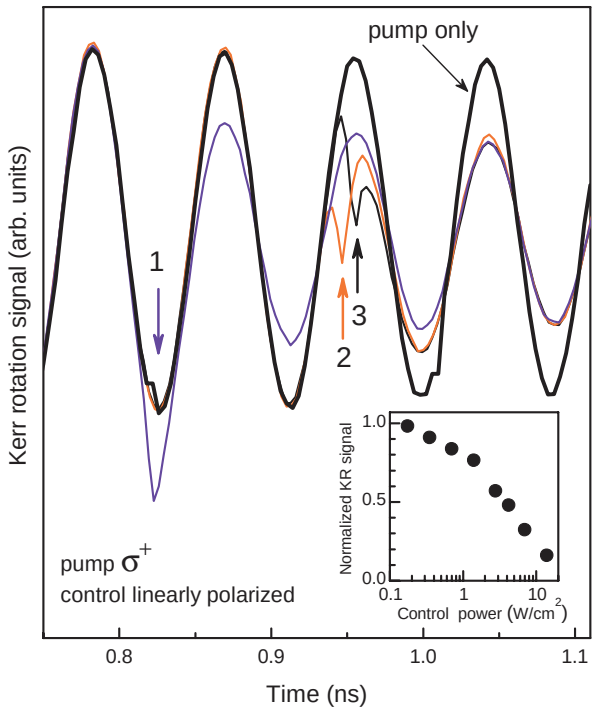

Figure 6.7: Kerr rotation signals measured at different time moments of control pulse arriving (indicated by arrows) for σ^+ polarized pump with $P_p = 2.2$ W/cm^2 and linearly polarized control with $P_c = 2.2$ W/cm^2. $B = 0.5$ T. Arrival times of the control pulses are shown by arrows: (1) $t_{pc} = 0.82$ ns, and $\varphi = \pi$; (2) $t_{pc} = 0.95$ ns, and $\varphi = 1.8\pi$; and (3) $t_{pc} = 0.96$ ns, and $\varphi = 0$. Insert illustrates suppression of the KR signal amplitude with increasing control power. The amplitude is normalized to its value without control [85].

6.2 Qualitative model consideration of linearly polarized control action

The theoretical explanations and qualitative model of presented experimental results in this chapter were developed by M.Glazov Ref. [34].

In order to develop a qualitative picture of the spin depolarization by the linearly polarized control it has been considered the simple model of a spin ensemble described in Ref. [34]. The linearly polarized pulse can be represented as a superposition of two circularly polarized ones and assume that at the hit time of the control pulse there are n_+ electrons with spin z-component $1/2$ and n_- electrons with spin z-component $-1/2$. We assume that the control pulse arrives at the maximum ($\varphi = 0$) or the minimum ($\varphi = \pi$) of the pump-induced spin beats,in other words there are no in-plane spin components at the moment of control pulse arrival. The absorption of the σ^+ component of the linearly polarized light generates n_+W singlet trions by exciting the same number of $s_z = +1/2$ resident electrons. Here W is the probability of singlet trion formation per electron due to control pulse action. Analogously, the σ^- component of

the linearly polarized light generates $n_- W$ singlet trions by exciting the same number of $s_z = -1/2$ electrons. Provided the hole spin-flip time is much shorter than the trion radiative lifetime the electrons bound to trions are left unpolarized after trion recombination. Therefore, the total spin of the ensemble is decreased by

$$\delta S_z = S_z^{(a)} - S_z^{(b)} = -\frac{n_+ - n_-}{2} W = -S_z^{(b)} W. \tag{6.5}$$

Here the superscripts (a) and (b) correspond to the spin z- component after and before the control pulse arrival, respectively. The z projection of the total spin of the electron ensemble after control pulse arrival is given by

$$S_z^{(a)} = (1 - W) S_z^{(b)}. \tag{6.6}$$

Clearly, the probability of singlet trion formation is $0 \leq W \leq 1$ so that the electron spin after the control pulse is smaller than the spin before the pulse. It follows therefore that the linearly polarized pump acts as a depolarizer.

6.3 Quantitative theory

The quantitative theory of spin manipulation by a control pulse is developed following the methods described in Ref. [90]. The electric field of the control pulse can be written as

$$\boldsymbol{E}(\boldsymbol{r}, t) = E_{\sigma^+}(\boldsymbol{r}, t)\boldsymbol{o}_+ + E_{\sigma^-}(\boldsymbol{r}, t)\boldsymbol{o}_- + \text{c.c.}\,, \tag{6.7}$$

where $\boldsymbol{o}_\pm$ are the circularly polarized unit vectors related to the unit vectors $\boldsymbol{o}_x \parallel x$ and $\boldsymbol{o}_y \parallel y$ by $\boldsymbol{o}_\pm = (\boldsymbol{o}_x \pm \mathrm{i}\boldsymbol{o}_y)/\sqrt{2}$. Here the components E_{σ^+} and E_{σ^-} are proportional to the product of the exponential function $\exp(-\mathrm{i}\omega_\mathrm{C} t)$ with ω_C being the control pulse optical frequency and a smooth envelope. The incident electromagnetic field induces optical transitions between the electron state and the trion state, creating a coherent superposition of them. In accordance with the selection rules σ^+ circularly polarized light creates a superposition of the $+1/2$ electron and $+3/2$ trion states, while σ^- polarized light creates a superposition of the $-1/2$ electron and $-3/2$ trion states. In order to describe these superpositions it is convenient to introduce a four component wavefunction

$$\Psi = \left(\psi_{1/2}, \psi_{-1/2}, \psi_{3/2}, \psi_{-3/2}\right)\,, \tag{6.8}$$

where the $\pm 1/2$ subscripts denote the electron spin projection and $\pm 3/2$ refer to the spin projection of the hole in the trion. The electron spin polarization is expressed in terms of $\psi_{\pm 1/2}$ as follows

$$\begin{aligned} S_z &= \left(|\psi_{1/2}|^2 - |\psi_{-1/2}|^2\right)/2\,, \\ S_x &= \Re(\psi_{1/2}\psi^*_{-1/2})\,, \\ S_y &= -\Im(\psi_{1/2}\psi^*_{-1/2})\,. \end{aligned} \tag{6.9}$$

All excited states of the system, such as e.g. triplet trion states are neglected. In this respect the model is directly applicable to the case of a resident carrier strongly

localized in a quantum dot or quantum well imperfection. Further, it will be assumed that the delay between the pump and control pulses exceeds by far the radiative lifetime of the trion, hence, just before the control pulse arrival there is a resident electron with precessing spin but no trion. The state of the system just before the control pulse arrival corresponds to the non-zero components $|\psi_{+1/2}|^2 + |\psi_{-1/2}|^2 = 1$ and $\psi_{\pm 3/2} = 0$. Following the method in Ref. [90] and detailed description in the Ref. [34], one may reduce the Schroedinger equation for the four-component wave function to two independent differential equations for $\psi_{\pm 1/2}(t)$ which take the following simple form

$$\ddot{\psi}_{\pm 1/2} - \left(\mathrm{i}\omega' + \frac{\dot{f}_{\pm}(t)}{f(t)} \right) \dot{\psi}_{\pm 1/2} + f_{\pm}^2(t)\psi_{\pm 1/2} = 0 \,. \tag{6.10}$$

Where $f_{\pm}(t)$ are smooth envelopes for the σ^+ and σ^- polarized components of the control pulse. $\omega' = \omega_{\mathrm{C}} - \omega_0$ is the detuning between the control pulse optical frequency and the trion resonance frequency, ω_0. Below we discuss the cases of linearly and circularly polarized control pulses.

Linearly polarized control. In case of a linearly polarized control, according quantum-mechanical calculations detailed presented in Ref. [85], one gets equation

$$Q_l^2 = 1 - \frac{\sin^2(\Theta_l/2)}{\cosh^2(\pi y)}, \tag{6.11}$$

where $\Theta_l = 2\mu\tau_p/\sqrt{2}$ is the effective area of each circularly polarized component of the control pulse $y = \omega'\tau_p/(2\pi)$. The constants Q_l describes the transformation of the wavefunction under action of the linearly polarized pulse. Using the definitions of the spin components, Eqs. (6.9) and solution of the equation (6.10), one can readily obtain that the spin vector of an electron after the control pulse, $\boldsymbol{S}^{(a)}$, is connected with the electron spin vector before the control pulse arrival, $\boldsymbol{S}^{(b)}$, by

$$\boldsymbol{S}^{(a)} = Q_l^2 \boldsymbol{S}^{(b)}, \tag{6.12}$$

i.e. the spin vector before the control pulse is simply multiplied by some nonnegative quantity $Q_l^2 \leqslant 1$. If the electron is left behind unpolarized after trion decay, i.e. when the trion lifetime is longer than the hole spin relaxation time, then the total spin of the electron ensemble is decreased, in agreement with the simplified Eq. (6.6) obtained from qualitative arguments. In the case of small control power effective pulse area $\Theta_l \ll 1$, and for negligible detuning between the control pulse and the trion resonant frequency, $y \ll 1$, one can represent Q_l^2 in Eq. (6.11) as

$$Q_l^2 \approx 1 - \frac{(\mu\tau_p)^2}{2}. \tag{6.13}$$

Circularly polarized control. Now we turn to the case of circularly polarized control pulses. According Ref. [90] we obtain the following expressions for the spin

components before and after control pulse arrival:

$$S_z^{(a)} = \mp\frac{1-Q_c^2}{4} + \frac{Q_c^2+1}{2}S_z^{(b)}, \tag{6.14}$$

$$S_x^{(a)} = Q_c\cos\Phi_c S_x^{(b)} \pm Q_c\sin\Phi_c S_y^{(b)}, \tag{6.15}$$

$$S_y^{(a)} = Q_c\cos\Phi_c S_y^{(b)} \mp Q_c\sin\Phi_c S_x^{(b)}. \tag{6.16}$$

Here the upper signs of $\mp$ and $\pm$ correspond to a σ^+ polarized control and the lower signs to a σ^- polarized control. The constant Q_c is given by

$$Q_c^2 = 1 - \frac{\sin^2(\Theta_c/2)}{\cosh^2(\pi y)},$$

where $\Theta_c = \sqrt{2}\Theta_l = 2\mu\tau_p$. For small pulse areas $\Theta_c \ll 1$ and $y \ll 1$

$$Q_c^2 \approx 1 - (\mu\tau_p)^2. \tag{6.17}$$

One can see from Eq. (6.14) that there are two contributions to the spin z component of an electron after circularly polarized control pulse arrival. The first contribution is an additive one: it changes its sign upon reversal of the circular polarization of the control pulse and it does not depend on the spin state before control pulse arrival. For weak control power, $\mu\tau_p \ll 1$, and negligible detuning, $y \ll 1$, the additive part to $S_z^{(a)}$ is given by, see Eq. (6.17)

$$\mp\frac{1-Q_c^2}{4} \approx \mp\frac{(\mu\tau_p)^2}{4}. \tag{6.18}$$

This additive contribution equals exactly the spin z component created by a pump pulse of the same power. Another contribution to the electron spin after control pulse action is a non-additive one. It can be interpreted as a transformation of the electron spin by the control pulse. This contribution is given by

$$\frac{Q_c^2+1}{2}S_z^{(b)} \approx \left[1 - \frac{(\mu\tau_p)^2}{2}\right]S_z^{(b)}, \tag{6.19}$$

where the last approximate equality holds for weak control power and small detuning. This non-additive contribution is independent of the circular polarization sign and always decreases the z component of electron spin. The comparison of Eq. (6.19) with Eqs. (6.12) and (6.13) shows that for weak control powers the depolarization of the electron spin z component by circularly and linearly polarized light is the same. The in-plane spin components are also affected by the circularly and linearly polarized control pulses. The absolute value of the in-plane spin projection $S_\perp = \sqrt{S_x^2 + S_y^2}$ is decreased by the factor $Q_c \approx 1 - (\mu\tau_p)^2/2$ (the latter equality holds for weak control pulses), similar to the case of a linearly polarized control.

6.4 Non-additive contribution of control

In this section we address experimentally the question whether a circularly polarized control, similar to a linearly polarized one, can serve as a depolarizer of the induced

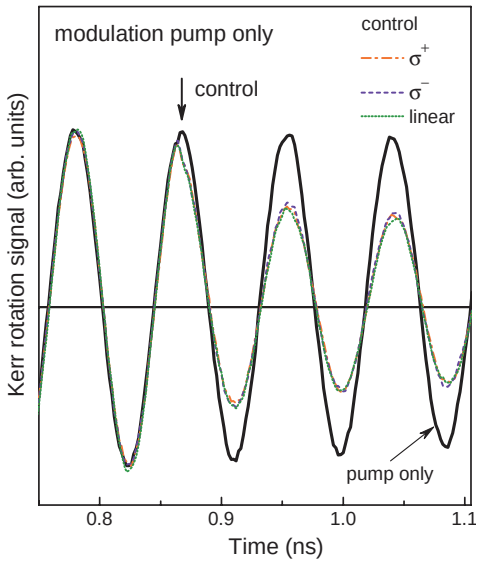

Figure 6.8: Non-additive effect on Kerr rotation signals measured at different polarizations of control (σ^+, $P_c = 3.5$ W/cm^2) in the case of the only pump beam modulation ($P_p = 0.25$ W/cm^2). Arrow indicates the time moment of control pulse arrival at $t_{pc} = 0.87$ ns, and $\varphi = 0$. $B = 0.5$ T [85].

spin coherence. This will also allow us to obtain in-depth insight into the non-additive contribution. Here are presented results of studying modifications of the pump-induced spin coherence by the control. For that purpose, one should exclude Kerr rotation signal that is directly caused by generation of electron spin polarization by the circularly polarized control. It is possible to suppress this signal by implementing the second measurement protocol described in Section 6.2. Only the pump beam is modulated in this case and lock-in detection allows us to exclude the direct contribution of the unmodulated control to the detected spin polarization. One can see in Fig. 6.8 that also a circularly polarized control decreases the Kerr rotation amplitude, similar to the case of a linearly polarized control. The magnitude of this effect is identical for σ^+ and σ^- polarization of the control and is also independent of the control delay t_{pc} (not shown). It is interesting that the suppression efficiency of the circularly polarized control is equal to the one for a linearly polarized control of the same intensity. This suggests that the responsible mechanism is the same, which is confirmed by the quantitative analysis given below. As opposed to the singlet trion, mentioned above (in the previous section), there are other possible excited states in the system, such as the triplet trion state, which can be populated by polarized light absorption. In the classical approach [34] this state can be considered as an exciton interacting with a resident electron. Due to the electron spin-flip within a triplet trion a singlet trion state can be formed. To analyze the non-additive effect of a circularly polarized control pulse for the case when the triplet trion/exciton can be photocreated, we denote the probability of singlet trion formation via an exciton [as a result of the following process: electron $-1/2$ + exciton $(-1/2,\ 3/2)$, afterwards electron spin-flip and formation of $(-1/2,\ 1/2,\ 3/2)$ or $(-1/2,\ 1/2,\ -3/2)$ trion] by $\tilde{W}$ and the probability of direct singlet trion formation

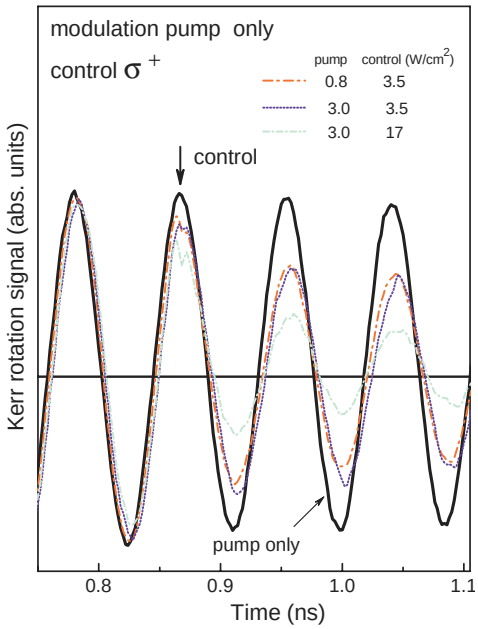

Figure 6.9: Non-additive effect on Kerr rotation signals measured at various pump and control (σ^+) powers (the case of only pump beam modulation). Signals are normalized on the pump power to simplify their comparison with each other. Thick solid line is pump only signal at $P_p = 0.25$ W/cm^2. $B = 0.5$ T, $t_{pc} = 0.87$ ns, and $\varphi = 0$ [85].

[1/2 electron + photocreated exciton (−1/2, 3/2) yields (−1/2, 1/2, 3/2) trion] as W [**?**]. Here we analyze the experimental scenario where the pump polarization is assumed to be modulated while the control is always σ^+ polarized. If the electron spin before control arrival is 1/2 the electron spin after trion recombination is $(1-W)/2$, because in this case direct singlet trion formation occurs. If the electron spin after control arrival is $-1/2$ then its spin after trion recombination is $-(1-\tilde{W})/2$, since formation of a triplet trion/exciton is required. The detected signal is suppressed compared to the case without control by the factor

$$S_z^{(a)} = \left(1 - \frac{W + \tilde{W}}{2}\right) S_z^{(b)}. \tag{6.20}$$

At high pump powers both W and $\tilde{W}$ approach unity (see Ref. [34]) and the spin after control is completely erased. Clearly, W approaches 1 faster since no electron spin-flip is needed. Therefore one can expect a kind of "two-stage" behavior of suppression: first the spin is suppressed down to the level $(1-\tilde{W})/2$ of its value before control pulse arrival, and further increase of control power yields complete suppression.

In Figure 6.9 the effect of the non-additive contribution is presented for various pump and control powers. The Kerr rotation signals are normalized to their maximum amplitudes before control pulse arrival. Two conclusions follow from these experimental data. First, the suppression efficiency increases with increase of the control power. Second, the suppression efficiency is determined by the control power only, compare

the signal amplitudes for different pump powers before and after control arrival for the same control power of 3.5 W/cm^2.

6.5 Comparison of theory and experiment

We have established experimentally and theoretically that the control pulse has, in general, a two-fold effect on the electron spin coherence in quantum wells. First, a circularly polarized control pulse generates additional spins and results in an additive contribution to the spin beats. Besides, the control pulse effects the spins that are already polarized by the pump pulse, leading to suppression of the pump-induced spin coherence. The latter effect is possible both for circularly and linearly polarized control pulses.

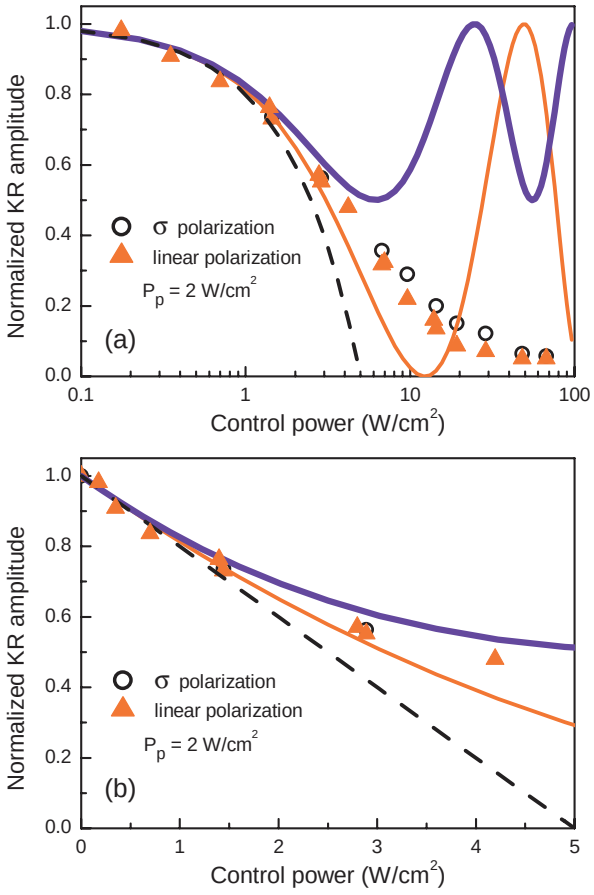

Figure 6.10: Amplitude of Kerr rotation signal after the control pulse arrival normalized to the amplitude before the control pulse arrival, $S_z^{(a)}/S_z^{(b)}$. Symbols are the experimental data measured in linear polarization of the control pulse (triangles) and in circular polarization (circles). $B = 0.5$ T and $T = 1.9$ K. Curves are theoretical calculations: suppression in linear polarization (solid red line) and in circular polarization (solid blue line). Dashed curve shows small power asymptotics [85].

As next we consider the effect of the spin coherence suppression by linearly and circularly polarized light. Figure 6.10 shows the suppression efficiency, i.e. the ratio $S_z^{(a)}/S_z^{(b)}$ as function of control pulse power for a linearly polarized control (closed circles) and a circularly polarized control (open circles). We focus on the small control power regime $P_c \leq 5$ W/cm^2 illustrated in detail in Fig. 6.10(b). In this regime the efficiency of suppression increases linearly with increasing control pulse power. Fitting the experimental data by the theoretical model, Eqs. (6.13) and (6.19), we obtain a relation between the control pulse power and its area:

$$P_c = C\Theta_l^2, \tag{6.21}$$

where $C \approx 0.63$ W/cm^2 is the fitting parameter. The theoretical curve corresponding to the limit of $\Theta_l \ll 1$ is shown by the dashed line in Fig. 6.10. The solid thick and thin lines show the suppression efficiency as function of control power for linear and circular polarizations of the control pulse, respectively. They are calculated for the whole range of experimentally used powers by Eqs. (6.13) and (6.19), using the link between the control power and its area from Eq. (6.21), see Fig. 6.10(a). The theory reproduces the experimental data well for control powers $P \leqslant 5$ W/cm^2. Fig. 6.10 shows the discrepancy between the experiment and theory for control powers $P_c \gtrsim 5{-}10$ W/cm^2. This discrepancy of the theoretical predictions and the experimental data for a circularly polarized control results from limitations of the model. We consider the optical transition from a localized electron state to a trion state within a two-level model neglecting completely other excited states such as, e.g., triplet trion states, etc. Their inclusion may result in the complete suppression of the Kerr signal due to the non-additive contribution of the circularly polarized control pulse. In addition, heating of the electron ensemble can be considerable for pump powers exceeding 5 W/cm^2 and can cause reduction of the signal both in linear and circular polarization.

6.6 Summary

We have demonstrated experimentally the possibility to manipulate the electron spins in quantum wells by means of polarized laser pulses. We have shown that the coherence of resident electrons can be increased or decreased by the circularly polarized control pulse depending on the pump/control delay and the relative polarizations of the pump and control pulses. This additive effect is a result of the spin coherence generation by the control pulse which may be summed up or subtracted from the pump-induced spin coherence.

Surprisingly, we have also found a non-additive effect of the circularly polarized control pulse. This contribution is experimentally detected by a special modulation protocol where the control pulse is not modulated while the pump pulse is modulated and the Kerr signal is detected by the lock-in technique. The measured signal is decreased by a control pulse and the suppression efficiency is determined only by the control pulse power. It is independent of the circular polarization of the control pulse and the amount of spin coherence induced by the pump.

The similar suppression is observed for the linearly polarized control pulses which do not generate any spin coherence in our geometry. The suppression efficiency is the same for the linearly and circularly polarized pulses for the relatively small control powers.

The experimental findings are well explained by the proposed theoretical model. It takes into account the formation of the singlet trion by a polarized light localized on an imperfection of an n-type quantum well. The spin of electron returning from the trion after its radiative recombination is depolarized. Since linearly polarized light results in the trion formation regardless the electron spin projection the spin coherence is suppressed. The model describes also both additive and non-additive effects of circularly polarized control pulses.

The manifestations of non-additive effects are related with considerable spin polarization generated by the pump pulse, and in general, they do not require the trion as an intermediate state in the spin coherence manipulation. The high spin polarization regime is achievable for the widely studied quantum wells with a dense electron gas. However, it takes place at much higher excitation densities where other nonlinear effects complicate the interpretation of experimental data. On the contrary, in the quantum wells with a low dense electron gas studied here the relatively high spin polarization can be reached at rather low excitation powers.

Conclusions

Nowadays the quantum information technologies are getting very important. One of the promising ways of its development is considered to date to be exploiting of the photon polarization for sharing of the quantum information and of the spin polarization of carriers for its storage. In order to storage information, one has to find appropriate structures with the high optical susceptibility and low rates of the spin relaxation. Studied in this work quantum well heterostructures fulfill condition of the high optical susceptibility. The most important thing is an understanding and recognition of spin relaxation processes causing spin relaxation in semiconductors quantum wells. This thesis contributes only a small piece of new information for solving of such research problems.

In these thesis spin dynamics of carriers in three types of heterostructures, GaAs/(Al,Ga)As,(In,Ga)As/GaAs and CdTe/(Cd,Mg)Te QWs were studied in details. The main method for study of the spin relaxation times was the Faraday/Kerr rotation technique. In Kerr/Faraday rotation experiments, the rotation angle of the polarization plane of the probe beam is proportional to the degree of circular birefringence induced by the pump beam which generates spin oriented carriers. The Kerr signal is contributed by electron and hole spins.

First part of this work devoted to the experimentally study of the spin dephasing times and spin relaxation mechanisms in (001) GaAs/(Al,Ga)As quantum well structures. The different experimental parameters, such as an applied external electric bias, magnetic-field, and temperature have been varied, in purpose to identify their effect on the spin dephasing rate. We demonstrate interesting result, the electron spin dephasing time T_2^* of 25 ns has been measured. This is currently the longest time reported in literature for semiconductor GaAs quantum wells. The long-lived spin memory is of great importance for possible practical applications. In order to measure the longest electron spin coherence time for the studied sample, the modified pump-probe Kerr rotation technique namely so called Resonant Spin Amplification method (RSA) was used.

Additionally, we measured time-resolved Kerr rotation signal for GaAs/(AlGa)As quantum well with different electron concentration. In n-doped GaAs/(Al,Ga)As quantum wells we don't observe the long spin dephasing times. We show for this structure, that there is no influence of the magnetic field on the spin dephasing time. The reason of such behaviour should be correspond to the Dyakonov-Perel mechanism. The most experimental results are focused on quantum wells grown on the substrate with

the standard crystallographic orientation (001). In this work were presented results of TRKR signal for quantum wells grown on the substrate with other orientation, namely (110). We demonstrate here the long spin dephasing time (1.28 ns) measured at high temperature $T = 100$ K for GaAs quantum well. We do not observe differences in the signals depending on orientation of the magnetic field applied in the plane of the sample. These features should be studied in the future more accurately.

The next part of this thesis corresponds to study of the carrier spin dynamics in a n-doped (In,Ga)As/GaAs quantum well by time-resolved Faraday rotation and ellipticity techniques in the temperature range down to 430 milliKelvin. We define here two contributions to the Faraday rotation and ellipticity signals due to interaction of the probe beam with the trion and exciton resonances. One interesting point concerning this structure is the observation of the long-lived spin dynamics of resident electrons measured in the regime of resonant spin amplification (RSA) at very low temperatures down to 430 mK. In order to achieve such low temperature we used ^{3}He system, which demands the efforts for performing the experiment. The characteristic bat-like shape is observed in the RSA signal, which contains information on the long-lived hole spin dynamics. The results of experiments for this structure, shows that carrier localization leads to a saturation of the spin relaxation times at 45 ns for electrons below 4.5 K and at 2 ns for holes below 2.3 K. At these temperatures the resident electrons are localized and their spin relaxation is provided by the hyperfine interaction with the nuclei spins, which is almost temperature independent. At the moment it is not clear to us what relaxation mechanism is controlling the hole spin dynamics in the range from 0.43-2.2 K. The hyperfine interaction with the nuclei is significantly weaker for the holes than for the electrons. Most probably it is due to the admixture of the light-hole to the heavy-hole states, enhancing strongly the possibility for spin-flip scattering.

The main idea of this thesis was to obtain valuable information about mechanisms which limit the spin memory and spin coherency lifetime in QWs. Depending on the structure properties and the experimental conditions, several mechanisms of spin relaxation may be important. We have already shown the results for GaAs/(Al,Ga)As quantum wells, where such effects like Dyakonov-Perel spin relaxation mechanism, electron-hole exchange interaction, and electron-electron scattering influence the spin relaxation times. Additionally to these effects, hyperfine interaction may also limit the longitudinal spin relaxation time. Otherwise the hyperfine interaction may result in stabilization of the electron spin and in a drastic prolongation of its lifetime if a dynamic nuclear polarization appears due to hyperfine interaction of the electron and nuclear spins. Such effect is already observed for QDs [94, 95]. So, hyperfine interaction in QWs may alter spin dynamics shortening or prolonging lifetime of the electron spin orientation.

We show the evidence of the nuclear polarization in the observation of the line splitting in RSA signals, corresponding to the nuclear magnetic resonances, under optical pumping with circularly polarized and alternatively modulated at frequency of 50 kHz pump pulse. The main result of these measurements is that we can identify peaks corresponding to nuclear isotopes by RSA. The next important point is that the alternatively modulation of the pump polarization also results in resonant cooling of

nuclei. This cooling is accompanied by the resonant change of nuclear polarization and can be also formally classified as the all-optical NMR. The electron-nuclear spin phenomena are still under study nowadays.

Last part of this thesis presents results of TRKR studied in a n-doped CdTe/(Cd,Mg)Te quantum well structure, using resonant excitation of the negatively charged exciton (trion) state. We demonstrate the possibility of the optical control of the spin coherence of quantum well electrons by short laser pulses with circular or linear polarization. Laser control pulses induce the amplitude and phase shifts of the electron spin beat signal in an external magnetic field. We show their dependence on the pump-control delay and polarization of the control relative to the pump pulse. Two types of the circularly polarized control pulse can be distinguished, additive and non-additive effects. The first one results in spin coherence generation by the control pulse, which may be added to or subtracted from the pump induced spin coherence. In case of non-additive effect, the measured signal is decreased by the control pulse and the suppression efficiency is determined by the control pulse power only. It is independent of the circular polarization of the control pulse and the amount of spin coherence induced by the pump. The same suppression is observed or linearly polarized control pulses, which do not generate any spin coherence in our geometry. At relatively small control powers, the suppression efficiency is the same for linearly and circularly polarized pulses.

Appendix A

Parameters

The Chapter 2 gives an overview of all samples that are investigated in this thesis. Here are displayed the growth parameters of the samples #p340, #p343, 32A21M7A, #11708, #11309 and #11320.

Layer	***Function***	***Thickness [nm]***
GaAs(001) substrate		
GaAs		1116.1
$Al_{0.21}Ga_{0.66}As$		4.5
GaAs		3.6
$Al_{0.29}Ga_{0.66}As$		5
GaAs		3.6
$Al_{0.31}Ga_{0.66}As$		5.7
11SL 2.8($Al_{0.31}$)x2		54.8
$Al_{0.31}Ga_{0.66}As$		314
11SL 2.5($Al_{0.31}$)x2.5		55
GaAs		282.7
$Al_{0.34}Ga_{0.66}As$		49.5
GaAs	Quantum well	19.8
$Al_{0.34}Ga_{0.66}As$		49.5
GaAs	Quantum well	14
$Al_{0.34}Ga_{0.66}As$		49.5
GaAs	Quantum well	9.3
$Al_{0.34}Ga_{0.66}As$		49.5
GaAs	Quantum well	5.6
$Al_{0.34}Ga_{0.66}As$		198.1
GaAs		9.3

Table A.1: The growth table of the structure #p340

Sample	***QW width (nm)***	***Transition E (eV)***	$\|g_{e,xy}\|$
p340	17.2	e1-hh1 1.527	0.40 ± 0.001
	13	e1-hh1 1.535	0.33 ± 0.001
	13	e1-lh1 1.542	0.33 ± 0.001
	13	e1-hh2 1.597	0.32 ± 0.001
	8.8	e1-hh1 1.555	0.20 ± 0.001
	5.1	e1-hh1 1.600	0.00 ± 0.001

Table A.2: Parameters of GaAs/(Al,Ga)As QW structure p340

Layer	***Function***	***Thickness [nm]***
Si:GaAs(001) substrate		
GaAs		805.4
14SL 2.6($Al_{0.28}$)x1.9		63
$Al_{0.28}Ga_{0.66}As$		383.9
11SL 2.6($Al_{0.28}$)x1.9		49.5
GaAs		236.7
3SLii 2($Al_{0.28}$)x2.2		12.6
$Al_{0.33}Ga_{0.66}As$		35.6
2SLii 2($Al_{0.28}$)x2		8
$Al_{0.33}Ga_{0.66}As^{0.44}$		55.6
GaAs	Quantum well	20
$Al_{0.33}Ga_{0.66}As$		55.5
GaAs	Quantum well	14.1
$Al_{0.33}Ga_{0.66}As$		55.5
GaAs	Quantum well	9.3
$Al_{0.33}Ga_{0.66}As$		55.5
GaAs	Quantum well	5.7
$Al_{0.33}Ga_{0.66}As^{0.44}$		138.7
$GaAs^{0.44}$		10

Table A.3: The growth table of the structure #p343

Sample	***QW width (nm)***	***Transition E (eV)***	$\|g_{e,xy}\|$
p343	14.3	e1-hh1 1.530	0.34 ± 0.01
	10.2	e1-hh1 1.543	0.27 ± 0.01
	7.3	e1-lh1 1.542	0.13 ± 0.01
	4.2	e1-hh1 1.597	0.06 ± 0.001

Table A.4: Parameters of GaAs/(Al,Ga)As QW structure #p343

Layer	***Function***	***Thickness [Å]***
GaAs substrate		
AlGaAs/AlAs	Bragg mirror	
AlAs		400
GaAs		25
AlAs		100
GaAs	Quantum well	200
AlAs		100
GaAs		25
AlAs		400
AlGaAs/AlAs	Bragg mirror	

Table A.5: The growth table of the structure 32A21M7

Layer	***Loop***	***T [°C]***	***Dur. [s]***	***Thickness [nm]***
GaAs substrate				
GaAs		700.0	261.8	50
AlAs	start: 15x	700.0	20.0	2
GaAs	end	700.0	10.5	2
GaAs		700.0	523.6	100
GaAs:Si		700.0	523.6	100
GaAs		700.0	471.2	90
GaAs		600.0	52.4	10
$In_{0.09}Ga_{0.91}As$		600.0	37.9	8
GaAs		600.0	8.9	1.7
$In_{0.09}Ga_{0.91}As$		600.0	37.9	8
GaAs		600.0	52.4	10
GaAs		700.0	471.2	90

Table A.6: The growth table of the structure #11708

Layer	***T [°C]***	***Thickness [nm]***
$Al_{0.15}Ga_{0.85}As$	490	400
GaAs	440	20
$Al_{0.15}Ga_{0.85}As$	490	120
GaAs	440	5
$In_{0.03}Ga_{0.97}As$	440	20
GaAs	490	5
$Al_{0.15}Ga_{0.85}As$	490	120
GaAs	440	5
$In_{0.04}Ga_{0.96}As$	440	20
GaAs	490	5
$Al_{0.15}Ga_{0.85}As$	490	120
GaAs	440	5
$In_{0.06}Ga_{0.94}As$	440	20
GaAs	490	5
$Al_{0.15}Ga_{0.85}As$	490	700
GaAs	490	200
Substrate: Si-GaAs (110)		

Table A.7: Parameters of structure PDI-M4-2264

Layer	***Loop***	***T [°C]***	***Dur. [s]***	***Thickness [nm]***
GaAs		650.0	273.0	50.0
AlAs	start: 20x	650.0	30.9	3.0
GaAs	end	650.0	16.4	3.0
GaAs		650.0	546.0	99.9
AlAs	start: 15x	650.0	10.3	1.0
GaAs	end	650.0	10.9	2.0
AlAs	start: 7x	650.0	8.2	0.8
GaAs	end	650.0	13.1	2.4
AlAs		650.0	8.2	0.8
GaAs		650.0	6.5	1.2
Si-Delta		550.0	30.0	0.0ML
GaAs		550.0	6.6	1.2
AlAs	start: 6x	650.0	8.2	0.8
GaAs	end	650.0	13.1	2.4
AlAs		650.0	8.2	0.8
GaAs		650.0	55.5	10.2
AlAs	start: 6x	650.0	8.2	0.8
GaAs	end	650.0	13.1	2.4
AlAs		650.0	8.2	0.8
GaAs		650.0	6.5	1.2
Si-Delta		550.0	30.0	0.0ML
GaAs		550.0	6.6	1.2

Table A.8: The growth table of the structure #11309

Layer	***Loop***	***T [°C]***	***Dur. [s]***	***Thickness [nm]***
GaAs		650.0	274.7	50.0
AlAs	start: 20x	650.0	31.9	3.0
GaAs	end	650.0	16.5	3.0
GaAs		650.0	549.5	100
AlAs	start: 15x	650.0	10.6	1.0
GaAs	end	650.0	11.0	2.0
AlAs	start: 7x	650.0	8.5	0.8
GaAs	end	650.0	13.2	2.4
AlAs		650.0	8.5	0.8
GaAs		650.0	6.6	1.2
Si-Delta		550.0	4.0	
GaAs		550.0	6.6	1.2
AlAs	start: 6x	650.0	8.5	0.8
GaAs	end	650.0	13.2	2.4
AlAs		650.0	8.5	0.8
GaAs		650.0	55.9	10.2
AlAs	start: 6x	650.0	8.5	0.8
GaAs	end	650.0	13.2	2.4
AlAs		650.0	8.5	0.8
GaAs		650.0	6.6	1.2
Si-Delta		550.0	4.0	
GaAs		550.0	6.6	1.2
AlAs	start: 7x	650.0	8.5	0.8
GaAs	end	650.0	13.2	2.4
AlAs	start 15x	650.0	10.6	1.0
GaAs	end	650.0	11.0	2.0
GaAs		650.0	22.0	4.0

Table A.9: The growth table of the structure #11320

Bibliography

[1] Sankar Das Sarma, Spintronics, http://www.americanscientist.org/articles/01articles/dassarma.html.

[2] S. Luescher, T. Heinzel, K. Ensslin, W. Wegscheider, M. Bichler, Phys. Rev. Lett. **86**, 2114 (2001).

[3] D. Loss, D. P. DiVincenzo, Phys. Rev. A **57**, 120 (1998), cond-mat=9701055.

[4] D. P. DiVincenzo, D. Loss, J. Magn. Mater. **200**, 202 (1999).

[5] M. N. Leuenberger, D. Loss, Physica E 10, 452 457 (2001).

[6] S. ONeil, *Coherent Optical Manipulation of Electron Spins in Semiconductor Nanostructures*, PhD thesis, the Department of Physics and the Graduate School of the University of Oregon (2008).

[7] M. Heidkamp, *Spin-Coherence and Dephasing of Donor and Free Conduction Band Electrons across the Metal-Insulator Transition in Si:GaAs*, PhD thesis, RWTH Aachen (2004).

[8] M. Fox, *Optical properties of solids*, (Oxvord University Press, New York, 2001).

[9] J. J. Sakurai, *Modern Quantum Mechanics*, (Addison-Wesley, Reading, 1994).

[10] B. Beschoten, *Spin coherence in semiconductors*, 2. Physikalisches Institut, RWTH Aachen, Germany.

[11] J. M. Kikkawa, D. D. Awschalom, Phys. Rev. Lett. **80**, 4313 (1998).

[12] D. R. Yakovlev, E. A. Zhukov, M. Bayer, G. Karczewski, T. Wojtowicz, and J. Kossut, Int. J. Modern Physics B **21**, 1336 (2007).

[13] X. Marie, T. Amand, P. Le Jeune, M. Paillard, P. Renucci, L. E. Golub, V. D. Dymnikov, and E. L. Ivchenko, Phys. Rev. B **60**, 5811 (1999).

[14] M. Syperek, D. R. Yakovlev, A. Greilich, J. Misiewicz, M. Bayer, D. Reuter, and A. D. Wieck, Phys. Rev. Lett. **99**, 187401 (2007).

[15] I. A. Merkulov, Al. L. Efros, and M. Rosen, Phys. Rev. B **65**, 205309 (2002).

[16] *Spin Physics in Semiconductors*, Ed. M. I. Dyakonov, (Springer-Verlag, Berlin, 2008), Ch.6, p.135.

[17] Glazov M. and Ivchenko E., JETP , **99** (2004) 1279.

[18] Glazov M. and Ivchenko E., JETP Letters , **75**, 403 (2002).

[19] M. I. Dyakonov, Kachorovskii, Fiz. Tekh. Poluprovodn. **20**, 178 (1986). [Sov. Phys. Semicond. **20**, 110 (1986)].

[20] M. W. Wu, M. Kuwata-Gonokami, Solid State Communications **121**, 509 (2002).

[21] S. Dhrmann, D. Hgele, J. Rudolph, M. Bichler, D. Schuh, and M. Oestreich, Phys. Rev. Lett. 93, 147405 (2004).

[22] L.Schreiber, D. Duda, B. Beschoten, and G. Gntherodt, Phys. Rev. B **75**, 193304 (2007).

[23] N. S. Averkiev, L. E. Golub, A. S. Gurevich, V. P. Evtikhiev, V. P. Kochereshko, A. V. Platonov, A. S. Shkolnik, and Yu. P. Efimov, Phys. Rev. B **74**, 033305 (2006).

[24] N. S. Averkiev and L. E. Golub, Phys. Rev. B **60**, 1558215584 (1999).

[25] J. Strand, X. Lou, C. Adelmann, B.D. Schultz, Phys. Rev. B **72**, 155308 (2005).

[26] G. L.Bir, A. G. Aronov, G. E. Pikus, , Zh. Eksp. Teor. Fiz. 69, 13821397 [Sov. Phys. JETP 42, 705712 (1976)].

[27] J. M. Kikkawa, D. D. Awschalom, Science **287**, 473 (2000).

[28] E. A. Zhukov, D. R. Yakovlev, M. Bayer, G. Karczewski, T. Wojtowicz, and J. Kossut, Phys. Stat. Sol. (b) **243**, 878 (2006).

[29] G. V. Astakhov, V. P. Kochereshko, D. R. Yakovlev, W. Ossau, J. Nürnberger, W. Faschinger, G. Landwehr, T. Wojtowicz, G. Karczewski, and J. Kossut, Phys. Rev. B **65**, 115310 (2002).

[30] T. A. Kennedy, A. Shabaev, M. Scheibner, Al. L. Efros, A. S. Bracker, and D. Gammon, Phys. Rev. B **73**, 045307 (2006).

[31] A. Greilich, R. Oulton, E. A. Zhukov, I. A. Yugova, D. R. Yakovlev, M. Bayer, A. Shabaev, Al. L. Efros, I. A. Merkulov, V. Stavarache, D. Reuter, and A. Wieck, Phys. Rev. Lett. **96**, 227401 (2006).

[32] A. Shabaev, Al. L. Efros, D. Gammon, and I. A. Merkulov, Phys. Rev. B **68**, 201305(R) (2003).

[33] E. L. Ivchenko, *Optical spectroscopy of semiconductor nanostructures*, (Alpha Science, Harrow UK, 2005).

[34] E. A. Zhukov, D. R. Yakovlev, M. Bayer, M. M. Glazov, E. L. Ivchenko, G. Karczewski, T. Wojtowicz, and J. Kossut, Phys. Rev. B **76**, 205310 (2007).

[35] J. M. Kikkawa, D. D. Awschalom, Phys. Rev. Lett. **80**, 4313 (1998).

[36] I. A. Yugova, A. A. Sokolova, D. R. Yakovlev, A. Greilich, D. Reuter, A. D. Wieck, M. Bayer, Phys. Rev. Lett. **102**, 167402 (2009).

[37] *Semiconductor Spintronics and Quantum Computation*, Eds. D. D. Awschalom, D. Loss, and N. Samarth (Springer-Verlag, Berlin, 2002).

[38] A. Malinowski, D. J. Guerrier, N. J. Traynor, and R. T. Harley, Phys. Rev. B **60**, 77287731 (1999).

[39] A. Malinowski, M.A. Brand, R. T. Harley, Solid State Commun. **116**, 333 (2000).

[40] A. V. Kimel, F. Bentivegna, V. N. Gridnev, V. V. Pavlov, R. V. Pisarev, Th.Rasing, Phys. Rev. B. **63**, 235201 (2001).

[41] T. A. Kennedy, A. Shabaev, M. Scheibner, Al. L. Efros, A. S. Bracker, and D.Gammon, Phys. Rev. B **73**, 045307 (2006).

[42] A. Shabaev, Al. L. Efros, D. Gammon, and I. A. Merkulov, Phys. Rev. B **68**, 201305R (2003).

[43] A. Greilich, R. Oulton, E. A. Zhukov, I. A. Yugova, D. R. Yakovlev, M. Bayer, A. Shabaev, Al. L. Efros, I. A. Merkulov, V. Stavarache, D. Reuter, and A. Wieck, Phys. Rev. Lett. **96**, 227401 (2006).

[44] X. Marie, T. Amand, P. Le Jeune, M. Paillard, P. Renucci, L. E. Golub, V. D. Dymnikov, E. L. Ivchenko, Phys. Rev. B. **60**, 5811 (1999).

[45] M. Syperek, D. R. Yakovlev, A. Greilich, J. Misiewicz, M. Bayer, D. Reuter, A.D. Wieck, Phys. Rev. Lett. **99**, 187401 (2007).

[46] A. Greilich, D. R. Yakovlev, A. Shabaev, Al. L. Efros, I. A. Yugova, R. Oulton, V. Stavarache, D. Reuter, A. Wieck, and M. Bayer, Science **313**, 341 (2006).

[47] P. Felbier, *Oxford 7 tesla cryostat with ^{3}He inset*, User's Guide V 1.0 (2009).

[48] M. Perrin, J. Bloch, A. Lemaitre, and P. Senellart Phys. Stat. Sol. (c) 2, 759762 (2005).

[49] H. W. van Kesteren, E. C. Cosman, W. A. J. A. van der Poel, and C. T. Foxon, Phys. Rev. B **41**, 5283 (1990).

[50] F. Meier, B. P. Zakharchenya, em Optical Orientation, North-Holland, New York (1984).

[51] X. Marie, T. Amand, P. Le Jeune, M. Paillard, P. Renucci, L. E. Golub, V. D. Dymnikov, and E. L. Ivchenko, Phys. Rev. B **60**, 5811 (1999).

[52] K. Kheng, R. T. Cox, Y. Merle dAubigne, F. Bassani, K. Saminadayar, and S. Tatarenko, Phys. Rev. Lett. **71**, 1752, (1993).

[53] T. A.Kennedy, A. Shabaev, M. Scheibner, Al. L. Efros, A. S. Bracker, D. Gammon, Phys. Rev. B **73**, 045307 (2006).

[54] I. Ya. Gerlovin, Yu. P. Efimov, Yu. K. Dolgikh, S. A. Eliseev, V. V. Ovsyankin, V. V. Petrov, R. V. Cherbunin, I. V. Ignatiev, I. A. Yugova, L. V. Fokina, A. Greilich, D. R. Yakovlev, and M. Bayer, Phys. Rev. B **75**, 115330 (2007).

[55] T. Amand, X. Marie, P. Le Jeune, M. Brousseau, D. Robart, J. Barrau, R. Planel, Phys. Rev. Lett. **78**, 1355 (1997).

[56] T. C. Damen, L. Vina, J. E. Cunningham, J. Shah, and L. J. Sham, Phys. Rev. Lett. **67**, 3432 (1991).

[57] E. L. Ivchenko, A. A. Kiselev, and M. Willander, Solid State Commun. **102**, 375 (1997).

[58] R. I. Dzhioev, V. L. Korenev, B. P. Zakharchenya, D. Gammon, A. S. Bracker, J. G. Tischler, Phys. Rev. B **66**, 153409 (2002).

[59] A. J. Shields, M. Pepper, D. A. Ritchie, M. Y. Simmons, and G. A. C. Jones, Phys. Rev. B **51**, 18049 (1995).

[60] J. Tribollet, F. Bernardot, M. Menant, G. Karczewski, C. Testelin, and M. Chamarro, Phys. Rev. B **68**, 235316 (2003).

[61] R. I. Dzhioev, K. V. Kavokin, V. L Korenev, M. V. Lazarev, B. Ya. Meltser, M. N. Stepanova, B. P. Zakharchenya, D. Gammon, D. S. Katzer, Phys. Rev. B. **66**, 245204, (2002).

[62] G. V. Astakhov, M. M. Glazov, D. R. Yakovlev, E. A. Zhukov, W. Ossau, L. W. Molenkamp, and M. Bayer, Semicond. Sci. Technol. 23, 114001 (2008).

[63] H. J.Zhu, M. Ramsteiner, H. Kostial, M. Wassermeier, H.-P. Schönherr, K. H.Ploog, Phys. Rev. Lett. **87**, 016601 (2001).

[64] A. T. Hanbicki, B. T.Jonker, et all, Appl. Phys. Lett **80**, 1240 (2002). Ed. M. I. Dyakonov, (Springer-Verlag, Berlin, 2008).

[65] C. F. Klingshirn, em Semiconductor Optics, (Springer-Verlag, Berlin 1995).

[66] M. A. Lampert, Phys. Rev. Lett. **1**, 450 (1958).

[67] Israel Bar-Joseph, Semicond. Sci. Technol. **20**, R29 R39 (2005).

[68] M. Fox, *Quantum Optics: an Introduction*, Band 15, Oxford master series in atomic, optical and laser physics, (Oxford University Press, 2006).

[69] S. Das Sharma, Jaroslav Fabian, I. Zutic, *Spintronics: Fundamental and Applications*, Rev of modern Physic Vol. **76**, (2004).

[70] M. I. Dyakonov, V. I. Perel, Fiz. Tverd. Tela **13**, 3581 (1971). [Sov. Phys. Solid State **13**, 3023 (1972)].

[71] M. Gerbracht *Optically detected resonances induced by fair ifrared radiation in quantum wells and quantum dots*, PhD thesis, TU Dortmund (2008).

[72] B. Baylac, T. Amand, X. Marie, B. Dareys, M. Brousseau, G. Bacquet, and V. Thierry-Mieg, Solid State Commun. **93**, 57 (1995).

[73] M. Kugler, T. Andlauer, T. Korn, A. Wagner, S. Fehringer, R. Schulz, M. Kubova, C. Gerl, D. Schuh, W. Wegscheider, P. Vogl, and C. Schüller, Phys. Rev. B **80**, 035325 (2009).

[74] I. A. Yugova, M. M. Glazov, E. L. Ivchenko, and Al. L. Efros, Phys. Rev. B **80**, 104436 (2009).

[75] G. V. Astakhov, V. P. Kochereshko, D. R. Yakovlev, W. Ossau, J. Nürnberger, W. Faschinger, and G. Landwehr, Phys. Rev. B **62**, 10345 (2000). The values introduced in this paper: A is the area of QW layer and A_{T} is the trion area are in the following relation with the α_{T} value from the present work: $\alpha_{\mathrm{T}} = A_{\mathrm{T}}/A$.

[76] I. A. Yugova, A. Greilich, D. R. Yakovlev, A. A. Kiselev, M. Bayer, V. V. Dolgikh,D. Reuter, and A. D. Wieck, Phys. Rev. B **75**, 245302 (2007).

[77] T. Korn, M. Kugler, M. Griesbeck, R. Schulz, A. Wagner, M. Kubova, C. Gerl, D. Schuh, W. Wegscheider, and C. Schüller, arXiv:0909.3711v [cond-mat.mes-hall] 21 September 2009.

[78] M. I. Dyakonov, V. I. Perel, *Optical Orientation, Modern Problems in Condensed Matter Science*, Vol. 8, edited by F. Meier and B. P. Zakharchenya (North-Holland, Amsterdam, 1984), pp. 1171.

[79] A. Abragam, *The Principles of Nuclear Magnetism*, (Clarendon Press, Oxford, 1961).

[80] V.K. Kalevich, B.P. Zakharchenya, Physics of the Solid State, Volume **37**, Issue 11, November 1995, pp.1938-1940.

[81] V. K. Kalevich, V. D. Kul'kov, and V. G. Fleisher, Sov. Phys. Solid State **22**, 703 (1980).

[82] V. K. Kalevich, B. P. Zakharchenya, and O. M. Fedorova, Fiz. Tverd. Tela **37**, 287 (1995) [Phys. Solid State **37**, 154 (1995)].

[83] O. D. D. Couto, Jr., *Acoustically induced spin transport in (110) GaAs quantum wells*, PhD Thesis, Berlin (2008).

[84] K. C. Ku, S. H. Chun, W. H. Wang, W. Fadgen, D. A. Issadore, N. Samarth, R. J. Epstein, and D. D. Awschalom, Journal of Superconductivity, **18**, 185-188 (2005).

[85] E. A. Zhukov, D. R. Yakovlev, M. M. Glazov, L. Fokina, G. Karczewski, T. Wojtowicz, J. Kossut and M. Bayer, *Optical control of electron spin coherence in CdTe/(Cd,Mg)Te quantum wells*, submitted to PRB on 14 Dec 2009, arXiv: cond-mat, 0912.2589v1.

[86] X. Z. Ruan, H. H. Luo, Yang Ji, and Z. Y. Xu,V. Umansky, Phys. Rev. B **77**, 193307 (2008).

[87] *Semiconductor Quantum Bits*, Eds. F. Henneberger and O. Benson (World Scientific, Singapore, 2008).

[88] A. A. Sirenko, T. Ruf, M. Cardona, D. R. Yakovlev, W. Ossau, A. Waag, and G. Landwehr, Phys. Rev. B **56**, 2114 (1997).

[89] R. Akimoto, K. Ando, F. Sasaki, S. Kobayashi, and T. Tani, J. Appl. Phys. **84**, 6318 (1998).

[90] I. A. Yugova, M. M. Glazov, E. L. Ivchenko, and Al. L. Efros, Phys. Rev. B **80**, 104436 (2009).

[91] G. V. Astakhov, D. R. Yakovlev, V. V. Rudenkov, P. C. M. Christianen, T. Barrick, S. A. Crooker, A. B. Dzyubenko, W. Ossau, J. C. Maan, G. Karczewski, and T. Wojtowicz, Phys. Rev. B **71**, 201312(R) (2005).

[92] G. V. Astakhov, V. P. Kochereshko, D. R. Yakovlev, W. Ossau, J. Nürnberger, W. Faschinger, G. Landwehr, T. Wojtowicz, G. Karczewski, and J. Kossut, Phys. Rev. B **65**, 115310 (2002).

[93] L. V. Fokina, I. A. Yugova, D. R. Yakovlev, M. M. Glazov, I. A. Akimov, A. Greilich, D. Reuter, A. D. Wieck, M. Bayer, submitted to PRB on 19 Jan 2010, arXiv: cond-mat, 1001.3228v1.

[94] S. Yu. Verbin,B. Pal, M. Ikezawa, I. V. Ignatiev, Y. Masumoto, Physics of Semiconductors **893**, 1325-1326 (2007).

[95] R. Oulton, A. Greilich, S. Yu. Verbin, R. V. Cherbunin, T. Auer, D. R. Yakovlev, M. Bayer, I. A. Merkulov, V. Stavarache, D. Reuter, and A. D. Wieck, Phys. Rev. Lett. **98**, 107401 (2007).

List of Figures

Index

Symbols and abbreviations

symbol	**meaning**
$\|\uparrow\rangle$, $\|\downarrow\rangle$	spin up state, spin down state
$\|0\rangle$, $\|1\rangle$	general basis states
a	lattice constant
$a_B^{ex,h}$	exciton, hydrogen Bohr radius
B	magnetic field
$\mathbf{B}$	magnetic field vector
CB	conduction band
c_0	speed of light in vacuum (299 792 458 m s^{-1})
CCD	charge coupled device camera
c	coefficient
cw	continuous wave
CdTe	Cadmium Telluride
2DEG	two-dimensional electron gas
ΔE	energy difference
Δ	detuning
DNP	dynamic nuclear polarization
DP	Dyakonov-Perel mechanism
EY	Elliot-Yafet mechanism
E	energy
E_{conf}	confinement energy
E_{gap}	band gap energy
$E^{C,V}(\mathbf{k})$	dispersion of the conduction/valence band
E_B^{ex}	exciton binding energy
E_{Ry}^h	Rydberg energy
e	unit charge ($1.602176 \cdot 10^{-19}$ C)
eV	electron volt ($1.602176 \cdot 10^{-19}$ J)
ε, ε_0	dielectric constant, in vacuum

fcc	face-centered cubic
fs	femtosecond
g_e	effective electron g-factor
g_h	effective hole g-factor
g_0	free electron g-factor
GaAs	Gallium Arsenide
Γ_i	conduction band ($i = 6$) or valence band ($i = 7, 8$) symmetry
Γ-point	point of high symmetry,for GaAs in the center of the first Brillouin zone
HeNe	helium-neon
$\hbar$	$h/2\pi$= 1.054571$\cdot$ 10^{-34} J s= 6.582118$\cdot$ 10^{-16} eV s
H,H'	Hamiltonian, interaction Hamiltonian
H	magnetic field strength
$\hbar$	$h/2\pi$= 1.054571$\cdot$ 10^{-34} J s= 6.582118$\cdot$ 10^{-16} eV s
i	integer index $i = 0, 1, 2..$
I	current
InAs	Indium Arsenide
I	nuclear spin
J	total angular momentum and electric current density
J_z	z-component of the angular momentum
K	Kelvin
k_B	Boltzmann constant $1.38062 \cdot 10^{-23} JK^{-1}$
k	wave vector
L	orbital angular momentum
L_z	z-component of the orbital momentum
λ	wavelength
M	magnetization
m_0	electron mass ($9.109381 \cdot 10^{-31}$ kg)
m_e	effective electron mass
m_h	effective hole mass
m_X	effective exciton mass
meV	milli electron volt
ms	millisecond
μ	effective mass
μ_0	permeability in vacuum
μ_B	Bohr magneton
μm	micrometer
μs	microsecond

n	refractive index
Nd:YAG	yttrium aluminium garnet doped with neodymium
NMR	nuclear magnetic resonance
nm	nanometer
ns	nanosecond
$N(t)$ number of spins	
NHC	nuclear hyperfine coupling
$\Omega_{e,h}$	momentum dependent spin field for electron and hole
Ω	damping constant
p	label for p (band) electrons
$\mathbf{P}$	polarization
$\mathbf{p}$	dipole moment
P_{exc}	excitation power
PC	photonic crystal
PL	photoluminescence
ps	picosecond
φ_a, b	orthogonal functions
QB	quantum beat
QW	quantum well
ρ	charge density and density matrix
R	photodiode responsivity
RSA	resonant spin amplification
$\mathbf{S}$	Spin
S_z	z-component of the spin
s	label for s (band) electrons
SO	split-off band
σ_C	circular polarization degree
$\sigma_{x,y,z}$	Pauli-matrices
t	time
T	temperature, Tesla
T	Tesla
T^-, T^+	the negatively- and positively-charged trion respectively
T_R	laser repetition period
T_D	delay time
T_1	longitudinal spin relaxation time
T_2	transverse spin relaxation time, decoherence time
T_2^*	transverse spin dephasing time
Θ	pulse area of excitation

θ_F (θ_K)	Faraday (Kerr) rotation angles
U	voltage
U_{eff}	effective voltage
V	Volt
VB	valence band
ω_L	Larmor frequency
$\omega_{e,h,exc}$	electron, hole, exciton frequency
W	Watt
$\|X\rangle$	exciton state
Ψ	wavefunction
Ψ_k	state k in density matrix formalism

Publications

Parts of this work are or will be published as follows:

1. "*Electron-spin dephasing in $GaAs/Al_{0.34}Ga_{0.66}As$ quantum wells with a gate-controlled electron density*"
   I. Ya. Gerlovin, Yu. P. Efimov, Yu. K. Dolgikh, S. A. Eliseev, V. V. Ovsyankin, and V. V. Petrov, R. V. Cherbunin, I. V. Ignatiev, and I. A. Yugova
   L. V. Fokina, A. Greilich, D. R. Yakovlev, and M. Bayer
   Phys. Rev. B ***75****, 115330 (2007)*

2. "*Optical control of electron spin coherence in CdTe/(Cd,Mg)Te quantum wells*"
   E. A. Zhukov, D. R. Yakovlev, M. M. Glazov,
   L.V. Fokina, G. Karczewski, T. Wojtowicz, J. Kossut, M. Bayer
   Submitted to PRB on 14 Dec 2009, arXiv: cond-mat, 0912.2589v1

3. "*Spin dynamics of electrons and holes in InGaAs/GaAs quantum wells at milliKelvin temperatures*"
   L. V. Fokina, I. A. Yugova, D. R. Yakovlev, M. M. Glazov, I. A. Akimov, A. Greilich, D. Reuter, A. D. Wieck, M. Bayer
   Submitted to PRB on 19 Jan 2010, arXiv: cond-mat, 1001.3228v1

Acknowledgements

This work would not have been possible without the help of many people, whom I want to thank here for their mental, scientific, and financial support, for valuable discussions and technical assistance.

I would like to express my deep and sincere gratitude to Prof. Dr. Dmitri R. Yakovlev and Prof. Dr. Manfred Bayer, who gave me the opportunity to perform these studies, for their constant intellectual, emotional, and material support. Their excellent scientific expertise, in combination with their friendly, helpful and tolerant character make them an outstanding academic team.

A special thanks goes to Prof. Dr. Dietmar Fröhlich who helped me during the measurements with ^{3}He Setup and greatly enriched my knowledge.

I wish to express my warm and sincere thanks to Evgeny Zhukov, Ivan Ignatiev and Vladimir Lukoshkin for their kind support, help and guidance.

Additional thanks to Alex Greilich for the good collaboration, friendly and continuous help and of course for his always good mood, that created a great atmosphere in the office.

My sincere thanks to Misha Glazov, for proof reading of the thesis, his excellent advices and incredible ability to explain things.

I want to thank Irina Yugova for her continuous help and support during our measurements time in the dark pico-lab. I also thank Ilya Akimov. I wish to thank Klaus Wiegers for his creative ideas and technical support. I am grateful to Michaela Wäscher for providing permanent administrative support.

Thanks to all colleagues, present and past, of the Experimental Physik II group for the good working atmosphere and a great time. I apologize for not addressing everyone in person.

I also wish to thank Oleh Fedorych for his support and solving my computer problems.

I want to thank Anna and Yury Braun for being my best friends. "Capchiki" are the best!

Finally, I would like to thank my loving parents Elena and Vladimir for their care, protection, and for their amazing love and endless support. Their love gave me the strength to make this work possible. I dedicate this thesis to my mom and dad.